CALT 68-2001
DOE Research and
Development Report

Search for GUT Magnetic Monopoles with the MACRO Detector

Thesis by

Erotokritos C. Katsavounidis

In Partial Fulfillment of the Requirements
for the Degree of
Doctor of Philosophy

California Institute of Technology
Pasadena, California

1996

(Submitted June 12, 1995)

Acknowledgements

I am deeply grateful to my thesis advisor Professor Barry Barish for his continuous guidance and support throughout my graduate studies. I also owe my sincere appreciation to Professor Charles Peck for the guidance and encouragement that I received from him. Professors B. Barish and C. Peck have been for me an unlimited source of knowledge and experience.

I would also like to thank all my fellow graduate students (past and present) and the postdoctoral fellow members of the Caltech MACRO group. I feel part of this work belongs to them not only because of their major contribution in the construction of the MACRO detector in Italy, but also because of their critical comments, suggestions and generous help that they provided me with throughout the whole course of my graduate research work. My thanks especially go to Bob Nolty and Kate Scholberg who went through the early drafts of this thesis and provided me with valuable remarks and corrections.

From the other side of the Atlantic, I would like to thank the Laboratori Nazionali del Gran Sasso and the Istituto Nazionale di Fisica Nucleare (INFN-sessione di Bologna) for their warm hospitality and financial support during my extended stay in Gran Sasso and in Bologna, Italy.

Finally, I would like to express my special thanks to my brother Yiannis Katsavounidis who first brought to my attention the wavelet transform.

Abstract

Grand Unified Theories (GUT) predict the existence of superheavy magnetic monopoles ($\sim 10^{16} GeV$) as stable particle carrying magnetic charge. The extremely large mass of the GUT monopoles requires that they would have been produced during the early formation of the Universe and would probably have survived until today traveling through the Universe at nonrelativistic velocities. Cosmological arguments regarding the abundance of the magnetic monopoles today yield either too many or too few of them. However, simple arguments regarding the survival of the galactic field may set a reliable upper bound on the monopole flux. This is the so-called Parker bound and places an upper limit on the monopole flux of the order of $10^{-15} cm^{-2} sr^{-1} sec^{-1}$ for monopoles with mass $\sim 10^{16} GeV$ and typical galactic velocities $10^{-3} c$.

The MACRO detector at Gran Sasso (Italy) is a large underground detector offering large acceptance ($\sim 10,000 m^2 sr$) and high redundancy for a search for magnetic monopoles. The detector's large acceptance and different detection techniques will allow monopole searches ultimately beyond the astrophysical bound with high sensitivity over all the possible β-range of a monopole. The scintillator system of the full lower MACRO detector has been operational from December 1992 to June 1993 (total live time 160.7 days) and collected data with a trigger specialized to select slow ($10^{-4} c - 10^{-3} c$) moving particles. The waveforms of the candidate events have been recorded with commercially available waveform digitizers. More than 8,000 events that involved slow particle triggers from at least two different detector faces were found in this data set.

In analyzing this data set we have adapted the Haar decomposition (one of the simplest examples of the Wavelet Transform) of the candidate events. Our purpose was to build an algorithm that will effectively discriminate background (i.e., muon, radioactivity and noise) from monopole waveforms. Using various features of the Haar decomposition of the waveforms (like the propagation of the wavelet maxima

among scales and the energy content of each scale), we derived simple conditions by means of which we can efficiently select candidate waveforms. More than 80% of the initial dataset was thus rejected and the remaining events were visually scanned and classified. No signal was consistent with a slow magnetic monopole signature, and based on that we have established an upper flux limit on the monopole flux.

The detector's acceptance was obtained via a Monte Carlo simulation on a *run-by-run* basis, and for the majority of the runs it had an average value of $5200 m^2 sr$. The total effective exposure has been $5.6 \times 10^{14} cm^2 sr^1 sec^1$, corresponding to an isotropic upper monopole flux limit of $4.1 \times 10^{-15} cm^{-2} sr^{-1} sec^{-1}$ at the 90% confidence level. This limit is valid for monopoles in the velocity regime $1.5 \times 10^{-4} c \lesssim v \lesssim 4 \times 10^{-3} c$.

Contents

List of Figures

List of Tables

Chapter 1

Magnetic Monopoles: Theory and Experiment

It has been more than sixty years since P. A. M. Dirac [38] put forward the idea that magnetic monopoles, stable particles carrying magnetic charge, might exist. Since then, magnetic monopoles have been a subject of extensive theoretical and experimental work. Theoretical work has led to connections of the existence of magnetic monopoles to Grand Unified Theories (GUTs), Cosmology and Astrophysics; however it has offered rather little guidance as to their expected flux. On the other hand, experimental searches, besides only a few exciting moments when the long sought particle seemed to have given itself away [26] [30], have offered so far not a single shred of evidence for its existence. In this chapter we review the theory of the magnetic monopoles and the major experimental work that has been done in this field so far[1]. We start with a presentation of the monopole idea in the context of classical and quantum electrodymanics and continue with how monopoles arise in GUTs. We then move on to the cosmological and astrophysical implications of the existence of magnetic monopoles and describe how monopoles are expected to interact with matter. The limits on the magnetic monopole flux as obtained from various experiments so far are finally presented.

1.1 Monopoles in Abelian Theories

Within the context of classical electrodynamics, one may ask himself if Maxwell equations formally allow the existence of magnetic monopoles. The way classical electrodymanics is formulated assumes that all electric and magnetic fields are due to elementary electric charges. As a result of that, no matter if you start with Coulomb's

[1] A thorough review of the theory and detection of the magnetic monopoles may be found in the review articles of J. Preskill [94], D. E. Groom [49] and G. Giacomelli [48].

law and you invoke relativity or you start with Biot-Savart law, you always end up with a divergenceless magnetic induction $\mathbf{B}$. The fact that $\nabla \cdot \mathbf{B}$ is zero means that there can not be found sources of $\mathbf{B}$ while through Green's theorem, it implies that the net flux of magnetic induction through any closed surface is equal to zero. This *a priori* exclusion of magnetic sources from Maxwell's equations prohibits a mathematical symmetry between electricity and magnetism that would have been at least aesthetically desirable. However, if we allow magnetic charges and currents to exist and we modify Maxwell equations appropriately [59], it takes straightforward algebra to show that the generalized Maxwell equations remain invariant when fields and sources are redefined through ordinary rotations by a real angle θ in the plane $(\mathbf{E},\mathbf{B})$, $(\mathbf{J}_e,\mathbf{J}_m)$ and (ρ_e,ρ_m)[2]. More than leaving the Maxwell equations invariant, the above transformations do not lead to any change in the Lorentz force, the energy density or the Poynting vector. In other words, we may construct several versions of electrodynamics by choosing various values for θ; all of these versions would have been in agreement among themselves[3] [100]. So, what we observe is that maxwellian electrodynamics would have been perfectly *consistent* with the introduction of magnetic charges and currents in the theory; however, there is *no need* to do so.

In 1931, P. A. M. Dirac [38], by considering the quantum mechanics of an electron in an electromagnetic field, showed how quantum mechanics formally allows the existence of magnetic monopoles. There are various formulations of Dirac's original argument [94] [99]; the underlying idea is that the source of the monopole resides in singularities of the electromagnetic field and namely in the vector potential $\mathbf{A}$. A singular $\mathbf{A}$ is to be expected for a magnetic monopole configuration since a regular $\mathbf{A}$ throughout the whole space would had resulted in a divergenceless $\mathbf{B}$[4] and no magnetic charge could exist. By reversing the flow of Dirac's original derivation, let us start by taking a closed surface S which encloses a hypothetical magnetic charge g which resides at the origin of our coordinate system. The magnetic field is radial

[2]For a discussion on this *duality transformation* see ref. [59] p. 252.

[3]The θ=0 case would correspond to ρ_m=0, $\mathbf{J}_m$=0, i.e., the electrodynamics with no magnetic sources.

[4]For a magnetic field $\mathbf{B}$ described by a vector potential $\mathbf{A}$, $\mathbf{B}=\nabla\times\mathbf{A}$ and $\nabla \cdot \mathbf{B}= \nabla\cdot(\nabla\times\mathbf{A})\equiv 0$ everywhere if $\mathbf{A}$ is regular.

and is given by a Coulomb-type law which in spherical coordinates will be like

$$\mathbf{B} = \frac{g}{r^3}\mathbf{r}. \tag{1.1}$$

Gauss's law requires the total magnetic flux Φ through the surface S to be $4\pi g$; thus the vector potential $\mathbf{A}$ corresponding to $\mathbf{B}$ *must fail to represent it* in at least one point on S. Since this argument should hold for *any* closed surface surrounding the magnetic charge, a semi-infinite continuous line ending on g results. This is the so-called *Dirac string* and $\mathbf{A}$ remains singular on it. The Dirac string is a rather unphysical singularity and should remain undetected. This can be achieved as long as the phase $\Delta\alpha$ acquired by an electron's wavefunction when it is transported along a closed path enclosing the *string* is trivial[5], i.e., an integer multiple of 2π. In the presence of the electromagnetic field, the change in phase of an electron's wavefunction is [99]

$$\alpha \rightarrow \alpha - \frac{e}{\hbar c}\mathbf{A}\mathbf{r}, \tag{1.2}$$

and so for a closed path γ surrounding the *string*, the total phase that is picked up is

$$\Delta\alpha = \frac{e}{\hbar c}\,{}_{\gamma}\oint \mathbf{A}d\mathbf{l}. \tag{1.3}$$

From continuity arguments, however, we may see ourselves running into troubles when we allow the closed path γ over which the phase integral 1.3 is performed to continuously deform from a path infinitesimally close to the string, to a point *on* the *string*. As γ contracts on the *string*, the line element over which the phase integral is performed (equation 1.3) vanishes, while $\mathbf{A}$, the vector potential, becomes singular thus leading to indeterminate phases. To overcome this, we ask the wavefunction to *vanish* along the *string*, thus allowing undetermined phases. Going back now to equation 1.3, we may trivially transform it using Stokes' theorem from a line integral

[5]In this interference experiment, the interference pattern is shifted by an integral number of fringes; thus the original and shifted patterns remain indistinguishable.

of **A** to a surface integral of **B**. As γ remains infinitesimally close to the *string*, the surface integral is performed on an arbitrary surface S that does not intercept the *string* and ends on γ; as γ approaches the *string*, the surface S encloses the total flux $4\pi g$ coming from the magnetic monopole. The requirement we have imposed earlier that $\Delta\alpha$ be trivial then becomes

$$\Delta\alpha = 2\pi n \Rightarrow \frac{e}{\hbar c} 4\pi g = 2\pi n \Rightarrow eg = n\frac{\hbar c}{2}. \tag{1.4}$$

This is Dirac's quantization condition. Although it does not prescribe which exactly will be the quantum of the electric or magnetic charge, it shows how electric charges will be quantized if a magnetic charge exists and vice versa. The minimum magnetic charge implied by 1.4 is $g_D = \hbar c/2e = e/2\alpha = 68.5e$ and is referred to as the Dirac magnetic charge. Thus, the importance of Dirac's derivation becomes twofold: it not only shows how quantum mechanics does not preclude the existence of isolated magnetic poles, but it also explains the quantization of the electric charge[6].

1.2 Monopoles in Non-Abelian Theories

In the previous section we outlined in the context of electrodynamics, with the Abelian gauge group $U(1)_{em}$, how magnetic monopoles may be introduced without leading to any problems in the theory. However, although consistent with it, theory finds no need to introduce them except maybe to explain the quantization of the electric charge. One may ask what is our motivation to look for monopoles in theories with higher non-Abelian symmetries.

1.2.1 Grand unification

One of the greatest successes of modern physics has been the application of the principle of gauge invariance to describe the interactions of quarks and leptons by

[6]Let us point out that Dirac's derivation assumes *point* magnetic monopoles and makes no prediction for the monopole's mass whatsoever.

means of Lie group transformations. The "standard model" of our present understanding of particle physics is based on the $SU(3)_C \times [SU(2)_L \times U(1)_Y]$ gauge group where SU(3) describes the gluon structure of QCD and $SU(2) \times U(1)$ is the well-known Glashow-Weinberg-Salam model of the electroweak interactions. The glimpse of unification that the Glashow-Weinberg-Salam model offered us in the breakdown of $[SU(2)_L \times U(1)_Y] \rightarrow U(1)_Q$, provided the starting point for the hunt of the "gauge group of the world" G [47] that will provide the *unification* of all elementary particle forces. The idea is quite simple: we are looking for a *simple*[7] group that unites strong, weak and electromagnetic forces above a sufficiently high mass scale M_X involving a single coupling constant α_X. This Grand Unified Theory (GUT) breaks down to the $SU(3)_C \times [SU(2)_L \times U(1)_Y]$ standard model at the mass scale M_X through the spontaneously symmetry breaking mechanism. Doing simple *rank*[8] arithmetics of the group constituents of the "standard model," we may see why G must have rank greater or equal to four. Georgi and Glashow have shown [47] how SU(5) is the only (among the nine simple rank-4 Lie groups) that can satisfy the requirements in order to be a grand unified group. The unification scale for the minimal SU(5) GUT is $M_X \sim 10^{14}$-$10^{15} GeV$ at which scale the coupling constant is $\alpha_X \sim 1/40$. Since the proposal of the minimal SU(5) GUT, several other GUTs based on groups of higher rank have also been proposed. Among these are the SO(10) (rank-5) and SU(15) (rank-14) groups which break down to the $SU(3)_C \times [SU(2)_L \times U(1)_Y]$ through various alternative chains [32]. These alternative GUTs seem to merit certain features that the minimal SU(5) seems to lack. First of all, a direct consequence of the grand unification is the non-conservation of the baryon and lepton numbers. In every GUT theory, gauge bosons may transform quarks into leptons (and vice versa) thus giving rise to new phenomena like the proton decay. Although the predicted lifetime for the proton τ_p is much greater than the age of the Universe, if we observe the protons contained in a large enough volume of matter, we may find a few of them decaying

[7] A group G is called *simple* if it contains no non-trivial invariant subgroups. If N is a subgroup of G, then N is called *invariant subgroup* of G if for every element n of N, sns^{-1} is also an element of N for every $s \in G$.

[8] Rank of a Lie group is the maximum number of the generators of the group that are simultaneously diagonalizable.

within a few years. Materializing this idea, underground Čerenkov experiments have established a bound for proton's lifetime which exceeds 10^{32} years. Minimal SU(5) predicts a proton lifetime at least an order of magnitude less than the experimentally measured, thus making itself incompatible with the experiment. Further support that rules out the minimal SU(5) comes from precision measurements of the Weinberg angle θ_W; in the minimal SU(5) $\sin^2\theta_W$ is predicted to be 0.214 which should be compared with the experimental value of 0.2331 ± 0.0013 [41]. Although the minimal SU(5) is more or less ruled out, grand unification is by no means dead. GUTs based on higher rank groups seem to predict θ_W and τ_p in accordance with the experiment [46]. Another way of recovering the agreement with the experiment for the minimal SU(5) is by introducing supersymmetry (SUSY). In the minimal[9] supersymmetric SU(5) model, the evolution of α_3 slows down and consequently the unification scale M_X is raised approximately by an order of magnitude compared to the non-SUSY SU(5). The coupling constant at the unification scale reaches a value of $\sim 1/25$ and the predictions for the $\sin^2\theta_W$ and τ_p are increased, thus obtaining agreement with their experimental values [10] [41].

1.2.2 The 't Hooft-Polyakov monopole

The simplest example of a non-Abelian theory is the Georgi-Glashow electroweak model which employs an SU(2) gauge group. Although this theory is not a GUT, it has an interesting feature: it yields monopole solutions. This was shown in 1974 by 't Hooft [105] and Polyakov [92] who proved that genuine magnetic monopoles arise as regular solutions of the field equations within the context of SU(2). The 't Hooft-Polyakov monopole obeys the Dirac-like quantization condition[10] 1.4, but unlike the

[9] i.e., by introducing only one SUSY spinoral operator.

[10] To be exact, the quantization condition obtained by 't Hooft-Polyakov is of the type $ge=1$ (in $\hbar$=c=1 units) which differs from Dirac's condition by a factor 2. This is because the unit charge in the Georgi-Glashow model is $q = \pm\frac{1}{2}e$. With this in mind we may rewrite $ge = 1$ as $gq = \frac{1}{2}$, which is the Dirac condition.

Dirac monopole, it is finite *everywhere*. Its mass is found to be

$$m_M = \frac{M_W}{\alpha_W} C(\beta). \tag{1.5}$$

where M_W and α_W are the intermediate boson's mass and the coupling constant at that mass scale. The $C(\beta)$ is obtained numerically and has a soft dependence on β, the square of the ratio of the Higgs' to the vector boson masses[11]. It can be shown [94] that the monopole solution is a *necessary* consequence of *any* theory in which the electromagnetic group U(1) is embedded in a non-Abelian simple or semi-simple group which undergoes spontaneous symmetry breaking. Within the same theory, electric charge quantization also arises as a consequence of the nontrivial commutation relations that the electric charge operator obeys with other operators in the theory. Grand Unified Theories with symmetries described by a simple non-Abelian gauge group G do embed U(1) and thus yield monopole solutions when G is broken down into a subgroup $H = h \times U(1)$ that contains an explicit U(1) factor. For the minimal SU(5) GUT, equation 1.5 yields a monopole mass of the order of $10^{16} GeV$. However, we may notice that the prediction on the mass of the monopole is rather *soft*: GUTs which undergo spontaneous symmetry breaking at a lower energy scale may yield lighter monopoles while the SUSY extension of the SU(5) or theories like the Kaluza-Klein [94] may yield much heavier monopoles.

1.2.3 Monopoles in cosmology and astrophysics

As we have just seen, GUT monopoles are expected to be superheavy objects, well beyond the energy scales of any present or future terrestrial accelerator. Cosmic Rays on one hand offer a "natural accelerator," appreciably more energetic than any man-made accelerator; however, on the other hand, cosmic rays are still not energetic enough to produce monopoles. The *very early Universe* is thus left as the only place where to look for mechanisms of monopole production; as we will see, the very first

[11] $C(\beta)$ varies from 1 to 1.787 for the two limiting cases of $\beta = 0$ and $\beta \to \infty$.

epochs following the "Big Bang" could have been the "ultimate accelerator," energetic enough to produce magnetic monopoles.

The Early Universe

We have observational reasons [62] to believe that the Big Bang Cosmology is a good model for understanding the evolution of the Universe. In this model the "kinematics" of the Universe is described by the Robertson-Walker spacetime metric while its dynamic evolution is governed by the Einstein-Friedman equations [108]. According to this model, the Universe was once in a singular state (the "Big Bang") where all points of space had zero distance with each other, the density of the matter and the curvature of spacetime was infinite and so was the temperature. Initially, this hot "soup" of matter and radiation had the full, grand unified gauge symmetry restored. But as the Universe cooled and expanded, it underwent a phase transition at a temperature $T=T_C \sim M_X$ (M_X is the typical mass of the heavy gauge bosons of the GUT) at which the expectation value of the Higgs field turned on and the magnetic monopole production started. During this phase transition, the Higgs field acquired vacuum expectation values $\langle\phi\rangle$ which could not be correlated over distances greater than the *horizon* d_H [12] at that temperature. This means that $\langle\phi\rangle$ pointed in different directions in the symmetry space in different domains within which it remained correlated. The monopole configuration arose at the intersection point of several such domains as a stable "topological defect" which was "frozen in." Thus one expects this cosmological production mechanism[13] (also known as the Kibble mechanism [61]) to yield a monopole (or antimonopole) abundance of order one per

[12]Throughout the following few equations we are going to be using some standard quantities that appear in the Einstein-Friedman-Robertson-Walker Cosmology (the so-called "standard" Cosmology). The horizon d_H is the furthest distance traveled by a light signal since $t = 0$. This is the fraction of the Universe that is in causal contact. The Hubble parameter H measures the expansion rate of the Universe. Today's value of H is expressed as $H_0 = h\times$ 100 km sec^{-1} Mpc^{-1} where we bury in h our lack of precise knowledge of H_0. The critical density ρ_C is defined as $\rho_C = 3H^2/8\pi G = h^2 1.88 \times 10^{-29} g cm^{-3}$ and corresponds to the density for a *flat* Universe. The ratio of today's mass density over the critical density ρ_C defines Ω.

[13]The above derivation of monopole density assumes that the phase transition was either second order or weak first order. In the case of a strong first order phase transition, although the picture of how the monopole configuration arises changes [94], a monopole abundance of the same order of magnitude results.

horizon volume

$$n_M \sim \frac{1}{d_H^3} \sim \frac{T_C^6}{m_{Pl}^3}, \tag{1.6}$$

where $m_{Pl} \sim 10^{19} GeV$ is the Planck mass.

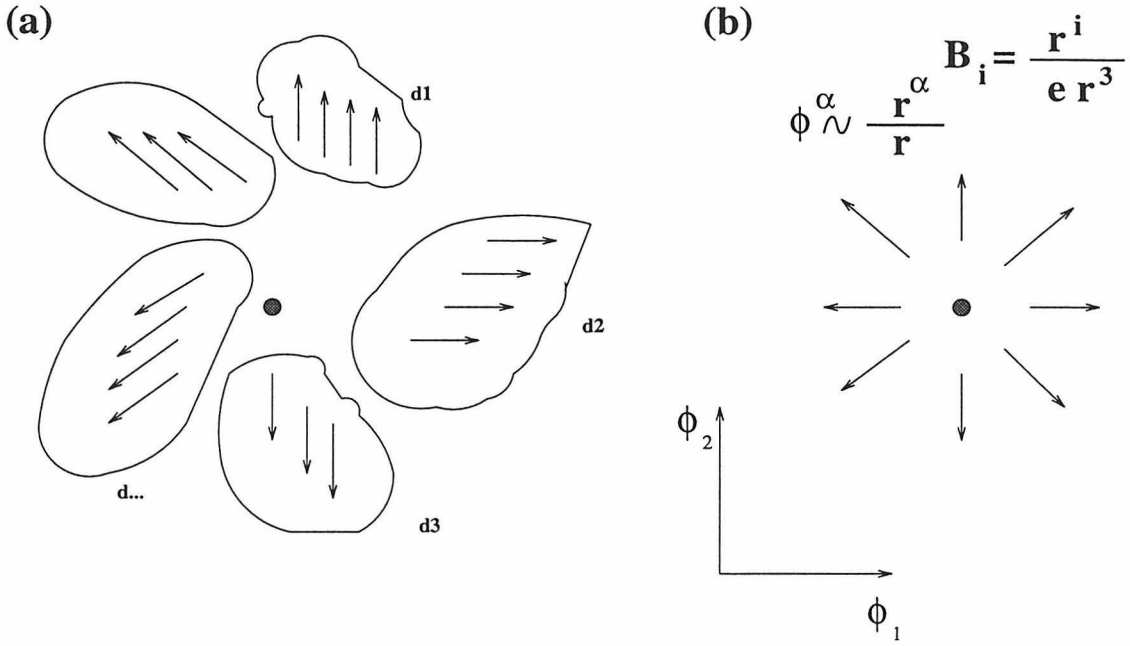

Figure 1.1: (a) Monopole production in the early Universe according to the Kibble mechanism: As the spontaneous symmetry breaking occurs, causally disconnected domains d_i result; in each of these domains $\langle\phi\rangle$ points to different directions of the gauge group. At the point of intersection of several d_i's the Higgs field vanishes, while around it the vector ϕ in the internal space (for simplicity, a two-dimensional space is depicted here) is proportional to the unit vector $\hat{\mathbf{r}}$ in ordinary space. So, in the plot (b) shown here, α refers (i) to the gauge group for the field ϕ and (ii) to the ordinary space for the position vector $\mathbf{r}$. This is the so-called "hedgehog" solution and its topological stability is due to the vanishing of the Higgs field at the origin; there is no gauge transformation that can smoothly deform it into a trivial configuration. The long-range radial magnetic field associated with ϕ is the SU(2) monopole solution ('t Hooft-Polyakov monopole; in the SU(2) model the electric charge unit is half of that of an electron).

Often quoted is the number density n_M divided by the entropy density s; this yields the number density per comoving volume, a quantity that remains constant[14]

[14]This relies on the assumption that monopole-antimonopole annihilation remains insignificant. Calculations [93] show that this is indeed the case for the initial monopole densities we are dealing with.

as the Universe expands [108]:

$$\frac{n_M}{s} \sim \frac{T_C^3}{m_{Pl}^3}, \tag{1.7}$$

where we substituted $s \sim T_C^3$ in equation 1.6. For the nominal values of SU(5), equation 1.7 yields $n_M/s \sim 10^{-12}$. How does this translate in terms of today's cosmological observations? Well, if $\rho_M = n_M m_M$ is the mass density of monopoles today, we may trivially calculate their contribution to the Universe's density in terms of the critical density ρ_C:

$$\rho_M = \Omega_M \rho_C \Rightarrow \rho_M = \Omega_M h^2 1.88 \times 10^{-29} grcm^{-3} \Rightarrow \tag{1.8}$$

$$\Omega_M h^2 \sim 10^{25} \left(\frac{n_M}{s} \frac{m_M}{10^{17} GeV} \right), \tag{1.9}$$

where we assumed [62] in today's Universe $s = 7.04 n_\gamma \sim 10^3 cm^{-3}$. Given the values for n_M/s and m_M, equation 1.9 brings the existence of monopoles seriously at odds with the standard Cosmology which suggests an Ωh^2 of order 1. The value of Ωh^2 obtained from 1.9 would mean that our present Universe would have had an unacceptably high mass density, much larger expansion rate and significantly smaller age than a Universe with no monopoles, all of which contradict with the present measurements [62] of these quantities. This is the so called monopole problem [93] and various scenarios to fix it have been proposed. An ingenious one was proposed by Guth [52]; this is the so called inflationary Universe scenario and its basic idea is that the Universe went through an epoch during which the scale factor R of the Robertson-Walker metric grew exponentially. As the Universe expanded it "supercooled" but it was later reheated again to its pre-inflation level ($\sim 10^{14} GeV$); this process resulted in a huge increase of the entropy. As a result of that, the abundance of any relic (like the monopoles) that was produced before inflation was reduced exponentially by an equally enormous amount down to a negligible level. Although the inflation scenario may drive the monopole abundance to a non-detectable level, it is still an attractive model that gives answers to several cosmological puzzles [52] [62] including

the previously described "monopole problem."

Cosmological Densities

We will leave aside for now the question of what the fate of monopoles in the early Universe might have been and we will try to address the role of magnetic monopoles in the Universe we are observing today. First of all, their mass density can not exceed the present mass density of the Universe. Equation 1.9 can be thus solved with respect to n_M requiring to yield $\Omega_M h^2$ of order one. This places an upper bound to the average monopole number density:

$$n_M \lesssim 10^{-22} \left(\frac{10^{17} GeV}{m_M} \right) cm^{-3}. \tag{1.10}$$

If monopoles are uniformly distributed in the cosmos and they are traveling in random trajectories with typical velocities v_M, the above number density may be used to constrain the average monopole flux:

$$\langle F_M \rangle \lesssim \frac{n_M v_M}{4\pi} \Rightarrow \langle F_M \rangle \lesssim 2.4 \times 10^{-16} \left(\frac{v_M}{10^{-3} c} \frac{10^{17} GeV}{m_M} \right) cm^{-2} sr^{-1} sec^{-1}. \tag{1.11}$$

This picture changes slightly when we consider the role of monopoles in our Galaxy. Observational data concerning the mass density of our Galaxy suggests a local density enhancement of the order of 10^5 (with respect to the mass density of the Universe). Following the same steps as in the derivation above regarding the contribution of monopoles to Universe's mass, we obtain the following upper limit on the monopole flux in the Galaxy:

$$\langle F_M \rangle \lesssim 2.4 \times 10^{-11} \left(\frac{v_M}{10^{-3} c} \frac{10^{17} GeV}{m_M} \right) cm^{-2} sr^{-1} sec^{-1}. \tag{1.12}$$

This limit is valid as long as monopoles can remain gravitationally bound to our Galaxy. But what governs whether monopoles will be gravitationally bound or not?

The Galactic Field Survival

Given their magnetic charge and mass, monopoles are certainly subject to magnetic and gravitational forces. In the absence of these two, relic monopoles would have had a tiny velocity today mainly determined by the energy scale at which they reached kinetic equilibrium and by the subsequent Universe's expansion. The magnetic effect is due to the presence of magnetic fields in our Universe. If we assume that a magnetic monopole[15] –initially at rest– enters a region of size l_c within which the magnetic field remains coherent and of strength B, then simple energy conservation (in the non-relativistic regime) arguments yield that the velocity acquired by the monopole would be

$$v_{mag} = \left(\frac{2g_D B l_c}{m_M}\right)^{1/2} \sim 10^{-3}c \left(\frac{B}{3\times 10^{-6}G}\frac{l_c}{10^{21}cm}\frac{10^{17}GeV}{m_M}\right)^{1/2}. \qquad (1.13)$$

The physical strength of the astrophysical quantities in the above equation have been scaled to the typical ones expected for our Galaxy [107]. The above derivation becomes invalid if a monopole enters a volume of coherent magnetic field with initial velocity $v_0 \gg v_{mag}$; in this case the magnetic field effect is of second order and the *average* energy gained by the monopole is

$$\langle \Delta E \rangle \approx \frac{1}{2} m_M \left(\frac{g_D B}{m_M}\frac{l_c}{v_0}\right)^2 \Rightarrow \qquad (1.14)$$

$$\langle \Delta E \rangle \approx 10^{10}GeV \left(\frac{B}{3\times 10^{-6}G}\frac{l_c}{10^{21}cm}\frac{10^{-3}c}{v_0}\right)^2 \left(\frac{10^{17}GeV}{m_M}\right). \qquad (1.15)$$

In order for monopoles to cluster with our Galaxy they should be able to maintain the typical galactic virial velocity, which is $v_{grav} \sim 10^{-3}c$. Equation 1.13 indicates that monopoles lighter than $10^{17}GeV$ will easily be accelerated to velocities exceeding v_{grav} and thus escape from the Galaxy. A more restrictive limit on m_M may be imposed if the long-term (of the order of the age of the Galaxy) stability of any possible monopole

[15]The magnetic pole is assumed to be of a single Dirac charge g_D.

cluster in the Galaxy is considered; this requires $m_M \gtrsim 3 \times 10^{18} GeV$. Remaining clustered with our Galaxy or not, the above two derivations regarding the interaction of monopoles with the galactic field indicate that monopoles certainly drain energy out of it. Turner, Parker and Bogdan (TPB) [107] have used this to set limits on the monopole flux by demanding monopoles to drain field energy at a rate of the order of the galactic field regeneration by the dynamo action [87] [88] [89].

Let us first assume that monopoles fulfill the mass requirement and remain *bound* to our Galaxy. In this case the gravitational effect on the monopoles is the dominant one while the magnetic field effect is described by equation 1.15. The stability of a domain with coherent B over a period $\tau \sim 10^{15}$sec requires

$$\langle F_M \rangle \times \langle \Delta E \rangle \times (4\pi l_c^2) \times (\pi sr) \lesssim \frac{B^2}{8\pi} \frac{4\pi l_c^3}{3} \frac{1}{\tau} \Rightarrow \tag{1.16}$$

$$\langle F_M \rangle \lesssim 10^{-15} cm^{-2} sr^{-1} sec^{-1} \left(\frac{10^{15} sec}{\tau} \frac{10^{21} cm}{l_c} \frac{m_M}{10^{17} GeV} \right). \tag{1.17}$$

This is the TPB flux limit for monopoles that remain *bound* to our Galaxy. One may notice that $\langle F_M \rangle$ is proportional to the monopole mass m_M: the heavier the monopole is, the larger the monopole fluxes (consistent with the galactic magnetic field regeneration requirements) can be. This is because heavy monopoles are not easily deflected by the galactic field and thus it is harder for them to drain energy out of it (see equations 1.14, 1.15).

If monopoles *do not cluster* with our Galaxy, it is implied that $v_0 > 10^{-3}c$ and the TPB flux limit obtained in this case depends on the relative strength of v_0 and v_{mag}. If $v_0 > v_{mag}$ the galactic field effect is second order, like with the case of clustered monopoles. The TPB flux limit for such monopoles is given by equation 1.17 after only reintroducing the v_0 dependence[16] of $\langle \Delta E \rangle$:

$$\langle F_M \rangle \lesssim 10^{-15} cm^{-2} sr^{-1} sec^{-1} \left(\frac{v_0}{10^{-3}c} \right)^2 \left(\frac{10^{15} sec}{\tau} \frac{10^{21} cm}{l_c} \frac{m_M}{10^{17} GeV} \right). \tag{1.18}$$

[16] In the case we are examining here the monopole initial velocity can have any value greater than $10^{-3}c$.

If $v_{mag} > v_0$, then any infalling monopole will be accelerated to v_{mag} after traversing the first few domains of coherent B. Assuming that any such monopole traverses roughly 100 such domains[17] extracting from the galactic field on the average energy $\sqrt{100} g_D B l_c$ (1.13), TPB find that the maximum monopole flux consistent with the survival of the galactic magnetic field is

$$\langle F_M \rangle \lesssim 10^{-15} cm^{-2} sr^{-1} sec^{-1} \left(\frac{B}{3 \times 10^{-6} G} \frac{10^{15} sec}{\tau} \right) \left(\frac{10^{21} cm}{l_c} \frac{r}{10^{23} cm} \right)^{1/2}. \quad (1.19)$$

One may notice that in this case the obtained limit is independent of the monopole mass as long as $v_{mag} > v_0$. This is because the galactic field energy extracted by the monopole is independent of m_M. Given 1.13, one can trivially see that for monopoles traveling with $v_0 \sim 10^{-3} c$, equation 1.19 is no longer valid if they are heavier than $10^{17} GeV$. The upper flux limit defined by equation 1.19 is often referred to as the "Parker bound." As v_0 increases, the monopole mass for which the "Parker bound" remains valid moves to lower values.

Applying the same idea as in the derivation of the TPB bound, much more restrictive monopole flux limits may be obtained by considering the survival of the intragalactic fields or the magnetic field of neutron stars [49] [97]. Adams et al. [1] have recently reexamined the TPB bound and derived stronger bounds to the monopole flux (at least for monopoles lighter than $\sim 10^{18} GeV$) by considering the survival of much smaller ($B \sim 10^{-20} - 10^{-11} G$) galactic fields over the history of our Galaxy. This is the so-called "extended Parker limit" and for $m_M \sim 10^{17} GeV$ monopoles yields an upper flux $\sim 10^{-16} cm^{-2} sr^{-1} sec^{-1}$.

Other Monopole Attributes

Following our discussion of monopole velocities in our Galaxy, let us point out that Dimopoulos et al. [37] have suggested the possibility that the local monopole flux be as many as eight orders of magnitude larger than the typical galactic flux as

[17] The number of domains is essentially equal to the ratio of the size of the galactic magnetic field ($r \sim 10^{23} cm$) over the nominal size of a domain with coherent B.

monopoles may be gravitationally bound within our solar system. Monopoles bound in our solar system will be traveling with typical velocities as small as $10^{-4}c$, but according to Freese and Turner [45] any enhancement of their local flux would have been insignificant. Another interesting feature of monopoles is that they may come as *dyons*. Dyons are objects carrying both electric and magnetic charges and result from quantum mechanical excitations of a fundamental monopole [94]. Another type of dyon results from the long range interaction of a magnetic charge g and an electric charge q[18]. Bracci et al. [24] have examined the kinematics of the formation and disassociation of the monopole-proton bound system in the early Universe; they concluded that monopoles would most probably have picked up a proton in the early Universe era and that the resulting bound state could have survived until nowadays. The physics of the monopole-proton bound system is closely connected to the Rubakov-Callan effect [27] [98] according to which GUT monopoles may catalyze the decay of a nucleon at a characteristic strong-interaction rate. In the presence of the Rubakov-Callan effect, Bracci's et al. calculation would yield no monopole-proton bound system over timescales greater than the characteristic time of proton capture and decay. The Rubakov-Callan effect would also have contributed to the luminosity of various astronomical objects. Straightforward arguments can show that the observed luminosity of a star will be proportional to the incident monopole flux F_M and to the catalysis cross section σ. Observational limits on the luminosity of neutron stars have been used to set the most stringent upper limits to the monopole flux [36] which are of the order of

$$F_M \lesssim 10^{-23} cm^{-2} sr^{-1} sec^{-1} \frac{10^{-28} cm^2}{\langle \sigma \beta \rangle}. \tag{1.20}$$

Although certain assumptions regarding the age, size, luminosity and monopole capture rate by a neutron star are buried in the equation above, the catalysis cross section remains the most controversial issue.

[18]This could be an electron, a proton or any other nuclei.

1.3 Monopole Solutions Outside GUTs

In the previous sections, we stressed the connection of the monopole solutions with the unification of forces. This, in connection with our arguments in section 1.1 regarding the consistency but not necessity of monopoles in Abelian theories, may lead to the impression that there is no monopole solution outside unification. This is not true. It has been conjectured that within the context of purely Abelian theories, finite energy monopole solutions result when electromagnetism is coupled to a charged vector field W_μ and a neutral scalar field ϕ [64]. The physical significance (i.e., of finite energy or not) of the monopole solutions in this formulation, depends on the relative strength of two terms that appear in the Langrangian L of the theory. These terms correspond to the coupling of W's to the electromagnetic field and to W's self-coupling. Quantization conditions similar to Dirac's are obtained (Q_Me=q where q is an integer or a half-integer in $\hbar$=c=1 units), while the mass of the monopole is of the order of $M_{mon} \sim 1/e^2 R_{mon}$ (in $\hbar$=c=1 units). Within this derivation, an interesting result follows when the theory is coupled to gravity: new class of magnetically charged black holes arise, even when the conditions for finite-energy solutions are not met. In this case the singularity is hidden behind the event horizon of a black hole. Among the predictions for the evolution of these back holes is the emission of magnetic monopoles through Hawking radiation; this can lead to complete evaporation (if the black hole carries an integer multiple of the magnetic charge unit) or to a black hole of minimal half-integer magnetic charge [64].

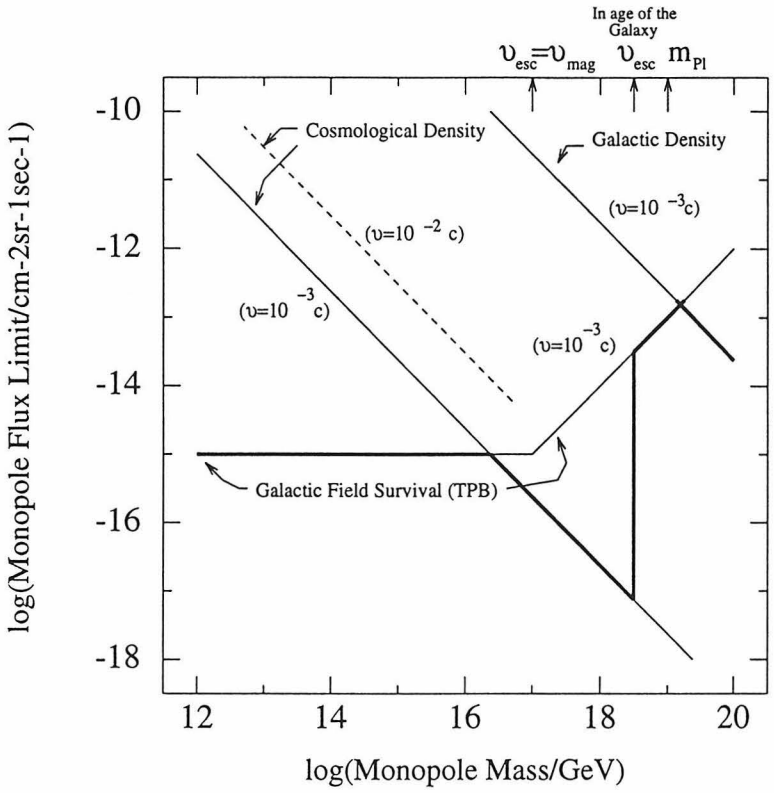

Figure 1.2: Monopole flux limits derived from cosmological and astrophysical considerations. The mass density limits are for monopoles uniformly distributed in the Universe and clustered in our Galaxy. The dashed line corresponds to monopole making up the Universe's critical density and traveling with $\beta \sim 10^{-2}$. The flux curves derived from mass density arguments assume certain values for the Ω and h. The reader should keep in mind that variation in the Ωh^2 by one order of magnitude is nominally allowed by the observational data; this would shift these curves parallelly to themselves. For the limit derived from the galactic magnetic field survival arguments (TPB), the nominal values for B, l_c, τ and r have been assumed (see text for details). The three mass scales that are indicated with an arrow correspond to (i) the monopole mass at which the velocity acquired by a monopole (initially at rest) equals the galactic escape velocity, (ii) the minimum monopole mass in order for monopoles to remain clustered over the age of our Galaxy and finally (iii) the Planck mass scale $m_{Pl} \sim (\frac{\hbar c}{G})^{1/2}$. The heavy dark curve shows the combined upper monopole flux limit based on mass density and field survival arguments. Finally, let us point out that although not plotted here, the monopole catalysis of nucleon decay sets significantly stringent limits (8 ± 4 orders of magnitude lower than the Parker bound) when applied to the luminosity of various astronomical objects. However, the whole phenomenon of monopole catalysis and its cross section remain controversial.

1.4 Monopole Detection

The physics of the supermassive magnetic monopole has stimulated intense activity among the experimenters. Soon after the GUT monopole postulation, physicists all around the world started working on setting up little traps to catch a monopole. The first thing that everyone realized was that monopoles can not be created in anybody's terrestrial laboratory. Because of their enormous mass, monopole detection must necessarily involve searching for Big Bang relics in the cosmic rays. The techniques involved in this hunt for the GUT monopole reflect the various phenomena that arise from the interaction of monopoles with matter and the production of signals that can be recorded by detectors. These experimental techniques can be generally divided into three categories: induction, ionization and catalysis of proton decay.

1.4.1 Induction

This is probably the most elegant monopole detection technique since it relies on the sole requirement a particle has to fulfill in order to qualify as a monopole: to possess magnetic charge g. The uniqueness of the induction is that it measures directly and unambiguously g without any assumptions regarding the mass, velocity or companion electric charge of a monopole. The detection of a (moving) magnetic charge with the induction technique is based on the long range electromagnetic interactions between the magnetic charge and the macroscopic state of a superconducting ring through which it travels. As it can be derived directly from the generalized –so that to include magnetic sources– Maxwell equations [26], the passage of a magnetic monopole through a superconducting ring results in an induced current I which is an integer multiple of twice the superconductivity quantum $I_0 = hc/2eL$, where L is the self-inductance of the ring. Blas Cabrera of Stanford University first reported in 1982 [26] on a monopole candidate recorded in his four-turn, $20cm^2$ superconductive loop. Although the event was believed to be of spurious cause, over the following decade several experimental groups [49] have focused their work in this field. The greatest challenge of the induction technique is the requirement to keep the ambient field fluc-

tuations to less than 1 part in 10^{11} of the earth's magnetic field. Several approaches to this problem have been proposed [21]; however, the difficulties of implementing these demanding technologies on large scales prevent the induction technique from probing monopole flux limit at or beyond the Parker bound[19]. Cabrera's original (1982) measurement yielded an upper monopole flux limit[20] of $1.4 \times 10^{-9} cm^{-2} sr^{-1} sec^{-1}$. Since then, the total exposure of induction detectors to monopole fluxes has been increased by almost four orders of magnitudes resulting in a present global induction limit [22] [55] of $2.14 \times 10^{-13} cm^{-2} sr^{-1} sec^{-1}$. Among the most stringent induction limits were obtained by the IBM group [22] ($3.8 \times 10^{-13} cm^{-2} sr^{-1} sec^{-1}$) and the Stanford group [55][21] ($7.2 \times 10^{-13} cm^{-2} sr^{-1} sec^{-1}$).

1.4.2 Ionization

It is well established from the study of the passage of energetic electrically charged particles through matter that they interact with the atomic electrons of the medium via their electric field thus resulting in the ionization and/or excitation of the medium[22]. In the case of a magnetic monopole moving in matter, atomic electrons are still subject to the monopole's magnetic field via the Lorentz force. This may lead to ionization and/or excitation of the medium like in the case of electrically charged particles. The significance of this is apparent since there are known materials (such as scintillators, gaseous tubes or track-etch) which respond to these processes by producing detectable signals. All of these detectors reflect well-known technologies and most importantly they are fairly inexpensive; thus any monopole search utilizing any of these techniques can probe within reasonable timescales very low monopole flux limits. However, un-

[19] For the IBM $\sim 1m^2$ superconducting detector [22], more than 500 years of data taking would be needed in order to reach the Parker bound ($10^{-15} cm^{-2} sr^{-1} sec^{-1}$). One has to double this period of time if one takes into account that during its 40 month (calendar time) operation the IBM detector collected data for only half of the time.

[20] All the direct experimental results on the upper limit of monopole flux are quoted at the 90% confidence limit ($ln10/\int dAd\Omega dt$).

[21] Actually, in this article, the Stanford group suggested that "the entire data set from the prototype (Cabrera 1982) detector which contains the single event should be discarded when quoting particle-flux limits for cosmic-ray magnetic monopoles."

[22] The energy that is lost in these inelastic collisions of a charged particle with the atomic electrons of the medium they traverse is often referred to as *electronic energy loss* or *electronic stopping power*.

like the induction method, all of these techniques suffer from strong dependence on the projectile's velocity. Thus a good understanding of the energy loss mechanisms as a function of the monopole's velocity is necessary.

Studies of energy losses of magnetic monopoles in matter have been strongly benefited from analytical calculations and experiments regarding the interaction of electrically charged particles with matter. So far, the Bethe-Bloch formula corrected for the *density* and *shell* effects [65] describes reasonably accurately the ionization of heavy relativistic electrically charged particles in matter. The usual prescription for obtaining an equally reliable formula for fast magnetic monopoles is through the question of what relativistic electric charge will mimic a magnetic monopole. This trivially leads to the observation that the force which the atomic electrons are subject to upon the passage of a monopole corresponds to an equivalent electric charge $(Ze)_{mon}$ of $g\beta$, where g is the strength of the magnetic pole and βc its velocity. This results to an approximately constant energy loss rate $[(Ze/\beta)^2 \rightarrow g^2]$ which for a monopole with a single Dirac charge $g_D = 68.5e$ translates to almost $68.5^2 \simeq 4700$ times the energy loss of a singly electrically charged minimum ionizing particle in the same medium. Ahlen [2], using semiclassical methods, derived the Bethe-Bloch analog for magnetic monopoles; his derivation yields several correction factors to the naively modified Bethe-Bloch formula we proposed earlier and improves significantly the dE/dx calculation for monopoles traveling with velocities greater than $10^{-1}c$. For monopoles (but also for electric charges) traveling with velocities less than $10^{-1}c$, the Bethe-Bloch type of energy loss formula breaks down as certain assumptions upon which it is based are no longer valid. This is because as the particle slows down, large-impact collisions become *adiabatic*[23] while small-impact collisions can no longer treat the atomic electrons as free[24]. For $\beta < 0.01$, Lindhard et al. [66] [67] have calculated electronic energy losses of charged particles by assuming that the projectile passes through a degenerate Fermi gas of noninteracting electrons; as the projectile's

[23]This is because the time scale over which the perturbation caused by the particle takes places is comparable to the period of the bound electron.

[24]This is because the kinematically limited energy transfer from a monopole to a free electron ($\sim 2mc^2\beta^2\gamma^2$) is no longer much larger than the atomic-electron energies.

velocity decreases, fewer electrons of the Fermi sea are "available" for ionization and thus a linear dependence of the electronic stopping power as a function of the incoming particle's velocity is obtained. The Lindhard theory had a remarkable success in predicting the energy loss of slow protons in matter and since then it has been applied successfully to the phenomenology of the passage of most of the slow ions through matter [109]. Ahlen and Kinoshita [3] applied Lindhard's technique in order to derive energy loss formulas for monopoles traveling with velocities $v < 10^{-2}c$. Not surprisingly, they obtained a linear velocity dependence for the monopole's ionization losses,

$$\left(\frac{dE}{dx}\right)_{elec} = Cg^2v, \tag{1.21}$$

where v and g are respectively the velocity and the strength of the magnetic monopole. The constant of proportionality C that enters in the above equation is material-dependent and is determined by the macroscopic characteristics of the Fermi gas, i.e., from its plasma frequency ω_p and its Fermi velocity v_F. Its explicit form is derived by Ahlen and Kinoshita [3]. As an example, let us simply mention that equation 1.21 for monopoles in silicon yields $dE/dx \simeq (45GeV/cm)(g/g_D)^2(v/c)$. The lowest $\beta = v/c$ for which this formula remains valid comes from kinematic arguments; these limit the lowest β of the projectile to that transferring the minimum energy E_{th} in order for excitation or ionization to occur. Given that the maximum possible energy transfer to an electron is of the order of $2m_e v_F v$, the kinematic limit is in the $10^{-4} - 10^{-3}$ β range if we assume E_{th} of few eV.

Scintillators

Our previous discussion on the monopole ionization has been more of a general guide rather than a direct evaluation of the response of ionization detectors to monopoles. Scintillators have been known since a long time as materials that respond to the ionization and/or excitation of charged particles. The energy absorbed by these materials is reemitted in the form of visible light because of the *luminescence* property that these materials exhibit. Generally speaking, the light output L of a scintillator

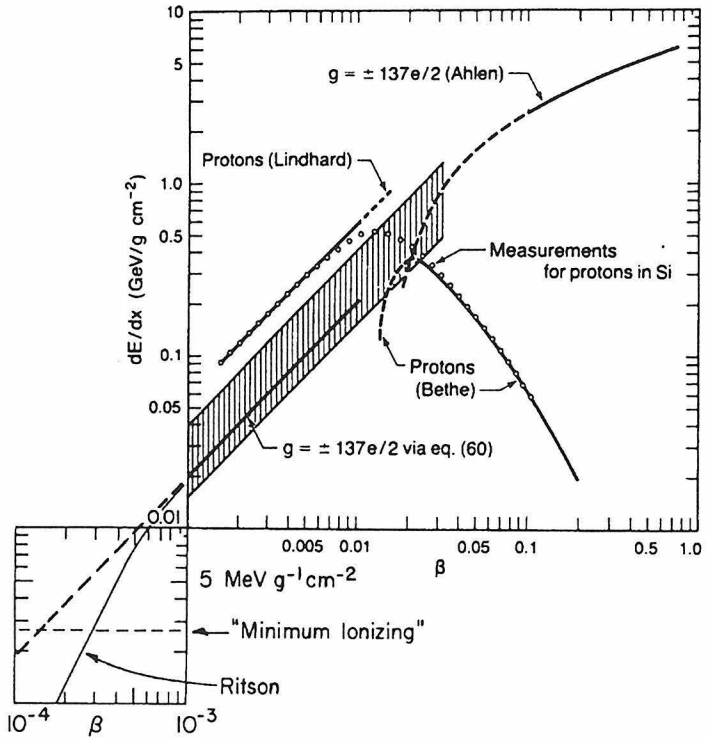

Figure 1.3: Energy loss for monopoles of a single Dirac charge (g_D) in Silicon. Experimental data (open circles) for protons in Silicon are also shown. The solid curves are calculated from the corresponding theoretical work mentioned in parentheses. The solid curve inside the shaded region shows the Ahlen and Kinoshita result for monopoles [3]. The extension of this curve below $10^{-3}c$ assumes no velocity cutoff due to E_{th}, while the one labeled as "Ritson" tries somehow to take this into account. The figure is reprinted from D. E. Groom's 1986 review article.

can be considered as a linear function of the deposited energy E. Deviation from this linear response is observed on large energy depositions when quenching interactions between the excited molecules created along the path of the incident particle start taking place (see [65] and references therein on *Birks'* formula). Ahlen and Tarlé addressed the problem of the light yield L of magnetic monopoles in scintillators. In their 1983 article [5], they derived the expected specific light yield (dL/dx) for monopoles of various velocities. By assuming the same scintillation efficiency as the one for protons and by using their earlier energy loss calculations for monopoles [2] [3], they have shown that monopoles faster than $\sim 3 \times 10^{-3}c$ are expected to be producing *at least* 20 times the scintillation light of the minimum ionizing particle

(see figure 1.4). However, their most intriguing conclusion was with regards to the minimum particle velocity to which scintillators could respond. As we have mentioned earlier, the simple two-body kinematics limits the maximum transferable energy to an electron. By assuming an $E_{th} = 5eV$ resulting from the scintillator's band structure, Ahlen and Tarlé suggested that the velocity threshold in order for scintillation to occur is of the order of $v_0 \sim 6.5 \times 10^{-4}c$; this threshold defines automatically the lower monopole velocity at which any monopole search could be sensitive to [4].

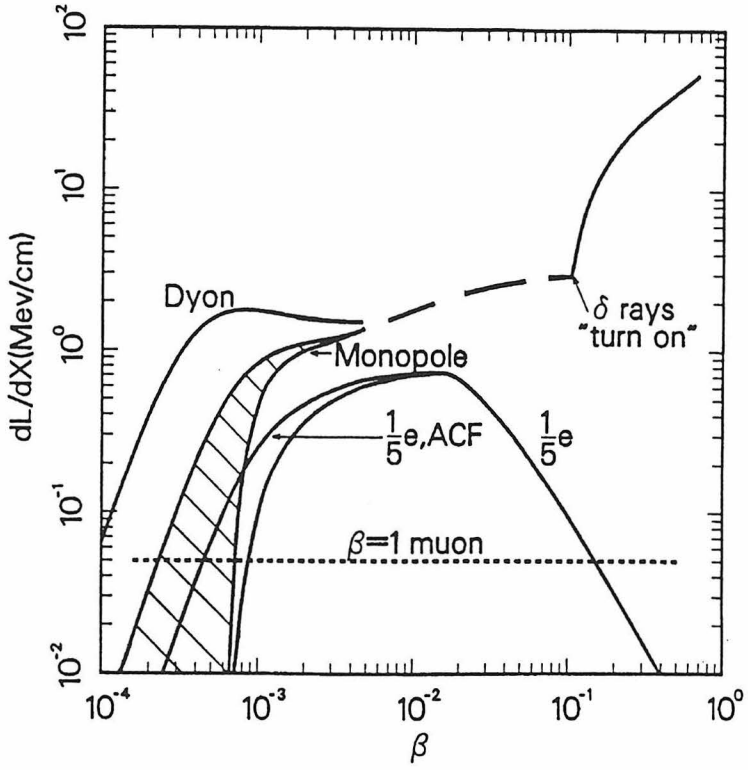

Figure 1.4: Light yield of bare monopoles in scintillator. This reflects mostly the work of Ahlen and Tarlé who adapted previous energy loss calculations for monopoles to estimate monopole's scintillation yield. In the shaded region one can see (lower curve) the conservative Ahlen-Tarlé velocity threshold for a $5eV$ energy gap model. The upper curve within this shaded region reflects the Ficenec's et al. work who modified Lindhard's stopping power with an adiabatic factor in order to fit their slow proton data. For comparison, the light yields for dyons, fractionally charged particles and minimum ionizing muons are also shown. The figure is reprinted from reference [43].

The question of how scintillators respond at particle velocities less than $10^{-3}c$ gave rise to various experiments [6] [43] which were aimed exactly at testing the applica-

bility of scintillators in monopole searches. In the most recent of these experiments [43], Ficenec et al. used slow neutrons in order to produce recoil protons within the scintillator. They were able to observe scintillation coming from $400eV$ protons which correspond to a β of 2.5×10^{-4}. Their result clearly suggests that the sharp kinematic cutoff in the particle's velocity that Ahlen and Tarlé put forward was rather over-conservative[25] and additional light production is to be expected in the velocity regime of $v < 10^{-3}c$.

Several groups around the world [14] [49] have utilized scintillator detectors to search for magnetic monopoles. To this day, the limit set by the Baksan detector [7] represents the best one set by a scintillator experiment for monopoles traveling at velocities $10^{-3}c < v < 10^{-1}c$. This limit stands at $6.8 \times 10^{-16} cm^{-2} sr^{-1} sec^{-1}$. Let us point out that the sensitivity of most scintillator experiments drops significantly at or below $\beta \sim 10^{-3}$ and the limits on the monopole flux set below this velocity still remain at least an order of magnitude above the Parker bound.

Gaseous Tubes

Gaseous detectors represent another class of devices able to detect ionizing radiation. In this kind of detectors, the incident radiation produces a number of electron-ion pairs which under the action of the (externally applied) electric field drift towards the anode and cathode respectively. The signal out of the gaseous detector is a current (voltage) signal which can be processed further by the electronics. The treatment of monopole energy losses in gaseous detectors follows the general arguments of Ahlen et al. that we presented earlier. Given the typical excitation potentials ($\sim 10eV$) for most of the (noble) gases used in gaseous tubes, the two-body-collision velocity threshold can easily be derived to be of the order of $10^{-3}c$. However, for a slow monopole passing near an atom, Drell et al. [40] have first described an interesting effect (referred to as the *Drell* effect) that can lead to much larger energy losses. This effect consists of a possible rearrangement of the atomic angular momentum that

[25] It is suggested by the authors in article [43] that the absence of a sharp velocity cutoff is probably due to either level mixing effects or underestimation of the contribution of high momentum electrons to dE/dx.

results from the angular momentum deposition that occurs when a monopole passes close to a target atom. This effect can lead to excitation cross sections significantly larger than the one expected from the Ahlen and Kinoshita treatment of monopole energy losses. After Drell's et al. original derivation of energy losses of slow monopoles in H and He, more detailed calculations for the case of multi-electron atoms followed [90] [103]. By using the most recent numerical calculation of reference [103], we find the energy loss rate for monopoles in Helium to be

$$\frac{1}{\rho}\frac{dE}{dx} = 119\beta\left(1-\frac{\beta_c^2}{\beta^2}\right)^{3/2} GeVg^{-1}cm^2, \tag{1.22}$$

where βc is the monopole's velocity and β_c is the "critical" velocity that accounts for the nucleus recoil effect; this defines the minimum threshold above which the above equation is valid. For the case of Helium, $\beta_c \approx 9.242 \times 10^{-5}$.

The exploitation of the Drell effect in monopole detection with gaseous detectors relies on the so-called *Penning* effect. The Penning effect is a well-known secondary mechanism for ionization in gases; according to this, the deexcitation of metastable states of the primary gas may proceed through collisions with the atoms of a second gas present in the mixture thus resulting in the ionization of the latter. In this way, the Drell-Penning effect becomes the primary tool for extending the sensitivity of monopole searches with gaseous detectors below $\beta \sim 10^{-3}$. In order to do so, not only the primary gas component has to exhibit the Drell effect, but the secondary one (in most cases the quencher) has to have an ionization potential less than the deexcitation energy of the primary's in order for the Penning effect to take place.

The Drell-Penning effect we have just described has been applied in the search for magnetic monopoles by various groups [49]. The UCSD group has reported [25] the best monopole flux limit covering almost the full range of the expected monopoles velocities. After 578 days of data taking, their $265m^2sr$ gaseous detector set an upper monopole flux limit of $1.8\times10^{-14}cm^{-2}sr^{-1}sec^{-1}$ which is valid for monopoles in the β range of $1.1\times10^{-4} < \beta < 1$. The gas mixture that they have used was of He-CH_4-H_2 in an 80%-19%-1% proportion and thus allowed them to exploit the Drell-Penning

effect for monopoles with $\beta < 10^{-3}$. Among the most recent monopole searches by means of gaseous tubes is the one reported by the SOUDAN 2 collaboration [106]. The gas mixture used in this detector has been an Ar-CO_2 (85%-15%) which, however, does not have a well-established Drell-Penning effect. After almost three years of data taking, SOUDAN 2 reported an upper monopole flux of $8.7 \times 10^{-15} cm^{-2} sr^{-1} sec^{-1}$ which is valid for monopole velocities greater than $2 \times 10^{-3} c$.

Track-Etch

The track-etch detectors is another family of solid state detectors known to respond to the electronic energy losses of electrically or magnetically charged particles [44]. The passage of such particles through the track-etch material leaves a trail of local radiation damage which may become visible when the material is treated with a suitable chemical etchant. We will postpone until the next chapter the details of the operation of such a detector. Here, let us point out that the sensitivity of these detectors to ionization has been well established for electrically charged particles traveling as slow as $10^{-2} c$. Given the fact that monopoles are expected to be extremely ionizing (see figure 1.3), track-etch detectors may enjoy sensitivity to monopoles with $10^{-2} \lesssim \beta \leq 1$. However, any sensitivity of the track-etch detectors to monopole velocities less than $10^{-2} c$ requires an ability of these detector to respond to the energy that a monopole loses in *elastic collisions* with the target nuclei[26]. Price et al. [95] [96] have studied the capabilities of the muscovite mica and the CR39 track-etch detectors for monopole searches and suggested that these two represent the most powerful tools for probing monopole fluxes below the Parker bound and with sensitivity to velocities below $10^{-3} c$.

What makes the muscovite mica [96] a powerful monopole detector is its unsurpassed integrated exposure (several hundreds of Myr) and the fact that it responds

[26]This energy loss mechanism is often referred to as the nuclear stopping power and obviously does not fall in the energy loss mechanism we are discussing in the section, i.e., the electronic ionization and excitation. However, for the sake of completeness, we will make a short mention of it here in order to present relevant monopole flux limits that were obtained with these assumptions. A more detailed discussion on the role of the nuclear stopping power in the monopole searches with track-etch detectors will follow in chapter 2.

to nuclear recoils that are produced when monopoles bound to heavy nuclei (heavier than $Z = 10$) travel through it. Mica's sensitivity peaks at velocities of $\sim 10^{-3}c$, where the stopping power is found to have its maximum value. The flux limit obtained from the analysis of the old mica [96] is at $\sim 10^{-18} cm^{-2} sr^{-1} sec^{-1}$ and it is the lowest one obtained from any terrestrial search for magnetic monopoles. Let us mention that for bare monopoles the stopping power does not exceed mica's sensitivity threshold and thus the above flux limit *does not apply.* Aside the uncertainties related to the *history* of the pieces of old mica that were searched, the monopole catalysis of nucleon decay and/or the formation of monopole-proton bound states in the early epochs of the Universe (see section 1.2.3) could severely affect the mica result making it completely *invalid* if monopoles do catalyze the nucleon decay or *all* the monopoles are positively charged dyons (composite or not).

The CR39 is one of the new generation track-etch detectors which enjoy high sensitive without being forbiddingly expensive. In addition to that, Price has shown [95] that the diamagnetic repulsion of the atoms in the CR39 may lead to extra sensitivity at monopole velocities around $\sim 10^{-4}c$. Orito et al. [86] utilized a $2000m^2$ array of CR39 detectors which they deployed underground in Ohya, Japan; after 2.1 years of exposure they set an upper monopole flux limit at $3.2 \times 10^{-16} cm^{-2} sr^{-1} sec^{-1}$ in the velocity range $10^{-2}c < v < c$. From the same analysis, a limit of $3.7 \times 10^{-15} cm^{-2} sr^{-1} sec^{-1}$ may be applied to monopoles with velocities $4 \times 10^{-5}c < v < 2 \times 10^{-4}c$ *if Price's prescription regarding the diamagnetic repulsion of the CR39's atoms may lead to etchable tracks in the CR39 detectors Orito et al. have used.*

1.4.3 Catalysis of proton decay

The possible ability of monopoles to catalyze nucleon's decay (see section 1.2.3) may be observed in a terrestrial proton decay detector, thus allowing monopole upper flux limits to be set in the case of a negative search. Monopole flux limits obtained in this way are –in general– difficult to interpret and to compare amongst each other as different authors adopt different catalysis cross section σ. In searching for monopoles

via the catalysis of proton decay, an assumption on σ needs to be made in order to estimate $\lambda_{cat} = 1/(\sigma N_N)$, the mean distance between catalyzed nucleon decay interactions. The IMB group has recently reported [19] upper monopole flux limits based on the combined analysis of data they collected over most of their proton decay detector's livetime. Their limit stands at $2.7 \times 10^{-15} cm^{-2} sr^{-1} sec^{-1}$ for monopoles traveling with $\beta \sim 10^{-3}$ and catalyzing proton decay with a cross section of $\sigma \approx 10^{-24} cm^2$. For slower moving monopoles ($10^{-4} < \beta < 10^{-3}$) and lower cross sections ($\sigma = 10^{-25} cm^2$), their upper flux limit is $1.0 \times 10^{-15} cm^{-2} sr^{-1} sec^{-1}$. Let us point out that the 1984-89 search for magnetic monopoles at the Lake Baikal deep underwater experiment [23] has set monopole flux limits by roughly an order of magnitude lower than the IMB limits we have just mentioned. However, in doing so the Baikal group has assumed a significantly enhanced catalysis cross section ($\sigma > 10^{-22} cm^2$). Terrestrial searches for monopoles catalyzing proton decay, besides complimenting the indirect astrophysical limits (see section 1.2.3), can actually compete with them if they achieve sensitivity to catalysis cross section *lower* than the ones assumed for the derivation of the astrophysical limits.

1.5 Is There Any Place Left for a Massive Magnetic Monopole to Hide? [27]

We have just seen how magnetic monopoles arise in Grand Unified Theories as stable, superheavy particles carrying magnetic charges. These monopoles will most probably be traveling with a velocity close to $10^{-3}c$, the characteristic velocity of the galaxy's or supercluster's gravitational potential, while monopoles bound in our solar system are expected to have typical velocities of $10^{-4}c$. Various theoretical arguments based on the properties of the GUT monopole (i.e., its charge, heavy mass and its ability to catalyze nucleon decay) provide guidance for their expected abundances. However, these predictions vary over a significant range of values with inflation being able

[27] The title of this section is borrowed from D. E. Groom's paper contribution to the 3rd Conference on the *Intersections between Particle and Nuclear Physics*, Rockport, Maine, May 14-19, 1988.

to drive the monopole abundance as low as one monopole within the present event horizon. The Parker bound remains the least speculative and most reliable one; it relies on parameters that we know better than any other astrophysical quantity; that is why it is widely accepted as the benchmark for all the terrestrial monopole searches. Although induction would have been the desirable technique for any monopole search, the demanding technologies forbid it from large acceptance applications. This leaves traditional and generally inexpensive ionization detectors as the only tools to probe monopole limits beyond the Parker bound. Ficenec's et al. measurement raised our confidence on the use of conventional scintillator detectors to look for monopoles. On the other hand, the Drell-Penning effect and the diamagnetic effect in CR39 suggested two new ways for extending the sensitivity of traditional ionization detector to lower monopole velocities.

This has been the theoretical and experimental background within which the MACRO collaboration was born. The aim of the collaboration has been to build a detector with high *collecting power* so that to probe beyond the Parker bound and *sensitive* enough so that to remain powerful over the whole range of possible monopole velocities while offering something that no other monopole detector had offered before, *multiple signatures* of the same rare event. The result of this collaboration –the MACRO detector at Gran Sasso– will be presented in detail in the next chapter.

Chapter 2

The MACRO Detector at Gran Sasso

The **Monopole, Astrophysics and Cosmic Ray Observatory** (MACRO) is one of the new generation multi-purpose underground experiments, built primarily to search for rare events in the cosmic radiation with high sensitivity and redundancy. The MACRO detector was made possible thanks to the large experimental halls of the Laboratori Nazionali del Gran Sasso (LNGS) of the Istituto Nazionale di Fisica Nucleare (INFN) in Italy.

2.1 The Gran Sasso Laboratories

In the early 1980's, the construction of the Rome-Teramo highway in central Italy gave birth to the Laboratori Nazionali del Gran Sasso. Located approximately underneath the tallest point of the Appenines –the so-called Gran Sasso (the big rock)– the newborn laboratory was named after that. The latitude and longitude of the Laboratory are 42°27′09″ North and 13°34′28″ East respectively, while the altitude is 963m above sea level. The rock overburden the laboratory consists mainly of calcareous-dolomite ($CaCO_3$, $Ca_2Mg(CO_3)_3$, $CaMg(CO_3)_2$) limestone with an average density $\rho = 2.71 \pm 0.05$ g/cm^3, average atomic number of 11.4 ± 0.2 and average atomic weight of 22.9 ± 0.4 [11]. The rock shields the laboratory from cosmic ray muons by a factor of 10^6. It has a minimum thickness of approximately 1160m, while the average thickness is around 1400m. The minimum energy for a muon at the top of the mountain to reach the laboratory is approximately 1.4TeV. The general layout of the LNGS is shown in figure 2.2; it consists of three main underground Halls, all of which have overall approximate dimensions of 100m×17m×17m. The experimental halls have direct connection to the westbound highway tunnel, thus allowing straightforward

access using motor vehicles. The easy access to the underground facilities is one of LNGS' important advantages. There is also an external laboratory which provides ample office space and computer facilities. Fiber optics provide computer connection between the underground and external laboratory. The main physics objectives of the LNGS experiments [58] include –but are not limited to– the search for magnetic monopoles, the solution of the solar neutrino problem, the detection of neutrino from collapsing stars, the atmospheric neutrino problem and its connection to neutrino oscillations and the study of high-energy primary cosmic rays. The favorable azimuthal direction of the LNGS with respect to a possible neutrino beam coming from CERN has given rise to interesting ways of studying neutrino oscillations in the future [42] [57].

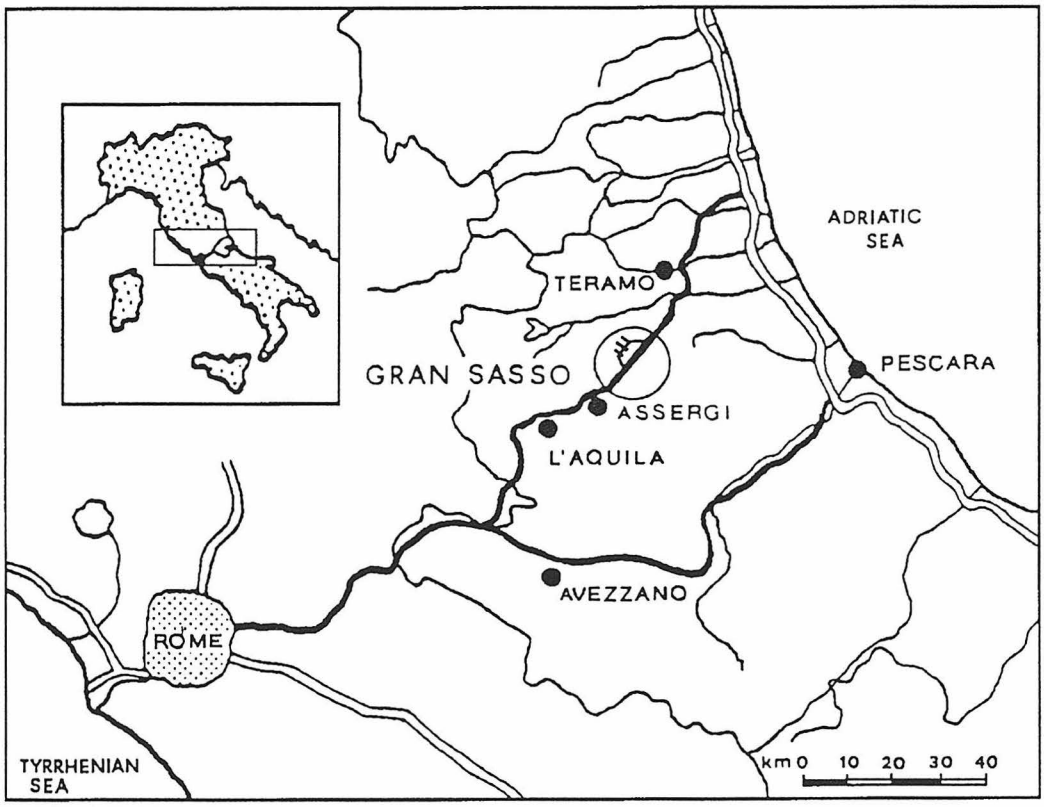

Figure 2.1: Map of central Italy. LNGS is located approximately 120km east of Rome on the north side of the A24 highway.

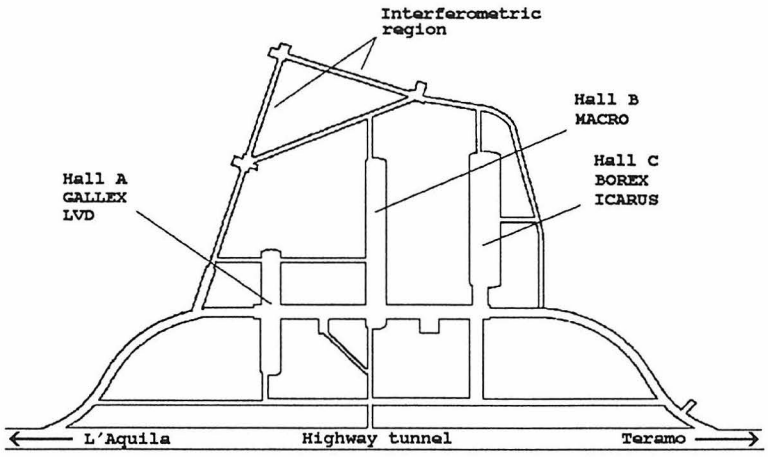

Figure 2.2: Underground facilities of the Laboratori Nazionali del Gran Sasso.

2.2 General Layout of the MACRO Detector

The MACRO detector is located in Hall B of the underground facilities of the LNGS. Its design philosophy was dictated by its primary objective: the search for magnetic monopoles. Probing monopole limits at the astrophysical level requires detector with large acceptance and of course redundancy. There are only a few events expected to be recorded during the experiment's lifetime, making thus apparent the need for multiple signatures of the same event. The overall dimensions of the detector are 77m×12.3m×9.9m and provide an acceptance of approximately 10,000m^{2}sr to an isotropic flux of particles. Given the size of the detector, basic modularity is an absolute necessity. The "unit" in the overall construction of MACRO is the so-called "supermodule" (SM). Each supermodule consists of a lower part (lower SM) with overall dimensions 12m×12m×5m and a vertical extension referred to as "attico," which brings the total height of a supermodule to 9.9m. There are six such supermodules making up the full detector.

Figure 2.3 shows a drawing of how MACRO looks today in Hall B of LNGS. A cross-sectional sketch of the lower part of a supermodule of the MACRO detector is depicted in figure 2.4; in this sketch we may identify the three detection systems that

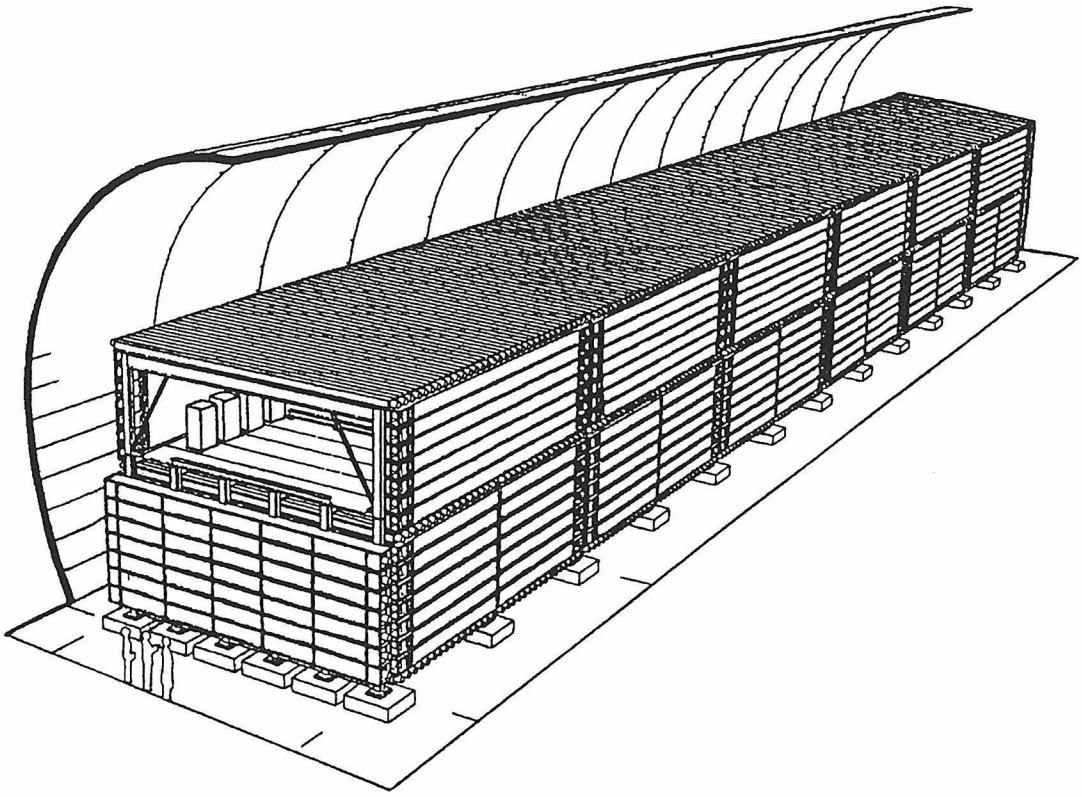

Figure 2.3: General layout of the full MACRO detector (as is today) in hall B of the LNGS.

are employed in MACRO: scintillators, streamer tubes and track-etch. The whole detector body is almost completely surrounded by scintillator counters, while an additional horizontal layer of scintillator counters exists in the middle. This scintillator layer will be referred to as "center," while the other two horizontal layers lying underneath and above it will be referred to as "bottom" and "top" respectively. Of the vertical faces of the detector, we identify –based on their orientation– the "east," "west," "north" and "south" scintillator layers[1]. Although the east and west layers extend to the full height of the detector, the north and south ones cover only the lower half. This is in order to allow access to the "attico," the volume between the center and top layers which houses the electronics of the detector. The scintillator system is

[1]The reference to the scintillator counters by these names (bottom, center, west, east, etc.) will be quite frequent in the subsequent chapters, and unless otherwise specified, it will imply the whole layer or "face" of the whole detector or of one of its supermodules.

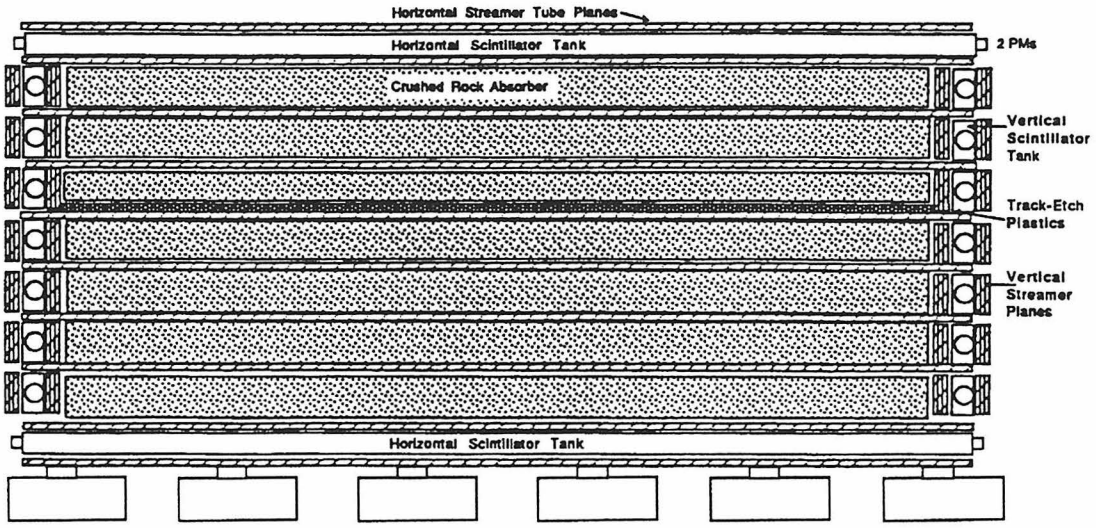

Figure 2.4: Cross-sectional end view (not to scale) of the lower part of a MACRO supermodule.

described in more detail in the next section. Each horizontal scintillator layer is sandwiched between two planes of limited streamer tubes, while vertical scintillator layers are sandwiched between three streamer tube planes. There is more than 99% overlapping of the sensitive areas of both systems. In addition to the streamer tubes located in the immediate vicinity of the scintillator counters, six equidistant horizontal planes of streamer tubes are placed between the center and bottom scintillator layers. These inner planes are separated by passive absorber $\sim 60 g/cm^2$ thick. The seven layers of absorber present in the lower half of MACRO set a minimum threshold of $\sim 1 GeV$ for vertical muons to cross the apparatus. They also prevent delta rays from hitting multiple streamer tubes. The streamer tube system of MACRO is described further in section 2.4. Finally, layers for track-etch detectors are placed in the middle of the lower MACRO and on the east and north faces. Each track-etch module is made of three layers of Lexan and three layers of CR39, while a layer of aluminum absorber is placed among them. The absorber is there in order to prevent heavily ionizing nuclear fragments from traversing all of the six layers of Lexan and CR39 detectors, something that is expected in the case of a magnetic monopole. While scintillators and streamer tubes are the active (i.e., self-triggered) systems of MACRO providing

timing, ionization and pointing information, the track-etch system is passive and it provides confirmation and redundant ionization information in case a monopole candidate is identified by the scintillator and/or streamer tube electronics. MACRO's track-etch system is presented in more detail in section 2.5. The lower part of the first supermodule of MACRO[2] was first put in operation in February 1989. This first run proved sound the original detector design; there were only few modifications –mainly of the electronics– that followed. The lower part of the *whole* detector (all six supermodules) was put in acquisition (both scintillators and streamer tubes) in December 1992, while the *full* MACRO (lower part and "attico") construction was completed in June 1993. The data for this analysis came from the full lower part of MACRO as it was configured by the end of 1992. This will be the point of reference for what will follow regarding the MACRO detector. Since no part of the "attico" was used in this analysis[3] there will be no further reference to that.

2.3 The Scintillator Detectors

The scintillation system of the lower part of every supermodule in MACRO consists of 32 horizontal counters and 14 vertical counters. The horizontal counters cover the center and bottom layer with 16 units in each of them, while the vertical counters cover the east and west layers with 7 units in each of them. The face of the first supermodule that points to the north and the face of the sixth supermodule that points to the south are also covered with 7 vertical counters each. However, neither the north nor the south face of the MACRO detector have been in acquisition during the data-collection period relevant to this search[4]. Both the horizontal and vertical counters are parallelopided-shaped with a nominal length of 12m and rectangular cross-section of 74cm$\times$22cm. The active, highly transparent, mineral-oil based scintillator fills about 11m of the counter's length and it reaches a nominal height of 19cm and 46cm for

[2]The mechanical construction and related electronics of the lower part of the first supermodule of MACRO is described in detail in reference [70].

[3]Actually, no part of the "attico" has collected any monopole data so far.

[4]With the exception of the north face during the 1989-91 first supermodule engineering run, none of these detector faces have collected monopole data so far.

the horizontal and vertical counters respectively. This varies by a few millimeters from tank to tank and also from end to end within the same tank. The end to end variations are the result of the fact that counters are not perfectly level. The two ends of each counter house the reflectors and the photomultipliers (PMTs) that collect the scintillation light. Horizontal counters are instrumented with two PMTs in each end while vertical counters with just one PMT in each end. Since there will be frequent reference to individual scintillator counters in the upcoming chapters, let us briefly describe the nomenclature that we follow in assigning names to them. Each counter carries a four character name: the first character denotes the supermodule where it belongs (i.e., from 1 to 6); the second one corresponds to the face (we use the initial of the name of each face, i.e., C for center, B for bottom, etc.) while the last two indicate the relative position of the counter in the face. For example, 3B13 refers to the 13th counter of the bottom face of the third supermodule. Horizontal counters are numbered from 01 to 16 starting from the north-most one, while vertical counters are numbered from 01 to 07 starting from down up. Within one counter, let us assume 3B13, an additional digit (0 or 1) at the end discriminates the north (name-0) and south (name-1) end of a vertical counter or the west (3B13-0) and east (3B13-1) end of a horizontal counter.

2.3.1 The scintillator tank construction and filling

All scintillator counters are made of 0.63cm thick PVC sheets. They are divided into three chambers which are separated by highly transparent windows made of 0.32cm clear PVC. The inside walls of the counters are lined with a commercial white vinyl-FEP material. Given the indices of refraction for the FEP-liner (n_{liner}=1.33) and the scintillator mix (n_{scint}=1.4750$\pm$0.0005), total internal reflection (i.e., reflection with no loss in the light intensity) is achieved for light rays making an angle θ with the liner surface less than 25.6°. For the air/scintillator interface, total reflection is achieved at incident angles less than the critical angle (with respect to the interface)

of 47.3°. Reflections on the liner and the air[5] interfaces of the scintillator result in an effective attenuation length which tests have shown to be greater than 26m. The main central chamber ($\approx$ 11m long) of each scintillator counter is filled with mineral oil-based scintillator mix. The geometry of the MACRO counters dictates the attenuation characteristics of the liquid scintillator mix that we have developed. A high purity mineral oil is used as a solute; its attenuation length was measured by LED (light emitting diodes) spectrophotometer to be greater than 20m at the wavelength of 425nm[6] [91]. The scintillant is a mixture of pseudocumene (1,2,4-trimethylbenzene), PPO (2,5-diphenyl-oxazole) and bis-MSB (p-bis[o-methylstyryl]benzene). Pseudocumene (C_9H_{12}) is the primary fluor, emitting light at a wavelength of $\sim$290nm. PPO ($C_{15}H_{11}NO$) works as the first stage wavelength shifter to $\sim$360nm and finally the bis-MSB ($C_{24}H_{22}$) shifts the wavelength to $\sim$420nm [20], which is the sensitive wavelength region of the PMT. After studies of the performance of a test counter[7] with different proportions of the scintillator ingredients, the final MACRO scintillator mix is made of 96.4% mineral oil, 3.6% pseudocumene, 1.44g/l of PPO and 1.44mg/l of bis-MSB. The two end chambers of each horizontal counter contain two PMTs and two specially designed mirrors which increase the geometric light collection efficiency. The anode signals of the two PMTs in each end are connected in parallel and they drive a single 50Ω cable that goes to the electronics. On the other hand, the end chambers of the vertical counters contain one PMT and a simple conical mirror properly truncated to fit into the rectangular cross-section of the counter. Both horizontal and vertical counters have their end chambers filled with mineral oil, the same oil used in the scintillator mix. Figures 2.5 and 2.6 show the detailed geometry of each type of counters.

[5]Notice that the critical angle of the liner is less than the one for the air, thus making it the most relevant.

[6]Furthermore, individual mineral oil shipments to Italy were subject to laser spectrophotometry tests [63] before filling the MACRO counters; those tests yielded similar attenuation lengths.

[7]What we basically studied was the light yield of muons vs pseudocumene concentration.

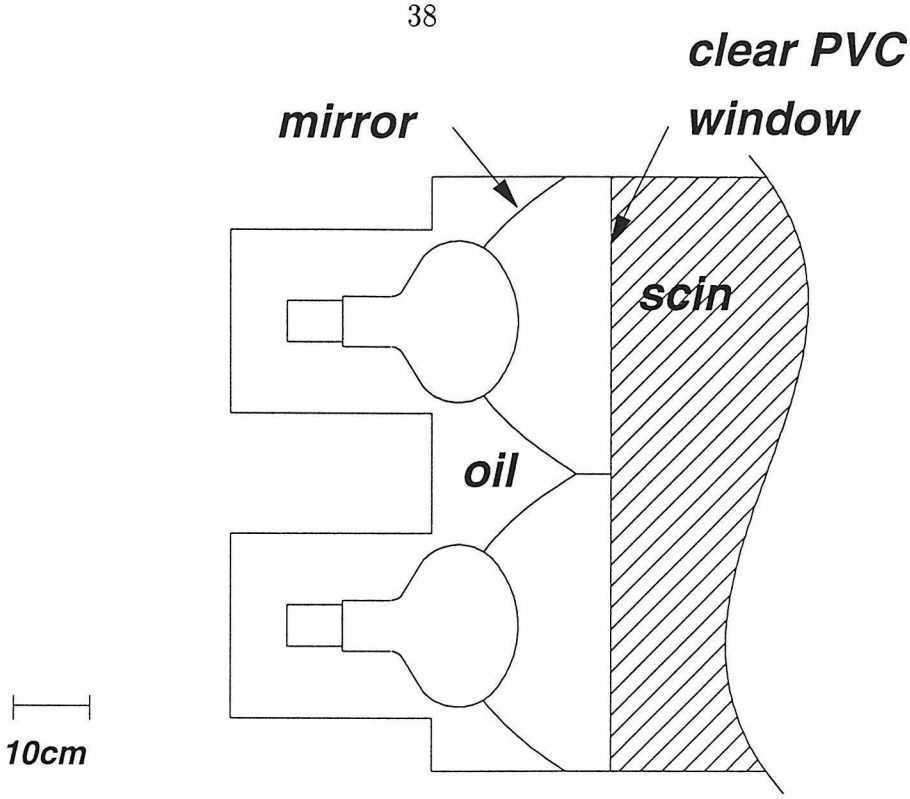

Figure 2.5: Details of an end chamber of a horizontal scintillator counter. The anode signals of the two PMTs are connected in parallel to a single cable which reaches the electronics.

2.3.2 The photomultiplier tubes

The photomultiplier tubes (PMTs) used in the lower MACRO detector are the EMI D642 20cm hemispherical tubes[8]. The manufacturer quoted quantum efficiency has a peak value of 27% at 420nm. The PMTs are operated with negative voltage at a

[8]During the first supermodule runs [54] [70] the Hamamatsu R1408 8" hemispherical PMTs were used. These HAMAMATSU PMTs were replaced by EMI ones. We chose the EMI PMTs to be used in MACRO, because of their very clear single photoelectron signal which is important for slow monopole detection. However, two rather serious problems came along with the installation of the EMI phototubes: unlike the HAMAMATSU ones, EMI PMTs in the horizontal tank ends proved to be significantly affected by the Earth's magnetic field and, in addition, they were severely subject to degradation due to sporadic discharges (often referred to as "sparking") from the PMT photocathode to the nearby conductors. These problems made necessary several retrofits of the scintillator tank ends: iron magnetic shields were used to protect each PMT, while installation of the so-called "spark-kits" brought the potential of all the conducting materials in a tank end to that of the photocathode. The installation of the "spark-kits" and the oil-filling of all tank ends reduced significantly the PMT sparking throughout the whole detector. However, mostly due to poorly installed spark-kits, sparking had been an occasional visitor of MACRO's PMTs. Sparking normally results in wide, wiggly sequence of pulses, which sometimes managed to trigger the slow monopole trigger.

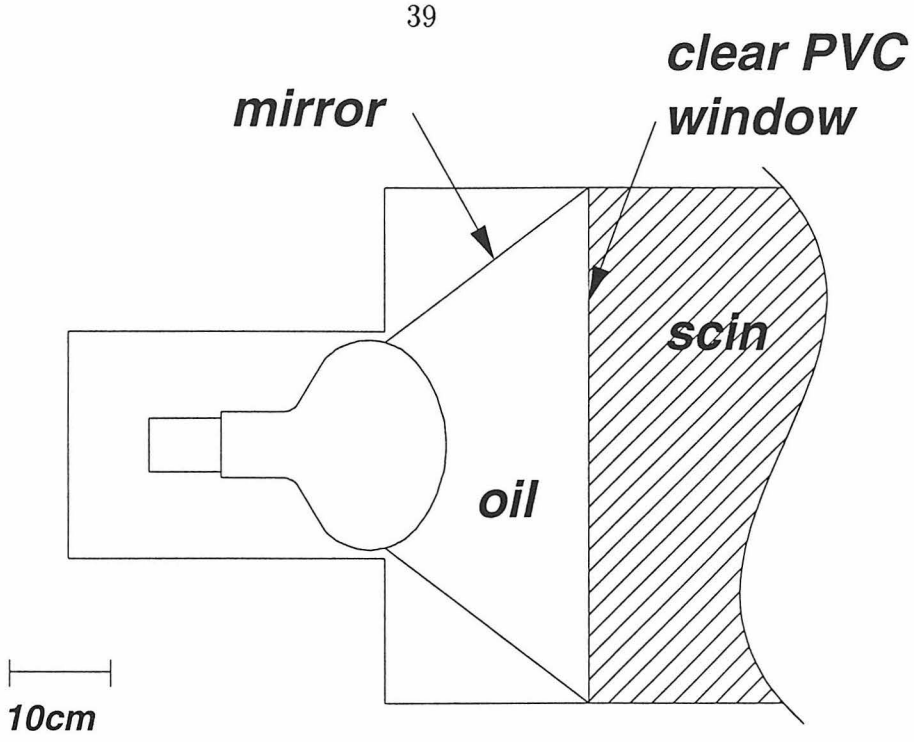

Figure 2.6: Details of an end chamber of a vertical scintillator counter.

nominal gain of 5.5×10^6. Their typical voltage setting is around –1500V and the most likely pulse height per single photoelectron (spe) is 4mV. Although a higher gain favors any slow monopole (because of their expected low light yield) search by allowing better resolution of spes, it is to the disadvantage of the muon and relativistic monopole (because of their expected high light yield) search due to PMT saturation effects. The above mentioned gain setting has been a compromise between these two. A typical spe charge spectrum for the EMI D642 PMT is shown in figure 2.7. A LeCroy 3001 multichannel analyzer (qVt) was used for this measurement [101]. A light emitting diode (LED) located at the far end of the tank was used as the light source; its light level was appropriately adjusted so that spe signals to be mainly produced. One can clearly see the pedestal (in the left-hand side) and the spe peak (in the right-hand side) standing out. The slight shoulder depicted at the right of the spe peak comes from two photoelectron pulses. By increasing the light level of the LED, multiple photoelectrons spectra can be seen. The PMT anode signals are

brought to the fanouts with 50Ω RG58 cables. We found no need to use extra signals from the dynode chain; they exhibit saturation characteristics similar to the ones of the anode, thus making no significant improvement to the dynamic range of the PMT. With the PMT signals arriving in the fanout, they are copied and made available to the various triggering and recording electronics.

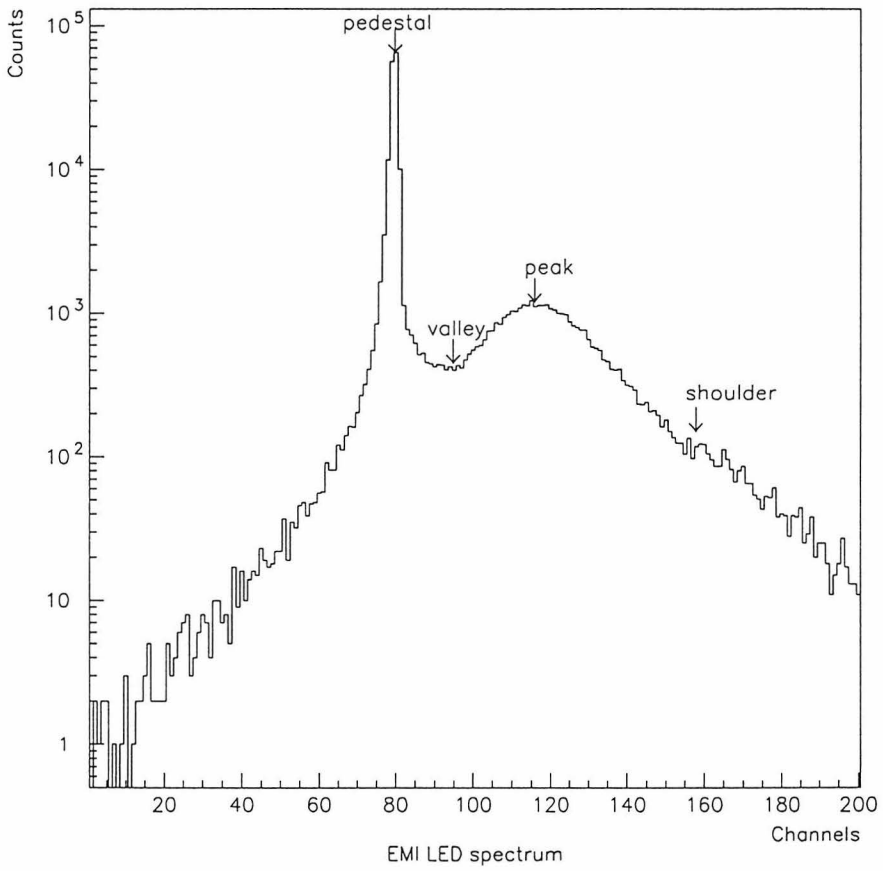

Figure 2.7: EMI PMT single photoelectron (spe) charge spectrum at 4mV gain. The spectrum was obtained using a LeCroy qVt in the q-mode. The spe peak is roughly 35 channels from the pedestal. Given the qVt's specifications of 0.25pC/channel, the observed spe peak corresponds to a charge of 8.75pC, or $5.5\times10^6 e^-$. A voltage calibration of qVt's q-mode yielded 0.11mV/channel [101] which translates the observed charge gain for spe to 4mV.

2.3.3 The calibration system

An issue of fundamental importance for a detector of the size and complexity of MACRO is its continuous monitoring. In addition, a number of diverse electronics processing the PMT signals ask for precise set up not only upon installation but also periodically. Having these in mind, two independent systems, able to generate artificial light, have been implemented throughout the whole scintillator system: light emitting diodes (LED) have been mounted on the mirror of each PMT in every counter while quartz optical fibers guide UV laser light to the longitudinal center of each counter.

The LEDs are manufactured by Hewlett-Packard and their emitted light is red. Two programmable pulse generators made by the same manufacturer (HP 8115A) constitute the heart of the pulse generation system. The pulsers are fully programmable in pulse height, pulse width, period, delay, rise time, fall time and polarity. A GPIB controller allows us to access them via CAMAC. The four analog outputs coming from the two pulsers are sent to a fanout which makes copies of the driving signals for each supermodule. The pulse distribution system for each supermodule consists of custom made LED switchboxes which distribute the signals to each LED via 30m long RG58 cables. A CAMAC interface (a two channel Jorway Model 224) allows access of the state (on/off) of individual LEDs. Being able to simulate the passage of any particle through MACRO, LEDs are used primarily for timing calibrations of both the muon and monopole electronics (see next section) and also for charge calibrations of the monopole electronics [68].

The laser calibration system is based on six nitrogen lasers, one for each of the supermodules. The output of each laser is directed through a variable attenuator and then into splitters which drive the laser pulses through optical fibers to every scintillator counter of any given supermodule. The variable attenuator is controlled via CAMAC and –like with the LED calibrations– laser calibrations run automatically via computer commands. Two monitoring PMTs view the light coming out of each laser before and after the attenuator; the ADC which is connected to each of these

PMTs provide the reference for the amount of light reaching each counter. Lasers are used primarily for calibrations of the muon electronics: variation in the laser's intensity allows us to calibrate their ADC response and also to calculate TDC corrections introduced by variations in the start of the timing circuits because of different PMT pulse heights.

2.3.4 The scintillator electronics

There are three classes of electronics attached to the scintillator system of MACRO; each one is optimized to trigger upon and record events coming from the passage of different kinds of particles through MACRO. These include –but are not limited to– relativistic cosmic ray muons, antineutrinos from stellar collapse and magnetic monopoles; we will refer to the corresponding electronics by the particle name they are primarily made to detect. Different electronics within the same class work in complementary way, while there is overlap between electronics of different classes.

The energy reconstruction processor (ERP) system is the primary muon trigger and ADC/TDC readout system for the MACRO scintillator counters. The trigger is based on the *amount of energy* deposited within a *single* scintillator counter. In order for the energy to be reconstructed, FADCs are used to digitize the integrated signals coming from the two ends of a scintillator counter. These digitizations are used as addresses into an 8k×8k RAM look-up table (LUT) which has pre-loaded the energies corresponding to all possible signal pairs. The threshold for the ERP muon trigger is ∼16MeV. The CSPAM electronics provide another trigger for fast particles going through MACRO. Unlike the ERP which is a single tank trigger, CSPAM requires the coincidence within 1μs of PMT signals coming from two different detector faces and exceeding a preset *amplitude threshold.* CSPAM trigger logic works with "supercounters": the scintillator counters are grouped in sets of eight[9] and thus a "supercounter" results. The two ends of a supercounter are formed by the analog sum of the corresponding ends of the eight individual tanks that make up

[9]Actually, for the vertical faces, supercounters group together seven scintillator counters. Incidentally, custom-made linear fanins are used for the multiplexing purposes.

the supercounter. After the rearrangement of the PMT signals into the scheme we have just described, commercial latching discriminators are used in order to check which of the signals coming from the supercounters exceed a 200mV threshold. The output of the discriminators are fed into a custom-made plane-logic module that checks for coincidence of signals coming from the two ends of a supercounter within a ~100ns coincidence window[10]. The plane-logic modules OR together the coincidence conditions of supercounters that belong to the same detector face and start a 1μs gate. If another such coincidence coming from another face is found within this gate, a trigger is generated. The CSPAM trigger forms face coincidences within a single supermodule or within any two adjacent supermodules of MACRO; because of the peculiar way in which the cross-supermodule triggering works for CSPAM, a trigger coming from a given supermodule will also generate a trigger in its adjacent one[11]. The CSPAM system offers only a CAMAC-readable hit register which records the supercounters that provided the coincidence; however, upon formation of the trigger (which lags only a few nanoseconds from the activity in the tanks) the waveform digitizers (described below) are stopped (in a common stop mode) and read. For the vast majority of the events selected by CSPAM, the ERP system is also expected to trigger[12], thus providing an additional ADC/TDC information.

The gravitational collapse (GC) electronics are designed to detect low energy (from a few MeV to a few tens of MeV) antineutrinos emitted by collapsing stars. Two independent systems looking for this type of events are employed. The PHRASE system [75] uses analog techniques to overcome the light attenuation within a scintillator counter; this attenuation is reflected in the PMT signals coming from its two ends. By comparing the adjusted PMT signals coming from the two ends of each counter, the energy of an event is thus reconstructed. The ERP system –as we have seen–

[10]The ~100ns coincidence window accounts roughly for the time it takes light to propagate from one end of a counter to the other.

[11]This is primarily a dead time issue, while some minor implications to the slow monopole analysis will be discussed in chapter 6.

[12]As we pointed out earlier, ERP is an energy threshold based trigger while CSPAM is an amplitude threshold based trigger. Because of this difference, muons triggering one system *at the threshold* might not trigger the other. Also, because of the channel multiplexing, CSPAM is less sensitive to muons corner-clipping single scintillator counters.

performs the same energy measurement, but using digital techniques. By setting a lower energy threshold (compared to the one for muons) and providing an additional event buffer, the same hardware (ERP) that is used for muon physics is also used to trigger and record GC events. The primary energy threshold of the GC electronics is ~7MeV.

Monopole Electronics

As we have seen earlier, magnetic monopoles are expected to traverse MACRO traveling at velocities of order $\sim 10^{-3}c$; however, velocities as low as the earth's escape velocity $v \sim 4 \times 10^{-5}c$ and as high as c should not be excluded. This is indeed a significantly wide range of velocities; assuming a pathlength of 5m (see fig. E.2), these velocities translate to time of flights ranging from 1μs to several hundreds of microseconds for a hypothetical monopole going through the center and bottom layers of MACRO. Nevertheless, time of flight diversity could have been easily overcome if monopoles were depositing enough energy in the scintillator counters to be straightforwardly distinguishable from the exponentially falling radioactivity spectrum. Unfortunately, this is true only for the upper end of the monopole's expected velocity range (see figure 1.4). As we have seen in chapter 1, the great diversity in the light yield expected for a monopole requires any terrestrial search to be efficient over more than four orders of magnitude of expected monopole light yield. More than that, there is an additional interest for searches for other exotic particles (besides monopoles) which are expected to travel at typical galactic velocities and have similar to or even less than the monopole's ionization yields (these include nuclearites whose ionization is strongly dependent on their mass [76] and other fractionally charged supersymmetric particles). With these in mind, a custom made circuit optimized to detect *wide pulses* of *low height* or *trains of single photoelectron pulses* lasting several microseconds was built at the California Institute of Technology. This is the so-called slow monopole trigger (SMT).

This trigger is based on the time of flight through a scintillator layer (nominally 19cm see fig. E.2). It consists of two parts: the first one is an analog circuit which

translates the input PMT pulse coming out from the fanouts to TTL output pulse whose duration is nominally the time during which the input pulse is greater than its half maximum. Because of that, this circuit is called Time-Over-Half-Maximum or TOHM circuit. There is a minimum threshold that the input PMT pulse should exceed in order for an output TTL pulse to be generated by the TOHM. This threshold is controlled with a front-face trimpot and it is currently adjusted to 2mV. The TTL output of the TOHM is sent to the second part of the trigger circuit which is fully digital. This circuit runs a scaler up at a fixed frequency (66MHz) when its input (i.e., the TOHM output) is high and runs it down at a lower frequency when the input is low. The trigger is formed when the scaler reaches a predetermined number of counts. Apparently, this second part of the SMT is nothing but an integrator which however "leaks out" when it receives no input; this is why it is called Leaky Integrator or LI circuit. Both the run-down frequency and the scaler's trigger threshold for the LI's are CAMAC programmable. During the six-month running, we set the trigger threshold to 10 counts (9 counts for the vertical tanks) which, given the LI's up-counting frequency, they correspond to a minimum pulse duration threshold of $\sim 160ns$. This defines the upper velocity limit to which the monopole circuit is sensitive; assuming a nominal pathlength of $19cm$ within a scintillator tank, this is $\beta \sim 4 \times 10^{-3}$. Each scintillator tank end is serviced by one TOHM and one LI channel. In order to trigger the data acquisition (and the rest of the electronics), the coincidence within $20\mu s$[13] of the LI output coming from the two ends of a scintillator counter is required[14].

The SMT by itself offers only a hit register that records the scintillator counters that satisfied the trigger conditions. This is read via CAMAC upon every SMT trigger. The PMT pulse shape information for every SMT trigger is recorded by commercially available waveform digitizers (WFD). These are the LeCroy 2261 CCD-based digitizers. This model provides 11-bit analog-to-digital conversion and offers clock rates up to 50MHz. Each unit provides four inputs with a memory of 320

[13]The end-to-end coincidence window is determined by the maximum time a slow monopole is expected to spend inside a scintillator tank.

[14]Let us point out that apparently the SMT is a single counter trigger.

samples (time buckets) for each one of them. We chose a clock rate of 40MHz for them[15]. The least count is 1mV and its range goes up to 2V. Due to the limited number of waveform digitizer units we had available, a multiplexing of the PMT signals was inevitable in order to instrument the whole detector. The multiplexing is based on a 16:1 scheme for the horizontal counters and a 7:1 scheme for the vertical counters. This scheme requires a total of 48 waveform channels for the whole detector. The multiplexed PMT signals are provided by the CSPAM system. As we have seen earlier, CSPAM forms the supercounter signals using linear fanins. A copy of each of these signals is used as an input to the waveform digitizers. Although the purpose of the WFD is primarily to provide pulse height information for the monopole system, both of the muon triggers can stop and read them. A custom made latching scaler (LS) module is used for managing the stop of the waveform channels and also for recording the time of flight for SMT triggers involving more than one detector face. This module utilizes a digital counter which is clocked by a 10MHz clock[16]. Upon the occurrence of an SMT face trigger, the corresponding WFD channel is stopped and the digital counter starts counting up. If a second SMT face trigger occurs within $\sim$1.7ms, a bit within the LS is set in order to indicate that a coincidence was found. At the same time, all the WFD channels are stopped and then read. The latching scaler latches four time words (corresponding to the four faces of a supermodule) but also trigger and face hit words providing information regarding which trigger stopped the WFD or, for the case of the SMT, which face was involved in the WFD stop. Each LS module services two supermodules. However, for coincidence formation (not for precise timing though) purposes, SMT signals from the adjacent supermodule(s) are also used in order to form two-face coincidences between *any* two-supermodule combination. In addition to the three LS modules needed to cover the whole detector, an extra module is used for timing of face hits coming from combination of supermodules not covered by the other three LS modules. Special attention was paid to guarantee the priority of the monopole triggers on stopping and reading the WFDs[17].

[15]Given the number of samples in memory, the digitizing window spans 8μs.

[16]The LS clock is actually synchronous with the 40MHz WFD clock.

[17]The WFD stop and readout configuration during the six-month run was not allowing ERP

In addition to the SMT circuit, a conventional time of flight-based trigger for the detection of magnetic monopoles of intermediate velocities is implemented in the MACRO detector. This is the so-called fast monopole trigger (FMT) and it uses the *same* hardware as the CSPAM muon trigger we have described earlier. The extra feature of the FMT is that it takes the output of the plane-logic boards and starts a $\sim 10\mu$s gate within which it waits for a two face coincidence. The FMT trigger is vetoed in hardware by the CSPAM trigger; thus FMT selects particles with time of flights within MACRO from 1 to 10μs, which for a nominal pathlength of 5m correspond to a β of 1.5×10^{-2} down to 1.5×10^{-3}. Let us point out that in this velocity regime, the monopole light yield is expected to be several times the light yield of the minimum ionizing muon; given that muons traversing 19cm of scintillator yield on the average PMT pulses of $\sim$1V (as recorded by the WFD), the pulse height discrimination of the CSPAM/FMT system at 200mV should not reject monopoles even if they go through only a few centimeters within a scintillator layer. The PMT pulse shape information for the FMT is provided by the WFD which the FMT system stops (in a common stop mode) and reads.

2.4 The Streamer Tube Detectors

The streamer tube system of the lower part of every supermodule in MACRO consists of 10 horizontal and 12 vertical (in the east and west faces) planes of tubes. The north and south faces of MACRO are also instrumented with 6 vertical planes of streamer tubes each. The area covered by each horizontal plane is approximately

(muon) triggers to stop and read the WFDs if they were accompanied by an SMT trigger. This, however, was not the case with the CSPAM triggers which could stop the WFDs in a common stop mode upon their occurrence. The assumption here is that even if this kind of event is accompanied by a monopole (SMT) trigger, it is caused by through-going muons. Let us point out that a fast particle which may trigger CSPAM is expected to be produced by a monopole catalyzing proton decay. The hardware configuration we have just described vanishes almost completely any sensitivity to proton-decay-catalyzing monopoles. Future running of MACRO will be able to detect such monopoles. This will be thanks to the new custom made WFD system which is currently being installed in MACRO. The new WFDs will not only have ample memory (64kB) but they will also be stopped 1ms after the first trigger (no matter which trigger that is), thus allowing the crossing of both the proton decay product and the monopole to be properly recorded.

12m×12m while for the vertical planes the covered area is approximately 12m×5m. Streamer tubes have modular structure; they are organized in groups of eight in a 3.2cm×25cm×12m chamber. They operate in the limited streamer tube mode [56] and take advantage of the resistive cathode technique to allow two-dimensional readout. The basic unit of the streamer tube system is an open cell made of 1.5mm thick PVC. A 100μm diameter anode wire (silvered Be-Cu) runs along the center of the cell, while the three sides of the square cross section of the cell are covered with a low-resistivity ($\leq$1kΩ per square) graphite coating. The fourth side of the cell is left electrodeless; it is only closed with a piece of insulating PVC [17]. In the horizontal streamer tube planes, two-dimensional readout is achieved with external pick-up strips placed under the insulated side of the wires at 26.5° with respect to them. The pick-up strips are made of aluminum sheet which is attached to a PVC foil. The vertical streamer tube planes are not equipped with pick-up strips. Streamer tubes may be operated with various gas mixtures. For MACRO's streamer tubes we have chosen a He-nPentane (in 73%-27% proportions respectively) mix which allows the exploitation of the Drell effect [40] for slow monopole detection.

MACRO's streamer tube system is equipped with digital and analog front end electronics that allow us to localize the streamer tube hits in space and time while providing us with an additional streamer charge and duration measurement. Digital electronics include hit registers that record the *individual* wires that fired within 10μs and within 550μs. The shift registers recording streamer tube hits within these two time windows are referred to as the "fast chain" and "slow chain" respectively[18]. On the other hand, discriminated analog signals coming from the wires are sent to ADC and TDC modules (QTP [9]) which record the streamer signal arrival time, duration and charge[19]. Both digital and analog electronics are accessible via CAMAC upon the occurrence of a trigger. There are two families of streamer tube triggers, both of which are utilizing as inputs the OR of the discriminated wire signals coming from a

[18]Digital readout for the strips [8] is similar to the one for the wires. It offers slightly worse granularity and the fast and slow chains have slightly wider time windows.

[19]At present, QTP modules serve only the wires of horizontal streamer tube planes and they are multiplexed in a 32:1 scheme.

streamer tube plane (of a supermodule). First it is the fast particle trigger [13] which checks for hit patterns among the 10 horizontal and 12 vertical streamer tube planes. The preselected triggering conditions are coded in EPROMs which sample the input signals at a 3.3MHz frequency and check for the desired hit coincidences. For slow particle triggering purposes the above approach would have lead to disastrous counting rates given the background rate of 50-100 Hz/m^2 induced by the local radioactivity. That is why a more sophisticated slow particle trigger was needed. The slow particle trigger for MACRO's streamer tube is based on the expectation the streamer tube hits in consecutive planes to be aligned in time, i.e., to be consistent with the passage of a particle of a constant velocity [12]. Since on processing a streamer tube hit pattern there is no *a priori* knowledge of what the β of a hypothetical slow particle might have produced them, custom made electronics search for alignment of the hits assuming various[20] β. The time history of each streamer tube plane is saved in a shift register which is clocked at 1MHz (thus offering a 1μs time resolution) and offers a memory of 480 buckets (i.e., it can search for time alignments within 480μs back in time). For a given β, predefined locations of hits are expected to be found in the time history of a streamer tube plane; based on that a slow particle trigger is formed.

2.5 The Track-etch Detectors

When charged particles pass through track-etch detectors, a path of intense local damage is created along the particle's trajectory. Although this damage is on the atomic scale (not exceeding a few hundreds of $\AA$), it can be made visible in an ordinary optical microscope when the detector is treated with a suitable chemical etchant; during the etching process, the material along the particle's path is removed at a rate v_T which is greater than the rate v_B at which the bulk (undamaged) material is removed. The simultaneous action of these two processes results in the simple track geometry depicted in figure 2.10 which allows the identification of the passage of a particle by simply detecting the resulted etch-pits. There is indeed a great diversity

[20]There are 160 different β-slices.

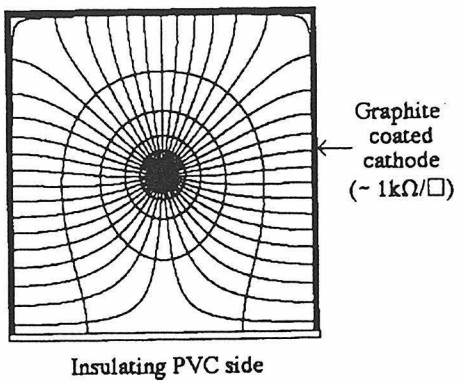

Figure 2.8: Configuration of the electric field lines for an electrodeless plastic streamer tube. During operation, the positive ions produced in the gas by the streamer procedure drift towards the insulated side reshaping the field lines (from the initially 90° rotationally-symmetric configuration) until all of them end only on the graphite-covered sides. The electrodeless streamer tubes simplifies the construction procedure without any significant loss in the performance of the tube.

of solids that exhibit this track-registering property: crystals, ordinary glass and organic polymers are the most commonly used. Although we are far from having a complete understanding of what exactly is the nature of the damage, we believe it has something to do with the continuous disorder of the crystal's lattice structure or the breaking of the long polymer molecule chains which the passage of charged particles results in. Although the two etching rates v_B and v_T depend in general on the material and the etching conditions, the *reduced etching ratio* $p=v_T/v_B$ –which traditionally has been the signal measured out of a track-etch detector– seems to obey simple relations with the so-called *restricted energy loss* of the impinging particles. According to the restricted energy loss model, the energy loss that is relevant to track formation is the portion of the total energy loss that produces delta rays of less than some specified energy E_0, characteristic of the recording material. Accounting for this cut, Bethe-Bloch's formula is then modified as follows

$$\left(\frac{dE}{dx}\right)_{E<E_0} = 4\pi N_a r_e^2 m_e c^2 (\frac{z}{\beta})^2 \frac{Z}{A}\left[ln\left(\frac{\sqrt{2m_e c^2\beta^2\gamma^2 E_0}}{I}\right) - \frac{\beta^2}{2} - \frac{\delta}{2}\right], \qquad (2.1)$$

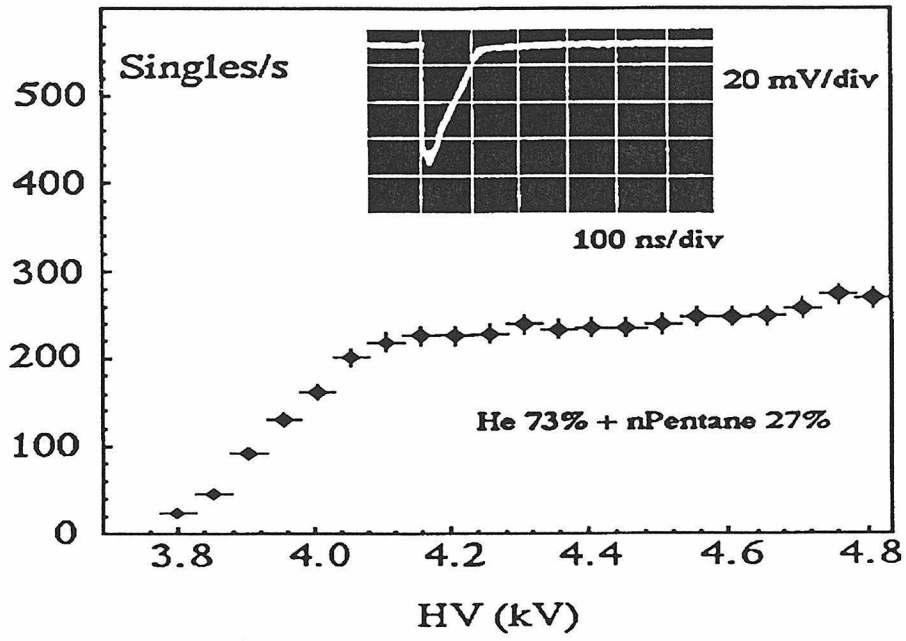

Figure 2.9: Singles plateau as a function of high voltage and typical wire pulses (on 50Ω termination) for a test streamer tube. The observed initial rise comes from the gradual transition from the proportional to the streamer operation. The streamer mode is almost in saturation but not fully. Tests with relativistic ion beams [18] have shown that multi-streamers produced by heavily ionizing particles (dE/dx>I_{min}) result in a logarithmic rise of the streamer charge as a function of the dE/dx.

where z/β refers to the incoming particle, Z/A to the track-etch material, $N_a r_e^2 m_e c^2 = 0.307 MeV cm^2 g^{-1}$ and δ is the density correction, which accounts for relativistic corrections due to charge shielding and can be calculated from various empirical formulas [65].

The above portion of the total energy loss represents low energy delta rays which deposit their energy mostly within a short distance (a few hundred $\AA$, the size of the damaged region in a track-etch detector) from the particle's path [60]. As faster ions result in a larger fraction of delta rays that have high energy, the restricted energy loss $dE/dx_{E<E_0}$ given by 2.1 becomes a smaller fraction of the total energy loss at high ion velocities.

Like all the other detecting elements in MACRO, the track-etch detector has a modular structure that matches MACRO's mechanical modularity. Each of the six lower supermodules, just above the fifth (counting from the bottom) layer of

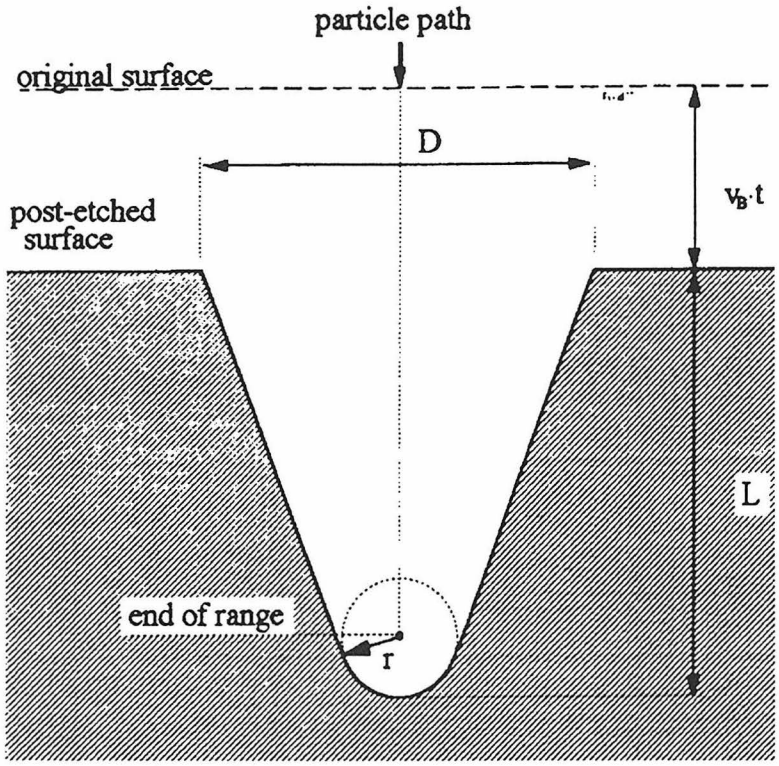

Figure 2.10: Sketch of the etching procedure of a solid state nuclear track detector. The fact that v_T is greater than v_B results in the conical shaped etch-pit. For etchings *beyond* the end of range of the impinging particle, the material is removed at the bulk rate, so a spherical "extension" of the original cone results.

streamer tubes, is equipped with 48 "trains" each consisting of 47 "wagons" (stacks) of nuclear track detectors. Similar mechanical structures house track-etch modules in the east and north face. The total area (horizontal and vertical) covered by track-etch detectors is $\approx 1300 m^2$. The basic unit of MACRO's track-etch detector is the "wagon" we have just mentioned. Each "wagon" is 24.5cm×24.5cm and has a sandwich-like structure made of three layers of 1.4mm thick CR39, three layers of 0.25mm thick Lexan and a 1mm thick aluminum absorber arranged as in figure 2.11. The purpose of MACRO's track-etch detector is to confirm the passage of a magnetic monopole when an electronic trigger is provided by the active detector elements [71].

Of the two nuclear track detectors used in MACRO, Lexan's high detection threshold (REL $\approx 3 GeVcm^2/g$) makes it sensitive only to relatively fast moving monopoles ($\beta > 10^{-1}$). The second nuclear track detector (CR39) was known to have unrivaled

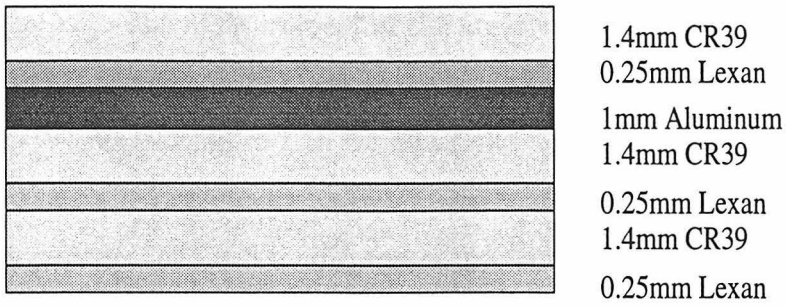

Figure 2.11: The CR39 sandwich (widths not in scale): the three layers of Lexan provide sensitivity to fast monopoles while CR39 is intent for slow monopole detection. The aluminum absorber in between the track-etch detectors is in order to prevent heavy ions from being recorded by all the track-etch layers.

sensitivity and resolution among track-recording solids [28] and was employed in order to accommodate the extremely wide velocity and energy loss ranges expected for a magnetic monopole. Our major concern has been to optimize the fabrication and establish the sensitivity of the CR39 as a monopole detector.

The CR39 used in MACRO is produced by the Intercast company in Parma, Italy. There are two types of CR39 which have been developed for MACRO: the so-called EN3 and the L6. The two types, although made of the same monomer, differ in the catalyzers and additives used and also in the maximum temperature reached during their curing cycle [71]. The L6 has shown lower detection threshold and better post-etched surface quality; that is why it was selected as the type to use in MACRO[21]. Both types of CR39 were calibrated with relativistic heavy ions: (i) with O^{8+} oxygen nuclei of 16 GeV/nucleon at Brookhaven (1988), (ii) with Ne^{10+} neon nuclei of 585 MeV/nucleon at Berkeley (1990) [71], (iii) with Si^{14+} silicon nuclei of 14.5 GeV/nucleon at Brookhaven (1990), (iv) with S^{16+} sulphur nuclei of 200 GeV/nucleon at CERN (1990) and (v) with Au^{79+} gold nuclei of 11.3 GeV/nucleon at Brookhaven (1992) [29]. During these exposures, stacks of few 7cm×13cm sheets of CR39 were exposed to the above mentioned primary ions and their fragments. The CR39 sheets were then etched in 6N NaOH solution at 70° temperature. The areas of the resulted etch-pits (see figure 2.10) were measured by an ELBEK automated image

[21]With the exception of the middle layer of the first supermodule which was equipped with the EN3 type of CR39, we have used the L6 type for the rest of the detector.

analyzer system [85]. The measurement of the areas combined with the measurement of the bulk etching rate v_B yields through trivial geometric equations [44] the reduced etching ratio $p=v_T/v_B$. In figure 2.15 we plot (with filled circles) the reduced etching ratio p versus the restricted energy loss (REL) values obtained from equation 2.1 for all the primary incident ions and their fragments to which CR39 was exposed[22]. As we can see from this plot, L6 remains sensitive ($p\geq 1$) above $\sim$26MeVcm^2/g (corresponding to $z/\beta \sim 5$)[23]. The above calibration procedures study the response of the CR39 to *relativistic* particles; such particles lose energy primarily via inelastic collisions with the target's electrons thus leading mainly to *ionization* and *excitation* of the target atoms. This so-called *electronic stopping power* S_e is indeed the primarily mechanism of energy loss for particles moving with velocities $v \gg 10^{-2}$ and the restricted energy loss model seems to describe fairly well the response of the CR39 detector to such particles. This picture of energy loss mechanism seizes to be the dominant one at particle velocities $v \ll 10^{-2}$ where elastic collisions of the incident particle with the target nuclei start becoming more and more important. In this case, the lost energy goes to the recoiling target nucleus; that is why this energy loss process carries the name of *nuclear stopping power* S_n. The assumption that the reduced etching ratio p depends on the rate of energy deposited locally in the CR39 and *not* on the exact process responsible for the loss (i.e., electronic or nuclear stopping) led P. B. Price [95] to the conclusion that a "good" CR39 detector with low threshold would be able to detect monopoles with velocities down to $\sim 3\times 10^{-5}$c. Price showed how screened Coulomb collisions of monopole composites (monopole+proton or monopole+^{27}Al) and diamagnetic repulsion of bare monopoles when interacting with the atoms in the plastic may lead to energy loss rates big enough to make monopoles able to be seen in CR39 even at that velocity regime (look at the left half of the plot in figure 2.12). However, it was again P.B. Price and D. P. Snowden-Ifft [104] eight years later who observed that CR39's response as measured with relativistic ions was not in agreement with the one obtained when slow ($\beta < 10^{-2}$) ions were used. More than that, Price

[22]For CR39 Z/A = 0.533, ρ=1.31gr/cm^3, E_0=200eV and I (the mean ionization potential) = 70eV

[23]Similar plot for EN3 reveals that its sensitivity threshold is $\sim$53MeVcm^2/g (corresponding to $z/\beta \sim 7.5$).

and Snowden-Ifft observed that the nuclear stopping power is only 20% as effective as the electronic stopping power in etchable track formation. Their results, although obtained using a *different type* of CR39 (manufactured by American Acrylics), put forward a reasonable doubt for all CR39-based monopole and other exotic particle searches [84] [86] which relied on relativistic ion-only calibrations to establish their sensitivity [39]. MACRO has undertaken the exercise of studying the response of our custom made CR39 to slow moving ions, i.e., to particles traveling at velocities expected for monopoles, losing energy at rates and with mechanisms comparable with those of monopoles.

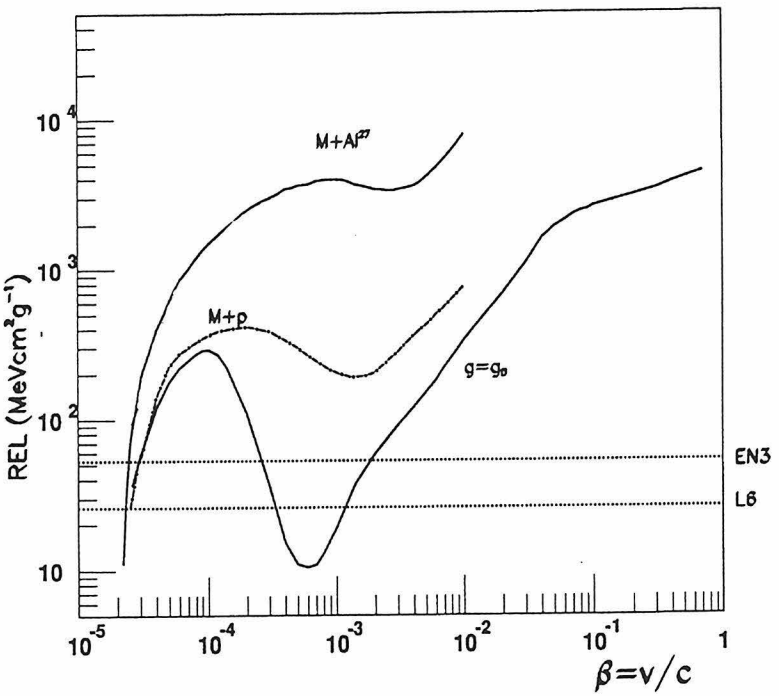

Figure 2.12: Restricted energy loss (REL) for monopoles (and other monopole composites) in CR39. For monopoles faster than $10^{-1}c$ the curve is obtained from Ahlen's calculations of REL in plastic detectors. In this velocity regime, REL corresponds to the part of the $(dE/dx)_{electronic}$ that results to delta rays with $E < E_0 = 200eV$ in the case of CR39. For $\beta < 10^{-2}$, REL=$(dE/dx)_{total} = (dE/dx)_{electronic} + (dE/dx)_{nuclear}$ with $(dE/dx)_{electronic}$ calculated by Ahlen and Kinoshita and $(dE/dx)_{nuclear}$ derived by Price after taking into account the screened Coulomb collision and diamagnetic repulsion of atoms in CR39.

The calibration with slow ions ($3.9\times10^{-3} < \beta < 2.07\times10^{-2}$) included exposures

to 100-400 keV beryllium ions, 200-400keV silicon ions, 50-200 keV hydrogen and deuterons and 6-10 MeV helium ions. The etching was performed in 6N NaOH solutions at 40°C, at which the bulk etching rate was measured to be 0.1μm/hr. Because of the short ranges of the particles studied (typically less than 1μm), a Scanning Electron Microscope (SEM) was used to determine the quantities related to the track geometry (fig. 2.10). In order to perform the measurement on the SEM, replicas of the exposed pieces of CR39 were prepared according to [44] with some changes. Although measurements of both the track diameter (D) and length (L) are possible with the SEM, we relied on the length measurement for calculating the reduced etch rate p. The intrinsic to the replica/SEM method relative error on the length measurement is significantly less than the one for the diameter one. In addition, the error on p scales as p^2-1 in the case of a diameter measurement as opposed to p-1 for the case of a length measurement[24].

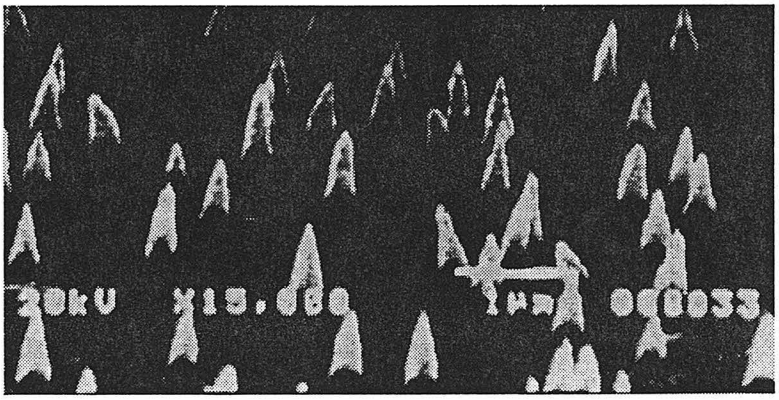

Figure 2.13: A piece of CR39 which was exposed to 400keV Be ions and was etched for 2 hours in a 6N NaOH solution at 40°C is here viewed in a SEM. The replica is observed at a 60° angle with respect to the normal to the surface and the etched cones are of the order of 0.5μm.

For an estimate of the amount of energy loss rate for the incoming slow ions, the formula given by 2.1 is clearly insufficient since it is valid for ion velocities much greater than 10^{-2}c. Moreover, in the velocity regime we are interested in, a separate estimate of the nuclear stopping power S_n is needed if we really want to investigate

[24]Both of these results follow trivially from the analytic expressions of p as a function of L or D. As we mentioned earlier, the analytical formulas for p are obtained from straightforward geometric arguments based on the track geometry shown in figure 2.10. For a derivation of them see [44].

Price and Snowden-Ifft's observation. We have used the TRIM computer code for estimating the electronic and nuclear energy loss rates for our ion/target configurations. TRIM is the work of J.F. Ziegler, J. P. Biersack and U. Littmark [109] and it provides reasonably accurate predictions (better than 10%) for the ranges and stopping powers (electronic and nuclear) of ions in solids. In figure 2.14 we see an example of a TRIM calculation for the electronic and nuclear stopping powers of beryllium and silicon ions in CR39.

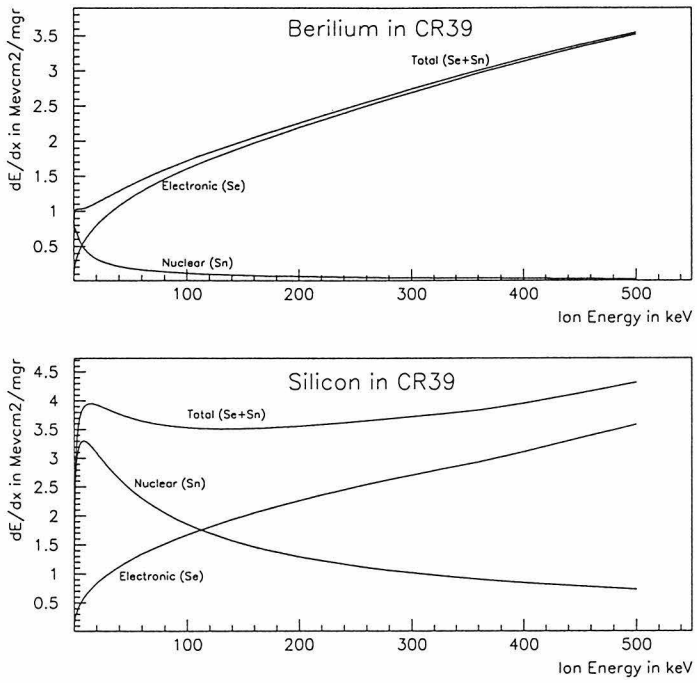

Figure 2.14: The instantaneous energy loss rates as predicted by TRIM for beryllium and silicon ions in CR39 as a function of the kinetic energy of the whole ion. One may appreciate the different contributions of the electronic and nuclear processes to the total energy loss rate for each of the ions.

With the stopping powers provided by TRIM, we plot in figure 2.15 the signal p versus the *total energy loss* for all the slow ion/energy combinations to which CR39 was exposed. As we can see, within the errors of the measurement, the slow ion data fall on the calibration curve obtained through exposures to relativistic ions pretty well. Should the phenomenon observed in the CR39 used by Price and Snowden-Ifft be also

present in MACRO's CR39, the calibration points for ions like the beryllium, protons or deuterons would be suggesting a response curve *other than* the one obtained with relativistic ions while for the case of silicon ions, a correction factor to the contribution of the nuclear energy loss to the total energy loss would have had to be introduced in order for the corresponding calibration points to fall onto the response curve[25].

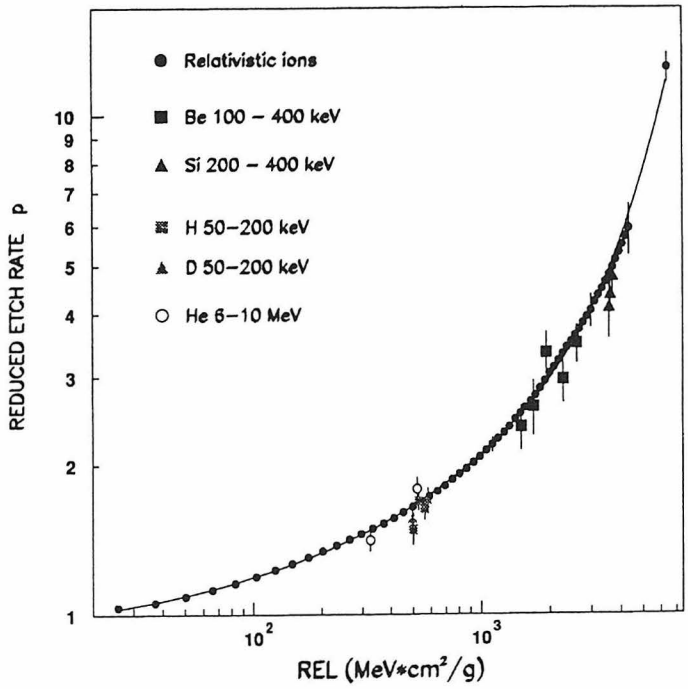

Figure 2.15: Calibration curve of the CR39 (L6 type) track detector used in MACRO. The calibration points were obtained through exposures to relativistic and slow ions. A single response curve describes the experimental data fairly well, while no need to scale down the contribution of the nuclear stopping power of slow ions is needed (see text for discussion). The etching in all cases was performed in a 6N NaOH solution at 40°C.

[25]We make this distinction between the silicon and the rest of the ions because if there were any nuclear energy loss inefficiency effect, it would have become apparent primarily in the silicon data; this is because the nuclear loss for the silicon ions is comparable to the electronic one while for the rest of the ions it is rather negligible (see figure 2.14).

2.6 The Data Acquisition and Data Organization System

The data acquisition system of the MACRO detector reflects the modular structure of the apparatus. It is based on a network of three microVAXII microcomputers[26] connected via Ethernet/DECNET and running VAXELN. Each microVAX (μVAX) services two supermodules. MicroVAXes are referred to by the numbers one through three. MicroVAX 1 handles the acquisition in SM 1 and 2, microVAX 2 the acquisition in SM 3 and 4 and finally microVAX 3 the acquisition in SM 5 and 6. This modular organization allows us to keep parts of the detector out of acquisition in order to debug or calibrate them while keeping the rest of it running. Both the scintillator and streamer tube systems collect data simultaneously through two CAMAC parallel branches. A central VAX 4000-500 running VAX/VMS is used as the file and network server. In addition to performing the data logging on disk, the main VAX runs the user interface of the acquisition system. The data taking is organized in runs whose duration is determined by the size of the output data file. When output data files reach approximately 75Mbytes in size, an end-of-run directive is issued by the central VAX and the output data file is closed. Then, a new run automatically starts. The data files are eventually transferred to the central LNGS VAX cluster (VAX 6000-510 running VAX/VMS) over the optical fiber local network, where they are copied to ~1Gbyte exabyte tapes. Copies of the exabyte tapes are then distributed to the members of the collaboration. Given the limit in the size of a data file, typical runs collecting data from the whole (lower) MACRO last approximately eight hours. The dead time of the acquisition is typically at the 1% level.

2.7 Physics Capabilities of the MACRO Detector

In the previous sections we have described the MACRO detector in detail. In summarizing, let us state that both the detector's sensitive elements and the triggering and

[26]There are two more microVAX that serve the PHRASE acquisition system.

recording electronics have been optimized to perform sensitive and redundant analyses in many fields of non-accelerator high energy physics and astrophysics. Although built primarily for magnetic monopole searches, its large scintillator volume (0.6ktons) and custom-made electronics make it sensitive to gravitationally collapsing stars in our galaxy. Continuous real-time monitoring of the incoming data make MACRO a large stellar collapse neutrino observatory [75]. Taking advantage of its large acceptance and excellent tracking provided by the streamer tube system, MACRO may search for astrophysical sources with excess flux of energetic neutral particles. By performing tracking of single muons underground, MACRO may point to their origin in the sky, thus looking for spatial or temporal anisotropies in their flux [69] [73] [74]. By means of the fine timing resolution of the scintillator muon electronics, MACRO may identify upward going muons resulting from neutrino interactions in the rock underneath the detector. Upward going muon data may be used to set limits in the local dark matter [15] [35], investigate the allowed Δm^2–$\sin^2 2\theta$ parameter space for a possible neutrino oscillation scenario [79] or probe astrophysical objects if we assume that the neutrinos are of that origin. MACRO's large area allows it to record multiple muon events separated by distances up to 77m. The rates of muon bundles of different multiplicities and the flux of muon pairs as a function of their lateral separation allows us to study the chemical composition and the hadronic interactions of the primary cosmic rays incident in the Earth's atmosphere at an energy range (E_0 >100TeV) not easily accessible by direct measurements [72] [78].

The scintillator system of the lower part of the MACRO detector is used in this thesis to make a contribution to MACRO's main physics objective: the search for slow ($10^{-4}c - 10^{-3}c$) magnetic monopoles. This search utilizes primarily the scintillator slow monopole trigger and the LeCroy waveform digitizer system we have already described.

Chapter 3

MACRO's Six-Month Run

In the previous chapter we presented in detail both the hardware and the related electronics of the MACRO detector. In the configuration there described, the MACRO detector was left for a period of roughly six months in order to collect data for physics analyses purposes. This was the *first uninterrupted run of the full lower MACRO detector* and gave the data for the monopole analysis described herein. This run, from now on, will be referred to as the *six-month run.*

3.1 Data Set

For the purpose of this analysis, we have analyzed runs starting with run 5531 which took place on the 13th of December 1992. Regarding the end of the six-month running period, run 6329, which took place on the 13th of June 1993, was the last run that accumulated scintillator data coming from all three microvaxes (full detector). All the MACRO data runs following run 6329 have scintillator data coming from *only part* of the detector. This is because at the end of the six-month run period we started decommissioning parts of the detector in order to reconfigure it in its final version (i.e., to include the "attico"). In an effort to search for a signature of a rare event in every piece of data available, we have extended our analysis to data collected beyond the official ending of the six-month run until run 6347 which took place on the 18th of June 1993. There were 1052 runs in total. Out of these 1052 data runs, 286 were *calibration* dedicated runs, i.e., runs during which part or all of the detector was being calibrated. As we have seen in chapter 2, during the six-month run the calibrations consisted of utilizing artificial light generated by LEDs and UV LASERs in order to evaluate the performance of the scintillator system. There were also 85 runs during

which *only* the PISA *Gravitational Collapse* system was in acquisition. For these 85 PISA runs the logbook entry was read in order to double-check them. These runs occurred mainly while the scintillator system was being maintained or calibrated. In addition, one run did not collect any triggers at all (due to its extremely short duration). Given the 286 calibration runs, the 85 PISA runs and the "empty" run, we are left with 680 data runs during which the full detector (i.e., all acquisition μVax 1,2 and 3) or part of the detector was collecting *"normal"* data. We define as *"normal"* data-taking, the state of the detector during which *both* the scintillator and streamer tube systems are simultaneously collecting data which are *not* intentionally induced artificially by the calibration system of the detector (LEDs and LASERs), i.e., they are produced by the cosmic radiation that reaches the detector and the local radioactivity. In figure 3.1 we plot a histogram of the duration of all the 680 runs of our data set. The duration is calculated based on the START-OF-RUN and END-OF-RUN records that are saved in each datafile. As we can see, their duration varies from less than a minute to almost 15 hours. Most of the short-lived runs occurred during the detector's maintenance-dedicated day, while most of the long-lived ones occurred close and beyond the official end of the six-month run when only part of the detector was collecting data (i.e., lower overall detector data rate), thus resulting in the fixed-sized data files being filled at a slower rate.

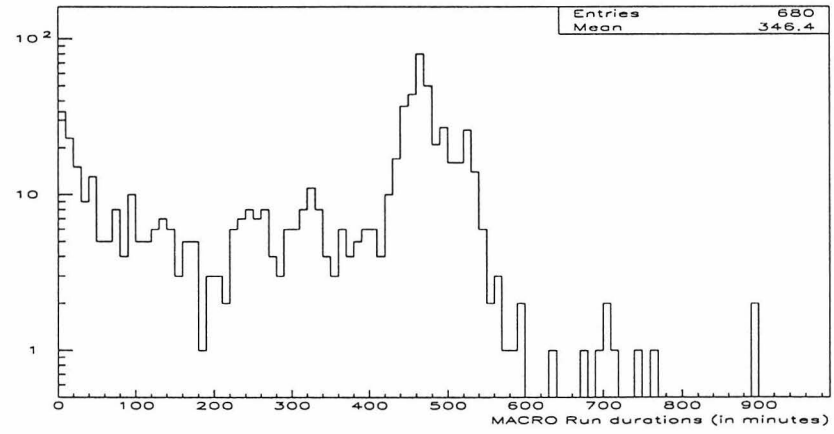

Figure 3.1: Duration (in minutes) of the runs analyzed.

However, more important for the slow monopole analysis is the livetime of the Slow Monopole Trigger (SMT) during each run rather than the duration of the run itself. We define as the SMT livetime on a per μVax basis the time difference between the occurrence of the last and first SMT trigger in that μVax. Given the SMT trigger rate per μVax (three per minute, see figure 3.3), one would expect the SMT livetime to follow the run duration within less than a minute. However, this is not always the case. In figure 3.2 we plot the difference between the run duration and the SMT livetime in each μVax. For a certain number of runs, the SMT livetime was as much as 225 minutes less than the run's duration. The vast majority of this type of difference was caused by problems in the acquisition system of a μVax, problems that resulted in "killing" some or all of the triggers coming from that μVax. Although we do not have full understanding of what exactly was causing these problems, we believe they had something to do with the hardware and/or software of the acquisition μVax(s) (computer errors, power glitches) or the abnormal behavior of some ERP trigger supervisor cards[1].

In principle, we should take this effect into account when calculating our detector's acceptance; however, it is easy to convince ourselves that the error in the acceptance introduced by this is small enough so that we may safely ignore it. Indeed, if we count our detector's exposure in units of μVax-days, then the amount by which we overestimate it by ignoring these abnormal stops of data-taking by the μVax(s) is merely 0.8 out of the total of 467.4, representing a fraction of less than 0.2%.

These 680 data runs constitute the six-month run data set. They reflect a total of 163.5 days[2] of data-taking during which some 2.6×10^6 slow monopole triggers were collected. This will be the starting point of our slow monopole analysis.

---

[1]There were only two occasions where power failures turned off the PMTs of a supermodule (SM) but the acquisition in the full detector was kept running. This effect can not be seen in plot 3.2 because the companion SM within the μVax kept taking data making the μVax livetime appear normal in the 3.2 plot.

[2]The calendar time elapsed from the beginning to the end of the six-month run was 183 days. If we account for 4.5 days worth of data which was lost due to a data copying error, we find that the percentage of running time of the experiment was 91.8%. The remaining 9.2% of the six-month run's (calendar) duration represents the time we spent mostly for calibrating and maintaining the detector.

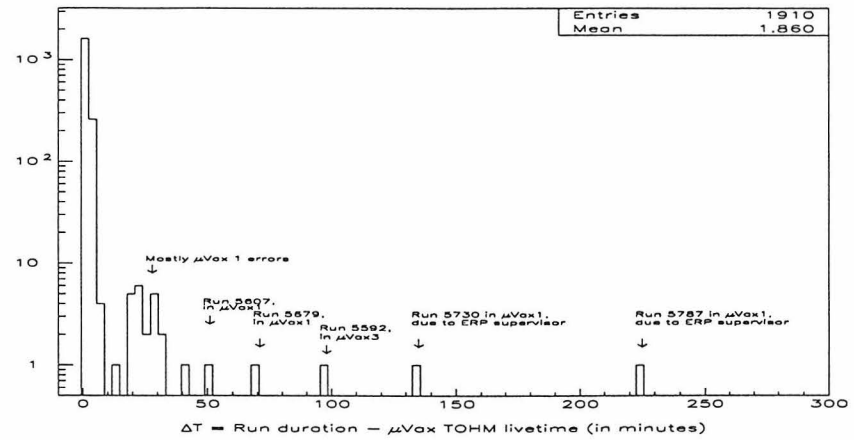

Figure 3.2: Difference between the duration of a run and the SMT livetime (in minutes). In this plot, there is one entry per run per μVax in acquisition. Given that in 595 runs all three μVax were taking data, in 40 runs two μVax were taking data and in 45 runs only one μVax was taking data, one may easily see why we have 1910 entries in this plot. Most of the differences bigger than 5 minutes are related to acquisition problems in a μVax. See text for discussion.

3.2 Slow Monopole Analysis Path

In analyzing these 2.6×10^6 slow monopole triggers, we followed the following path:

- For an undisputed evidence of a rare event recorded by our detector, we first of all require it to be present in more than one of our detector's faces. This requirement enables us to perform redundant measurements of fundamental properties (like the ionization and velocity) of a possible candidate. In order to establish if an event has two or more faces involved, we use the SMT hit registers to count them. The SMT hit registers record the individual scintillator boxes that produced a trigger within an event. From that, we can trivially infer the detector face corresponding to each hit. The full detector is treated as a single box of parallelopided shape with its "ends" (corresponding to the inactive North and South faces) open. If slow monopole hits are present in two or more of the remaining four faces (and these faces belong to a μVax configuration which was able to register a through-going particle[3]), the event is accepted.

[3]See chapter 2 for details.

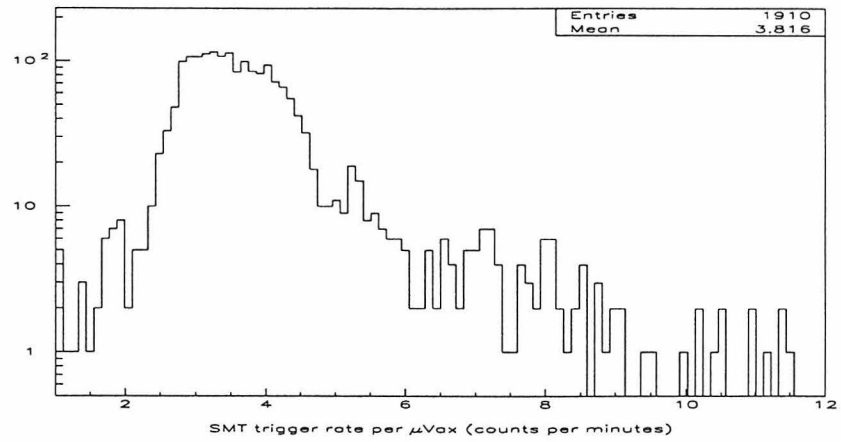

Figure 3.3: SMT trigger rate (number of counts divided by the SMT livetime) on a per μVax basis. As in figure 3.2 there is one entry per run per μVax in acquisition. Due to SMT's very low discriminator threshold, noise and subtle problems of individual PMTs dramatically affect its rate. In addition, sporadic firing of the LED during some runs, power failures affecting part of the μVax and extremely short runs result in entries in the above plot that fall significantly outside the peak of the distribution.

Out of the 2.6×10^6 slow monopole triggers, 1.7×10^5 satisfy this criterion. From now on, we will refer to these events as *monopole coincidence* events. The presence of a slow monopole hit in more than one face of MACRO is the most severe requirement and it practically throws away all the events where either radioactivity had been present in one face only, or through-going muons managed to fire the monopole trigger in one face only or, finally, abnormal PMT behavior of a single scintillator tank was firing the trigger circuit constantly.

- For every monopole coincidence event, we then check the information recorded by the latching scaler in order to make sure that the correct time-of-flight (TOF) and waveform digitizer (WFD) information have been recorded. In particular, we require the latching scaler to have its coincidence bit set. As we have seen in chapter 2, the coincidence bit in the latching scaler is set whenever a monopole coincidence occurs within 1.64 msecs, upon which all the WFDs within the μVax(s) involved in the trigger are stopped and read. Due to the absence of computer busy veto in the SMT hit register, SMT is allowed to record individual box hits over a time interval *much longer* (depending on the event readout data

volume, typically up to 50 msec) than the one for the latching scaler, thus extending to a velocity regime for a hypothetical through-going particle well below our sensitivity. The latching scaler requirements reduce the number of monopole coincidences to 1.5×10^5. One may observe that this cut throws way some 2.5×10^4 events which represent roughly 1% of the total SMT triggers. This is to be expected since the acquisition dead time is of this order.

- For every monopole coincidence event we finally check if the CSPAM trigger and the CSPAM supercounters *corresponding* to the SMT hits had also fired. The CSPAM trigger, being a two-face coincidence trigger within 1 μsec, selects *fast particles* impinging on our detector. For vertical trajectories, the lowest β of a particle selected by CSPAM is of the order of 1.5×10^{-2} which is well above the SMT's sensitivity. The presence of a CSPAM trigger and the association of the slow monopole hits with the CSPAM ones undoubtably flag a monopole coincidence event as actually having resulted from the passage of a fast particle through our detector and it is thus legitimate to use it as a veto[4]. Applying the CSPAM veto reduces the number of monopole coincidences to 1.2×10^4. However, by doing so, we lose our acceptance for slow particles that have short enough pathlengths that make them appear as "fast." We can trivially verify that a particle of β equal to 3×10^{-3} (which represents the upper limit in SMT's sensitivity) spends approximately 1 μsec inside MACRO if its pathlength is 1 meter. This portion of the acceptance is lost by applying the CSPAM veto.

[4]Both the slow and fast particle *triggers* in MACRO are expected to fire in a monopole catalyzing proton's decay event. The CSPAM veto eliminates any sensitivity to this class of events but, as we have seen in chapter 2, MACRO's hardware for the six-month run was already *not* capable of *recording* such an event.

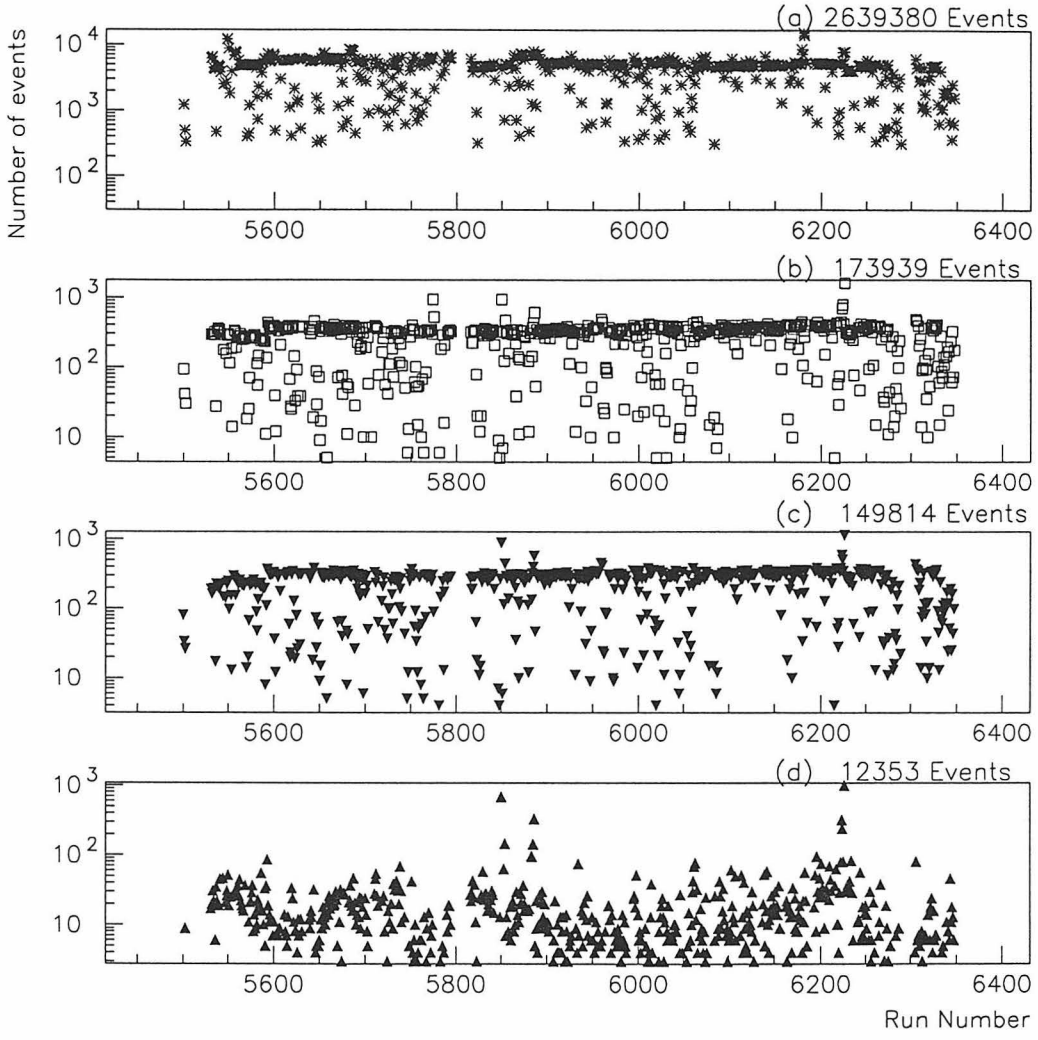

Figure 3.4: Number of surviving events versus Run number for each step of the slow monopole analysis path. In (a) we plot the total number of SMT triggers, in (b) the two-face coincidence events, in (c) the two-face coincidence events that had the correct latching scaler (LS) information and in (d) the two-face coincidence events with correct LS information that passed the CSPAM veto. Notice that Runs with numbers greater than 80000 have been renumbered starting from 5500, while the gap that appears around Run 5800 is due to the 20 runs that were lost due to copying error.

In figure 3.4 we plot for every stage of the analysis path described above, the number of surviving events as a function of run number. There are 11 runs (5850, 5853, 5854, 5883, 5884, 5885, 5886, 6223, 6224, 6225 and 6226) with extremely high coincidence rate which account for more than 25% of the total number of monopole coincidence events; so the question that naturally arises is, what is the nature of these high trigger rate runs?

3.3 Noisy Runs

The vast majority of the events collected during these 11 runs we just mentioned are related to noise present in our detector. Typical waveforms that were recorded during these runs depict bipolar oscillations as in figure 3.5. In order to have a more complete picture of the overall condition of MACRO during these runs, we also looked at the streamer tube activity over the same period of time.

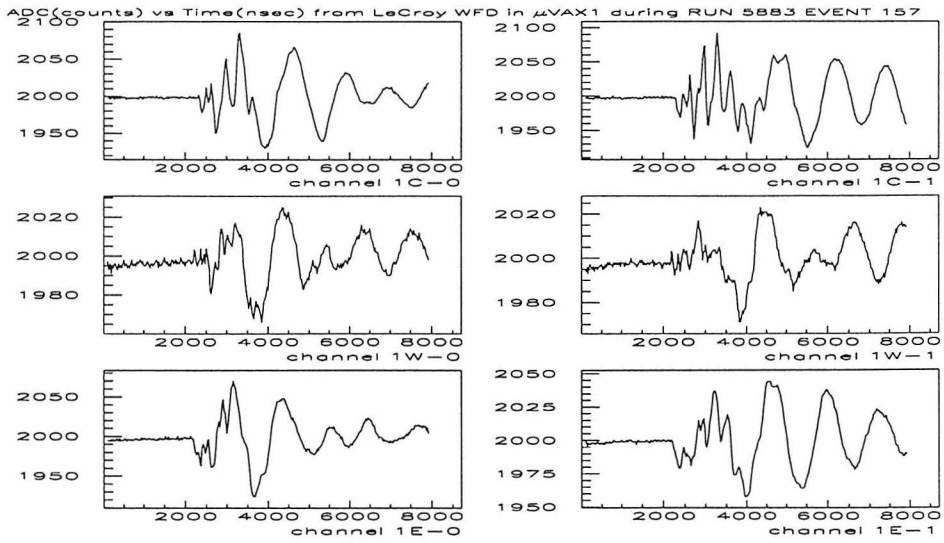

Figure 3.5: Typical waveforms of a noise-related event collected during the 11 noisy runs. Here, the WFD raw counts are plotted versus time (in ns) for event 157 of Run 5883.

In figure 3.6 (top plot) we plot the number of streamer tube wire hits versus event number for Run 5883. On the same plot, we have superimposed the histogram with

the event numbers of the SMT monopole coincidence events for the same run. Typical (muon) events in MACRO result in 10-30 streamer tube wires firing; in this plot we can clearly see that the SMT events are indeed events with extremely high streamer tube activity which is actually known to be noise-related. In addition, this activity in both the scintillator and streamer tube systems comes from the same "location" within the detector: supermodule (SM) 1 (figure 3.6 bottom) for the case of Run 5883. The simultaneous presence of noise in both the streamer tubes and the SMT is one of the typical features of noise-related events in our detector. In addition, SMT noise events generally span over *every* face of an SM and include many scintillator boxes (in most cases *every* single box within an SM). They tend to come in bursts and, within an event, the time-of-flight recorded between detector faces is predominantly zero. All of the above characteristics of the SMT noise events are summarized graphically in figure 3.7.

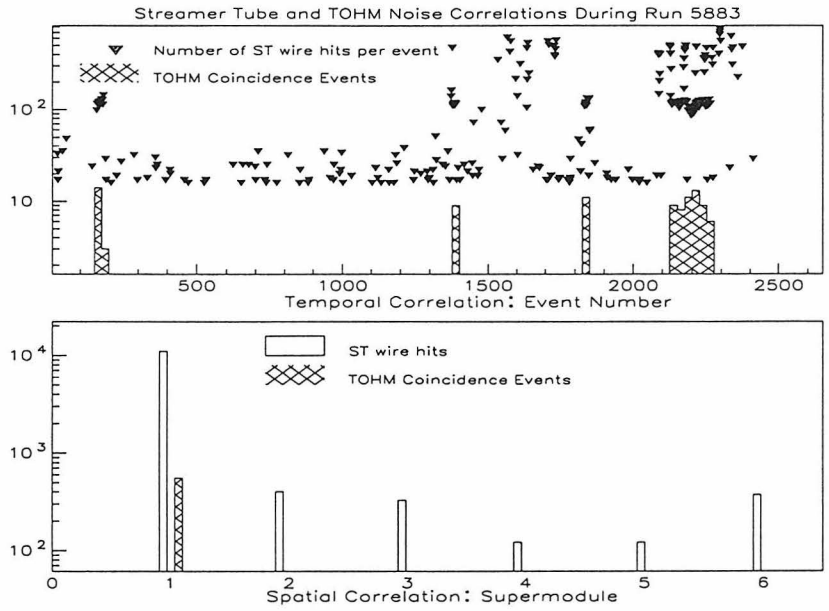

Figure 3.6: Top plot: Number of streamer tube (ST) wire hits versus event number and SMT event numbers during run 5883. Events with more than 30 ST wire hits are generally considered noise-related; one may notice that the SMT events occurred in simultaneity with this kind of ST noise events. Both were also coming from the same place, SM1 (bottom plot).

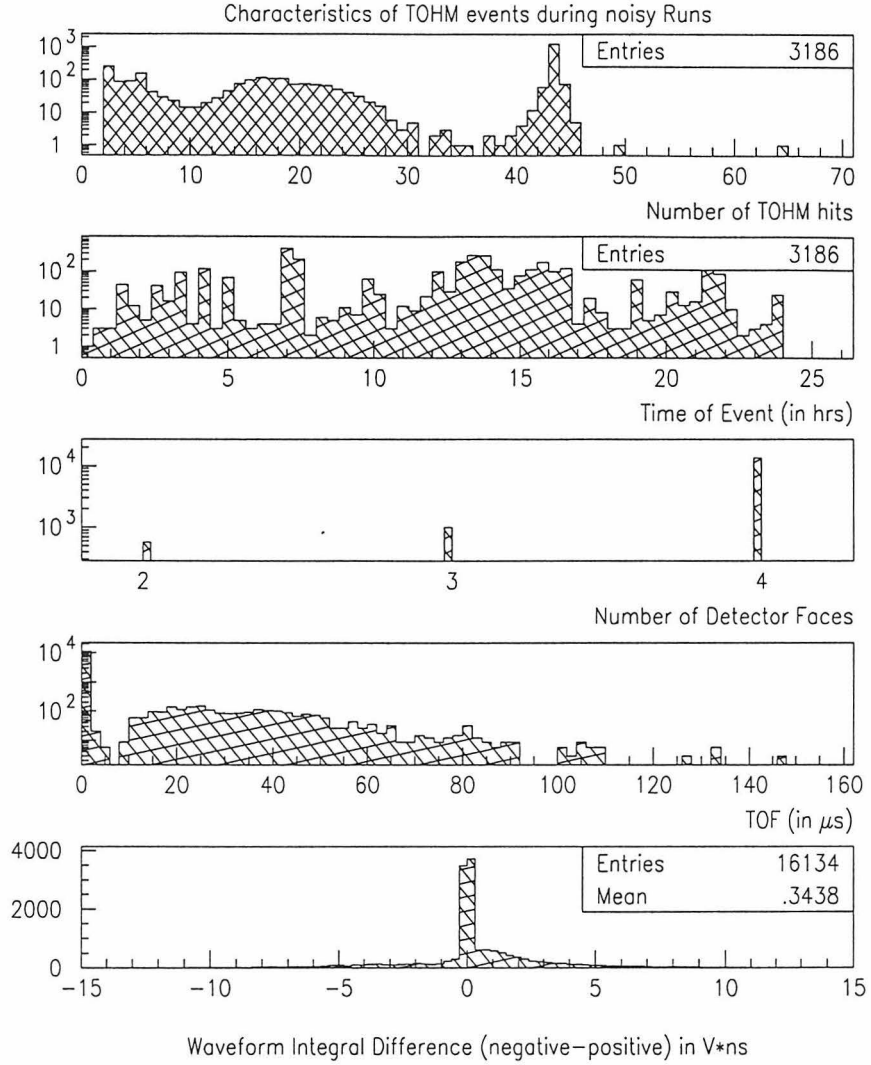

Figure 3.7: (a) Number of scintillator boxes that fired during an event: in most of the cases all 46 boxes within an SM produced a trigger. (b) Time distribution of SMT events: there are 11 plots (one for each run) superimposed. Events tend to occur in bursts and in most of the cases occurred during daytime. (c) Number of detector faces within an SM that had an SMT trigger. (d) Time-of-flight as measured by the latching scaler: while the vast majority of events had zero TOF, there were some that extended to tens of μsecs, corresponding to situations where noise was present in MACRO over longer timescales. Finally in (e) we plot the difference between the "positive" and "negative" portions of the recorded waveforms. The distribution peaks at zero, suggesting the approximate axial (around the pedestal) symmetry that we would expect for bipolar oscillations.

Being reasonably convinced that the events collected during these 11 runs are *not* monopoles[5], and sacrificing a minimum portion of our livetime (<2%), we have chosen to discard them for the slow monopole analysis purposes. This represents the *only* run selection that was imposed on the slow monopole analysis data set and reduces the number of monopole coincidence events to 9167.

3.4 Hardware Performance Checks

An initial scanning of the waveforms of the remaining events revealed that certain waveform digitizer channels were failing systematically to record the waveforms of the triggering events. As we have explained in chapter 2, the waveform digitizer system is of fundamental importance for the identification of a slow monopole candidate and any failure of it results in MACRO being completely insensitive for *recording* any such event. In figure 3.8 we plot a typical monopole coincidence event that involved a detector face which had hardware problems. Needless to say, for this kind of event, no waveform-only based decision can be drawn and under no circumstances the corresponding part of the detector (in the case of the event shown in 3.8, the bottom layer of SM2) may be treated as "sensitive" over that period. Rejecting these kinds of events is legitimate as long as the appropriate acceptance correction is introduced. We have used muon data to monitor the performance of the WFDs and make sure that they were functioning properly during *each and every run*[6]. Based on that, we have selected to *ignore* any SMT *hit* corresponding to a WFD channel that was found to have a hardware problem during the corresponding run; in this way every monopole coincidence event is guaranteed to have valid waveforms recorded for *every* SMT hit.

---

[5]It would not be true to state that *all* the events of these runs were noise-related. As we will be able to explain in upcoming chapters, muons, multimuons and showers "escape" into the monopole dataset for various reasons and so did during these runs. However, they represent a rather negligible fraction of the total events.

[6]A description of the detector monitoring procedure and the acceptance calculation may be found in Appendix E.

The requirement that the monopole coincidence event involve well-functioning WFD channels reduces the number of remaining events to 8219.

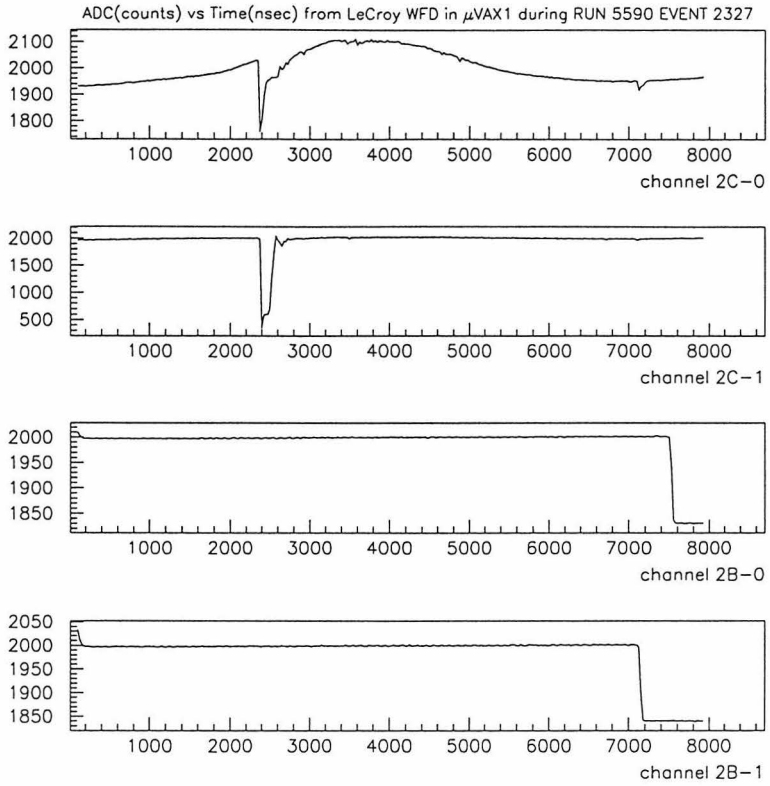

Figure 3.8: Typical two-face monopole coincidence event which had "incomplete" waveform information. In this specific one, a muon came in from the 2C face of MACRO and exited from 2B but the corresponding to 2B WFD channel failed to record the exit waveform. Step-like waveforms as in 2B-0/1 and/or completely unphysical pedestals (> 3000 counts) were the typical features of waveforms recorded by broken WFD channels.

3.5 Monopole Events

A summary of the effects of the slow monopole analysis physics cuts, the run selection criteria and the WFD hardware requirements on the slow monopole data set is presented in table 3.1. In this table, the quoted percentage of livetime loss is with respect to the six-month run's livetime (163.5 days) while the quoted percentage of

acceptance loss is with respect to the acceptance of the full lower MACRO detector to an isotropic flux of particles which are only required to hit a sensitive "piece" of the detector. The effect of the CSPAM veto to the acceptance depends on the β of the hypothetical particle (the quoted percentage is for β=0.002)[7], while the effect of the WFD hardware checks to the acceptance varies from run to run (the quoted percentage is for a typical MACRO run that had WFD hardware problems). With minimum loss of acceptance and livetime and no loss of sensitivity at all, the above three physics cuts combined with the run selection criteria and the WFD hardware requirements yielded 8219 monopole coincidence events collected over a period of 160.7 days, among which we will look for a signature of a slow moving particle going through our detector. Given the large amount of information (> 10 Kbytes) that is available for each of these events, one may see why hand scanning all of them is a rather difficult (but not really impossible) task. Our major concern was to try to establish a computer-driven pattern recognition method that will *efficiently* select any signature of a rare event while *effectively* rejecting all the background. The ideas behind and functionality of such an algorithm will be the subject of the next chapter.

Table 3.1: Summary of the Slow Monopole Analysis Path, Run Selection and WFD Checks for the monopole data set.

Cut Description	Events Remaining	Livetime lost	Acceptance lost
1. SMT trigger anywhere in MACRO	2639380	—	—
2. SMT hits in *at least two* faces	173939	—	17.7%
3. Correct Latching Scaler Information	149814	1.0%	—
4. No CSPAM trigger (SMT-CSPAM matched)	12353	—	1.2%
5. Exclude eleven Runs with high rate	9167	1.7%	—
6. Require well-functioning WFDs	8219	—	13.0%

[7]In general, the slower the particle, the smaller the effect on the acceptance is. This is because as the particle slows down, the fraction of the pathlengths that may result in a TOF less than 1μsec becomes smaller and smaller.

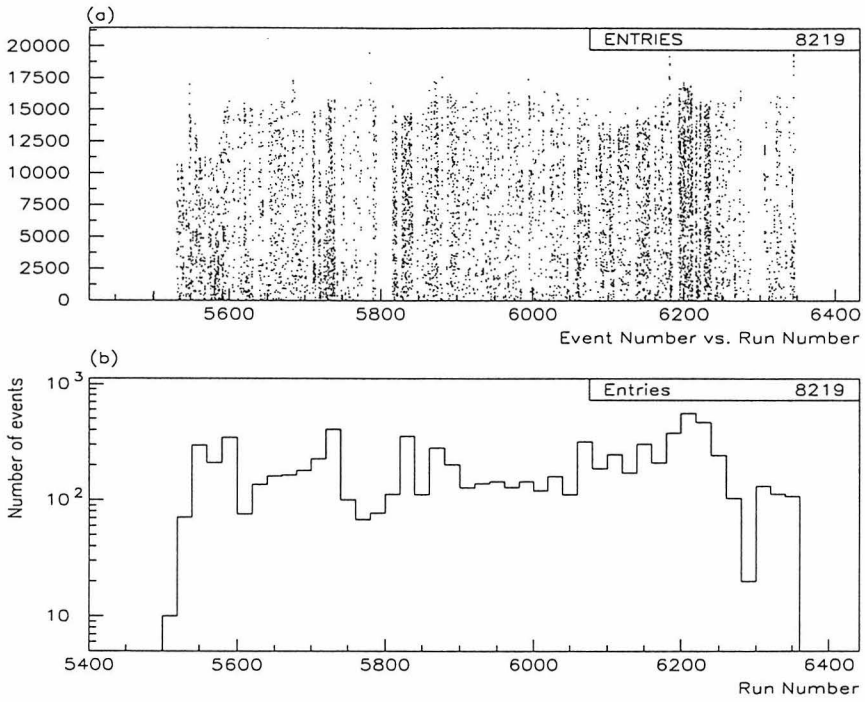

Figure 3.9: Monopole coincidence events that passed the slow monopole analysis path, the Run selection and the WFD hardware requirements. Every event is identified by its run and event numbers. A scatter plot of these pairs for all the monopole coincidence events is depicted in the figure (a). This is practically a time distribution plot: the run number axis reflects the elapsed time since the beginning of data-taking and the event number axis reflects the time elapsed since the beginning of any given run. In figure (b), we see the projection of the top figure onto the run number axis. Notice that as in a previous plot, Runs with numbers greater than 80000 have been renumbered starting from 5500.

Chapter 4

Wavelets and the Haar Decomposition

Over the last few years, "wavelets" have received great attention from a wide spectrum of scientists and engineers. Used primarily by engineers in signal and image processing [34], "wavelets ideas" have also emerged in a great variety of fields among which are biomedical research, economics, stochastic processes, geophysics and many more [83]. In this chapter we introduce the concept of wavelets and present the applicability of one of its simplest forms –the Haar decomposition– in the context of waveform analysis[1].

4.1 From the Fourier to the Wavelet Transform

Given an analog signal $f(t)$, the standard Fourier transform (FT),

$$\hat{f}(\omega) = \frac{1}{\sqrt{2\pi}} \int dt e^{-i\omega t} f(t), \tag{4.1}$$

has traditionally been used to study its spectral behavior. However, the Fourier coefficients thus obtained represent the signal over its entire support; a slight change of the signal in a small region of time t_0 will affect the entire spectrum and any attempt to read off from that the *location in time* of this change will not be easy.

Twentieth century scientists and engineers were not the first ones who had to deal with time-frequency localization problems; musicians were facing the same problem many centuries ago in music notation where the composer had to instruct the performer what notes (i.e., frequencies) to play at a given moment. It is actually thanks

[1]The mathematical description of the wavelet theory presented hereafter follows the one of ref. [33]; the reader is referred there for further details. An equally rigorous treatise on the same subject may be also found in ref. [31], chapters 1, 2 and 3.

to *Guido d'Arezzo*, a monk who just after the turn into the second millennium devised and organized what became the standard musical dictionary of western music.

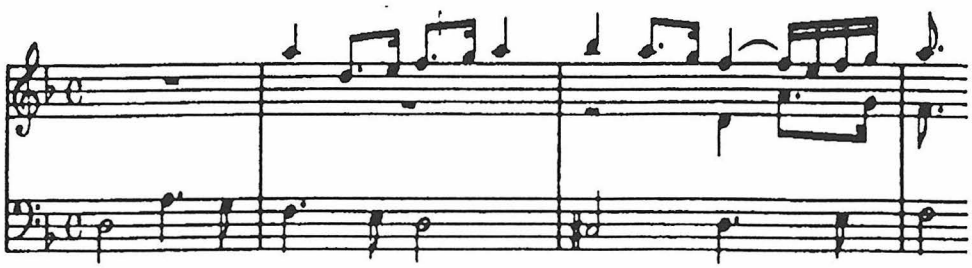

Figure 4.1: Excerpt from J.S.Bach's Art of Fugue, Fugue VI. One may imagine the "time" axis running along the music staff and the "frequency" axis perpendicular to that. The meter defines the "sampling rate."

Similar to music notation, the wavelet transform, by using "good" time-windows in analyzing a signal, merits the time-frequency localization that the Fourier transform lacks. The general form of the wavelet transform (WT) of a signal $f(t)$ is given by the following integral:

$$W_\psi f(\alpha, b) = |\alpha|^{-\frac{1}{2}} \int dt f(t) \overline{\psi(\frac{t-b}{\alpha})}, \tag{4.2}$$

where α and b are real and ψ is assumed to be a complex (in general) function satisfying the condition:

$$\int dt \psi(t) = 0. \tag{4.3}$$

As we can see, the WT takes the inner product of f with a doubly indexed family of functions $\psi^{\alpha,b} = |\alpha|^{-\frac{1}{2}} \psi(\frac{t-b}{\alpha})$ –the "wavelets functions"– which are obtained by *dilations* (by α) and *translations* (by b) of the "mother wavelet" ψ. In figure 4.2 we plot a few "members" of the "wavelet family" defined by a frequently used ψ: $\psi(t) = (1-t^2)exp(-\frac{t^2}{2})$, the so-called Mexican hat function. Notice that the normalization[2] for all the wavelet functions has been chosen so that $\|\psi^{\alpha,b}\| = \|\psi\|$ for all α and b. The integral 4.2, where b and α vary continuously (with the constraint $\alpha \neq 0$) over

[2]Here we have used the standard notation for the norm, i.e., $\|\psi\| = \sqrt{\int dt |\psi(t)|^2}$.

R, defines the so-called *continuous wavelet transform.*

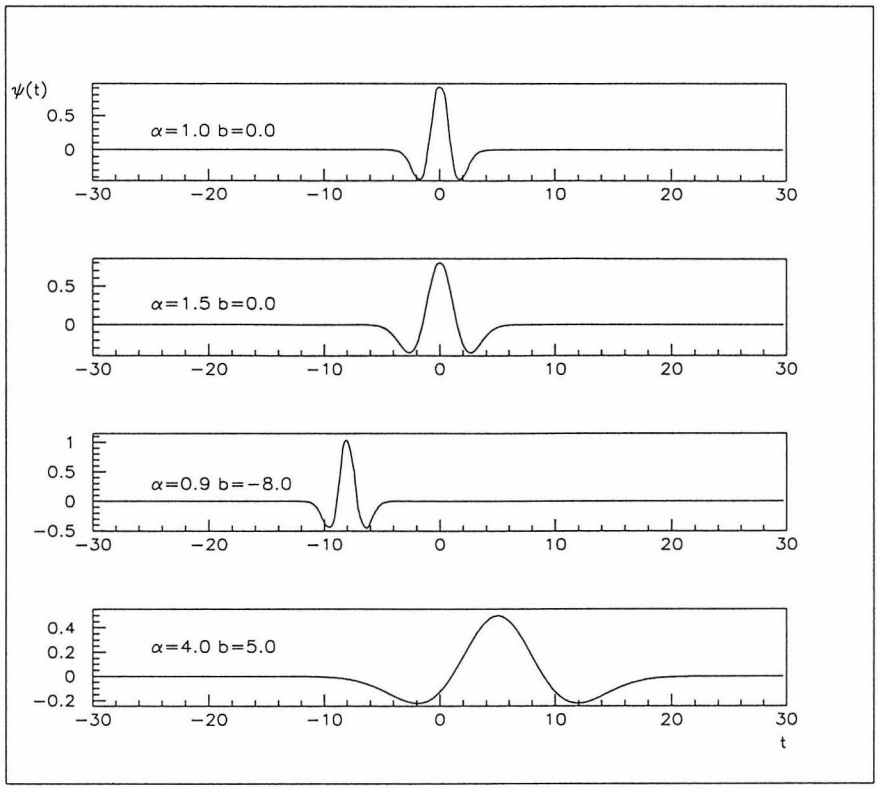

Figure 4.2: Wavelet functions $\psi^{\alpha,b}$ generated by the "mother" function $\psi(t) = (1 - t^2)exp(-\frac{t^2}{2})$. Parameter b shifts the center of ψ, while α compresses or stretches it.

Given the integral defining the WT, the question that naturally arises is how one proceeds in selecting the analyzing functions ψ; qualitatively speaking, we may see that the wavelet functions ψ, like the Mexican hat function mentioned above, should be well localized both in frequency and time. From the practical point of view, though, ψ will be accepted if one may reconstruct the original function f from the values of its wavelet transform $(W_\psi f)(\alpha, b)$. It can be shown ([33] [31]) that the *inverse wavelet transform* is given by

$$f = {C_\psi}^{-1} \int \int \frac{d\alpha db}{\alpha^2} W_\psi f(\alpha, b) \psi^{\alpha,b}, \tag{4.4}$$

where

$$C_\psi{}^{-1} = 2\pi \int d\omega \frac{|\hat{\psi}(\omega)|^2}{|\omega|}. \tag{4.5}$$

The admissibility condition for a wavelet function ψ is that C_ψ be finite so that the integral 4.4 exists. This condition is automatically implied by equation 4.3.

For most practical purposes though –namely, fast numerical implementations– our wavelet model is not required to keep α and b varying continuously over R; instead, simple *integral shifts* of ψ may cover all of R, namely:

$$\psi(t - nb_0(\alpha)), \tag{4.6}$$

where $n \in Z = \{..., -1, 0, 1, ...\}$ and $b_0(\alpha) > 0$[3] is the translation parameter which is fixed for given α. Like b, α –representing the frequency domain– is also partitioned into consecutive "octaves" (frequency bands) starting from a fundamental "octave" $\alpha_0 > 1$[4] and obtaining the rest by taking integral powers of α. In this case we may rewrite 4.2 as follows:

$$W_\psi^{m,n} f = \alpha_0^{-\frac{m}{2}} \int dt f(t) \psi(\alpha_0^{-m} t - nb_0) \quad m, n \in Z, \tag{4.7}$$

where for simplicity we assumed that ψ is now real and we substituted $b = nb_0(\alpha) = n\alpha_0^m b_0$. Integral 4.7 defines the so-called *discrete wavelet transform.* In both the continuous and discrete WT, the analyzing functions ψ *adjust their resolution* in order to match their scale (frequency): small values of α yield high-frequency spectral information of the signal and in order to give better accuracy the resolution (time-interval) is finer; on the other hand, for high values of α which yield low-frequency information, the resolution becomes coarser. This is the unique property of the wavelet transform that makes it attractive to many applications: its capability to "zoom-in" and "zoom-out" into the time-frequency domain accordingly.

[3]Obviously there is no loss of generality in this assumption. Incidentally, one may recognize b_0 as the *sampling rate* at scale α.

[4]As with b_0, this assumption does not harm the generality of the argument.

4.2 The Haar Basis

We have seen in the previous section how practical purposes have led us to the discrete wavelet transform. We will now introduce a particular family of wavelet functions by choosing $\alpha_0 = 2$ and $b_0 = 1$ such that the functions

$$\psi_{m,n}(t) = \alpha_0^{-\frac{m}{2}} \psi(\alpha_0^{-m} t - n b_0) \quad m, n \in Z, \tag{4.8}$$

satisfy the following two conditions:

- orthonormality, i.e.,

$$\langle \psi_{i,j} \psi_{k,l} \rangle := \int \psi_{i,j} \psi_{k,l} dt = \delta_{i,k} \delta_{j,l} \quad i, j, k, l \in Z, \tag{4.9}$$

- closure, i.e., every square integrable function $f(t)$[5] can be written as a linear combination of $\psi_{m,n}$

$$f(t) = \sum_{m=-\infty}^{\infty} \sum_{n=-\infty}^{\infty} c_{m,n} \psi_{m,n}(t), \tag{4.10}$$

  where $c_{m,n}$ are given by 4.7.

The family of wavelets defined by equation 4.8 and the corresponding wavelet transform are called *dyadic*[6] because we have imposed the scales to vary over the dyadic sequence $2^m (m \in Z)$. The simplest and actually the oldest example of a dyadic wavelet ψ that satisfies the above two conditions ([33] [31]) is the Haar [53] function given by

$$\psi^{Haar}(t) = \begin{cases} 1 & \text{if } 0 \leq t < \frac{1}{2} \\ -1 & \text{if } \frac{1}{2} \leq t < 1 \\ 0 & \text{otherwise.} \end{cases} \tag{4.11}$$

[5] In the context of Lebesgue measure theory, the set of all those functions is denoted as $L^2(R)$.
[6] From the Greek numeral *δύο* (dyo) for number 2.

For reasons that will become apparent shortly, we will define another family (through equation 4.8) of functions ϕ, associated with the Haar basis:

$$\phi^{Haar}(t) = \begin{cases} 1 & \text{if } 0 \leq t < 1 \\ 0 & \text{otherwise.} \end{cases} \tag{4.12}$$

In the real world, though, input signals $f(t)$[7] are measured at a finite resolution

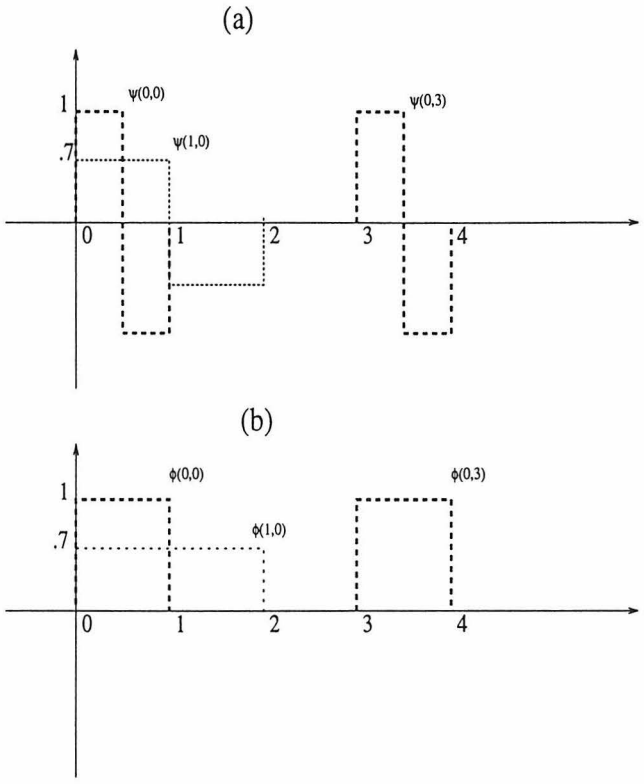

Figure 4.3: (a) Haar wavelets $\psi_{m,n}$ corresponding to m, n have support over the interval $[2^m n, 2^m(n+1)]$. (b) Associated to Haar $\psi_{m,n}$'s are the $\phi_{m,n}$ family of functions which have the same support as $\psi_{m,n}$.

determined by the sort of hardware that is used to register them. Let us assume for a moment that $f(t)$ consists of $N = 2^J$ samples $f(t_i), i = 0...(N-1)$ and let us

[7] As one may have noticed, we have been dealing with analog signals defined in the time domain; this is not a requirement or restriction for the wavelet theory to work. One can imagine replacing all functions of t with corresponding functions of space x (or even more generally of $\vec{r}$) and have everything working fine as long as the conjugate Fourier space –through equation 4.1– can be defined. Playing between space and time variables is signal ($f(t)$) and image ($f(\vec{r})$) engineers' favorite ([82] [81]).

normalize this *finest* scale to 1. According to 4.8 and 4.11 the Haar wavelets for this scale will then be

$$\psi_{1,n}^{Haar}(i) = \frac{1}{\sqrt{2}} \begin{cases} 1 & \text{if } i = 2n \\ -1 & \text{if } i = 2n+1 \quad where \quad n = 0...(2^{J-1}-1) \\ 0 & \text{otherwise,} \end{cases} \tag{4.13}$$

and the discrete wavelet transform 4.7 of $f(t_i)$ will read

$$c_{1,n} = W_{\psi^{Haar}}^{1,n} f = \sum_{i=0}^{N-1} f(t_i)\psi_{1,n}^{Haar}(i) = \frac{f(t_{2n}) - f(t_{2n+1})}{\sqrt{2}}, \tag{4.14}$$

As we can see, the Haar coefficients 4.14 of $f(t_i)$ in the 1^{st} scale are nothing but the *differences*[8] of adjacent samples! For the 1^{st} scale there are $N/2 = 2^{J-1}$ such coefficients which describe the *details* of our input signal $f(t_i)$ in the finest scale. As a short notation, we will define as the "*details-yielding operator*" $\hat{D}_m$, the operator which, acting on $f(t_i)$ returns the sequence of all the Haar coefficients at scale m, i.e.,

$$\hat{D}_m = \left\{ W_{\psi^{Haar}}^{m,n} \right\}_{n=0...(2^{J-m}-1)}. \tag{4.15}$$

Remaining in scale 1, we now return to equation 4.10 from which we may calculate the *approximation* at this scale of the original signal $f(t_i)$ by subtracting from it the *details* we have just calculated:

$$f(t_i) - \sum_{1,n=0}^{2^{J-1}-1} c_{1,n}\psi_{1,n}^{Haar}(i) =$$

$$\left\{ \begin{array}{ll} f(t_i) - \frac{f(t_i)-f(t_{i+1})}{\sqrt{2}} \frac{1}{\sqrt{2}} & \text{if } i = 2n \\ f(t_i) - \frac{f(t_{i-1})-f(t_i)}{\sqrt{2}} (-\frac{1}{\sqrt{2}}) & \text{if } i = 2n+1 \end{array} \right\} =$$

[8] Up to a normalization factor.

$$\left\{ \begin{array}{ll} \frac{f(t_i)+f(t_{i+1})}{2} & \text{if } i = 2n \\ \frac{f(t_{i-1})+f(t_i)}{2} & \text{if } i = 2n+1 \end{array} \right\} =$$

$$\frac{f(t_{2n})+f(t_{2n+1})}{2} =: S^{1,n}_{\psi^{Haar}} f, \tag{4.16}$$

where $n = \lfloor \frac{i}{2} \rfloor$, i.e., $n = 0...(2^{J-1} - 1)$.

As we can see, the *approximations* $S^{1,n}_{\psi^{Haar}} f$ of the signal are nothing but the average of f at a scale which is twice as coarse; this can in turn be written as a linear combination of the $\phi^{Haar}_{1,n}$, the family of functions associated to the Haar family we have defined earlier (equation 4.12). Indeed, given the definition of ϕ's, we may rewrite the last equation as:

$$S^{1,n}_{\psi^{Haar}} f = \frac{f(t_{2n}) + f(t_{2n+1})}{\sqrt{2}} \phi^{Haar}_{1,n} = a_{1,n} \phi^{Haar}_{1,n}, \tag{4.17}$$

where we have denoted as $a_{1,n}$ the expansion coefficients of $S^{1,n}_{\psi^{Haar}} f$ onto the ϕ's. In analogy to the "*details-yielding operator*" $\hat{D}_m$, we will define here the "*approximations-yielding operator*" $\hat{A}_m$ for any scale m as the operator which acting on $f(t_i)$ returns the sequence of all the $a_{m,n} \phi^{Haar}_{m,n}$, i.e.,

$$\hat{A}_m = \left\{ S^{m,n}_{\psi^{Haar}} \right\}_{n=0...(2^{J-m}-1)}. \tag{4.18}$$

The derivation above outlines the fundamental ideas ([80] [51]) of *multiresolution* techniques: we write successive coarser and coarser approximations to f (the $S^{m,n} f$) by averaging f over larger and larger intervals and at every step we write the difference between the approximation at scale j and the one at $j-1$ as a linear combination of Haar (or any other orthogonal wavelet basis) functions:

$$S^{j,k} f = f(t_i) - \sum_{m=1}^{j} \sum_{n=0}^{2^{J-m-1}-1} c_{m,n} \psi_{m,n}(i) = S^{j-1,k} f - \sum_{n=0}^{2^{J-j-1}-1} c_{j,n} \psi_{j,n}(i) \tag{4.19}$$

It is rather trivial to see that the coarse signal $S^{j-1,k} f$ provides the signal components for the scales below $j-1$ (j ... J). Indeed, by repeating the steps for the derivation of

4.14, we find that at scale 2 (notice that at this scale the Haar wavelets have twice as big support compared to this at scale 1 but less ($\frac{1}{\sqrt{2}}$) weight), the Haar coefficients are

$$c_{2,n} = W^{2,n}_{\psi^{Haar}} f = \frac{f(t_{4n}) + f(t_{4n+1}) - f(t_{4n+2}) - f(t_{4n+3})}{2}$$

$$= \frac{a_{1,4n} - a_{1,4n+2}}{\sqrt{2}} \tag{4.20}$$

where $n = 0...(2^{J-2} - 1)$,

i.e., the Haar coefficients at scale 2 are equal to the Haar coefficients of the *approximation* signal coefficients at scale 1. It is up to induction to convince ourselves of the validity of this argument for any scale j.

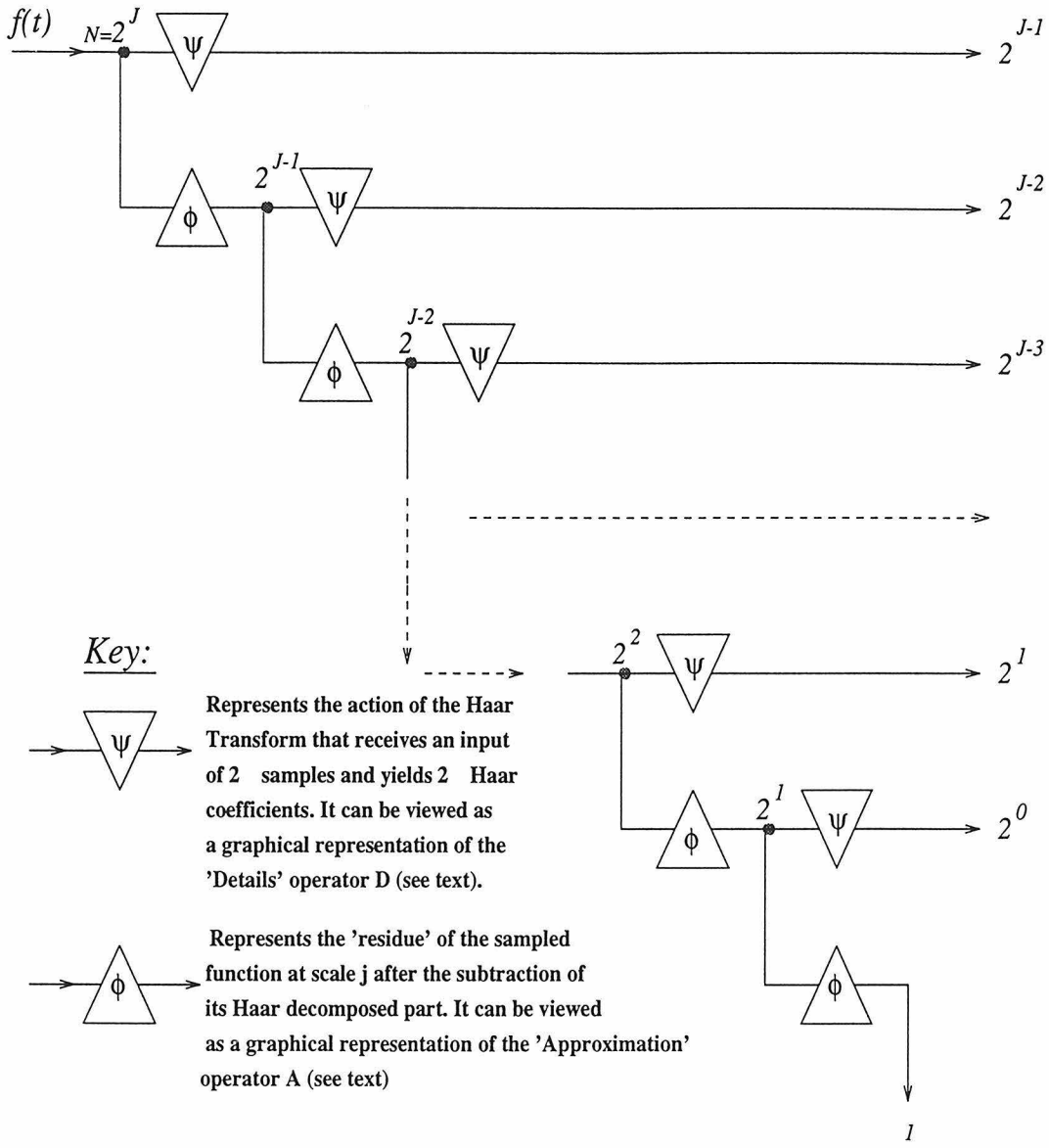

Figure 4.4: The "Haar machine": a multiresolution "ladder" which decomposes the original signal of $N = 2^J$ samples into projections onto successive resolution scales by using the families of functions ψ and ϕ. One can see that this is an $O(N)$ operation.

4.3 A Haar-based Filter for Particle Identification

Following our discussion in the previous section, an issue that remains open is how much information is carried by the Haar representation of a signal and most importantly if this information is well adapted for extracting the content of signals that differentiates them. In order to investigate this issue, we will work out the Haar decomposition of some typical waveforms that the MACRO detector has been recording.

4.3.1 Haar transform of typical MACRO waveforms

We have implemented a fast discrete wavelet algorithm and its inverse utilizing the Haar basis we have described in the previous section. For any –digitized– input signal $f(t_i)$ $(i = 1...2^J)$ we calculate the Haar coefficients and the approximation signals according to equations 4.15 and 4.17. Our input signals have 256 samples in which case their Haar transform is computed over $J = 8$ scales. Waveforms recorded by MACRO may be in general categorized into two groups: the first one includes the relatively fast and sharp waveforms corresponding to single muons and isolated radioactivities (hereafter referred to simply as muons and radioactivities) while the other one includes the relatively wide pulses corresponding to "fat" muons (resulting from multi-muons and/or showers), radioactivity pile-ups and monopole-like ones. In figures 4.6 and 4.7, for every scale j we plot the 2^{J-j} Haar coefficients of a radioactivity pulse (fig 4.5a) and a muon pulse (fig 4.5b) respectively as recorded by the LeCroy 2261 waveform digitizers (WFDs), while next to that we plot the approximation of the original signal at that scale. In figures 4.8, 4.9 and 4.10 we do the same for a radioactivity pile-up (fig 4.5c), "fat" muon (fig 4.5d) and a (simulated) monopole-like waveform (fig 4.5e). At each scale m –with the exception of the last one– we detect and record the *absolute maximum* value and its *location* (m, n) of the Haar coefficients $|W^{m,n}f|$, obtaining in this way what we will refer to from now on as the *Haar multiscale profile* of the waveform.

The Haar multiscale profile of the five waveforms we have just plotted will then be:

Table 4.1: Haar multiscale profiles for an isolated radioactivity (left) and a muon (right) waveform.

	radioactivity		*muon*	
Scale	Maximum	Location	Maximum	Location
1	35.36	53	640.64	122
2	140.00	26	694.00	61
3	100.41	13	56.21	32
4	46.50	7	627.25	16
5	71.24	4	519.37	8
6	46.13	2	364.75	4
7	26.25	1	256.94	2

Table 4.2: Haar multiscale profiles for a radioactivity pile-up (left), "fat" muon (center) and monopole-like (right) waveform.

	radioactivity pile-up		*"fat" muon*		*monopole-like*	
Scale	Maximum	Location	Maximum	Location	Maximum	Location
1	8.49	106	485.08	123	11.96	45
2	8.00	53	1036.50	64	10.00	64
3	9.90	27	1470.43	31	42.61	10
4	7.75	14	1685.50	16	33.17	7
5	3.18	7	2663.14	8	56.45	3
6	9.88	4	1880.88	4	53.46	2
7	11.31	1	1324.32	2	61.26	1

These numbers represent the multiscale information that we will analyze further.

4.3.2 Analysis of the Haar multiscale information

Let us focus for a moment on the muon and radioactivity waveforms and their Haar decompositions. Since the Haar coefficients at a given point measure the local derivative (equations 4.14 and 4.15) of the signal at each scale, Haar maxima are produced at *all* scales $j \in [1, 7]$ in the vicinity of where the signal varies sharply.

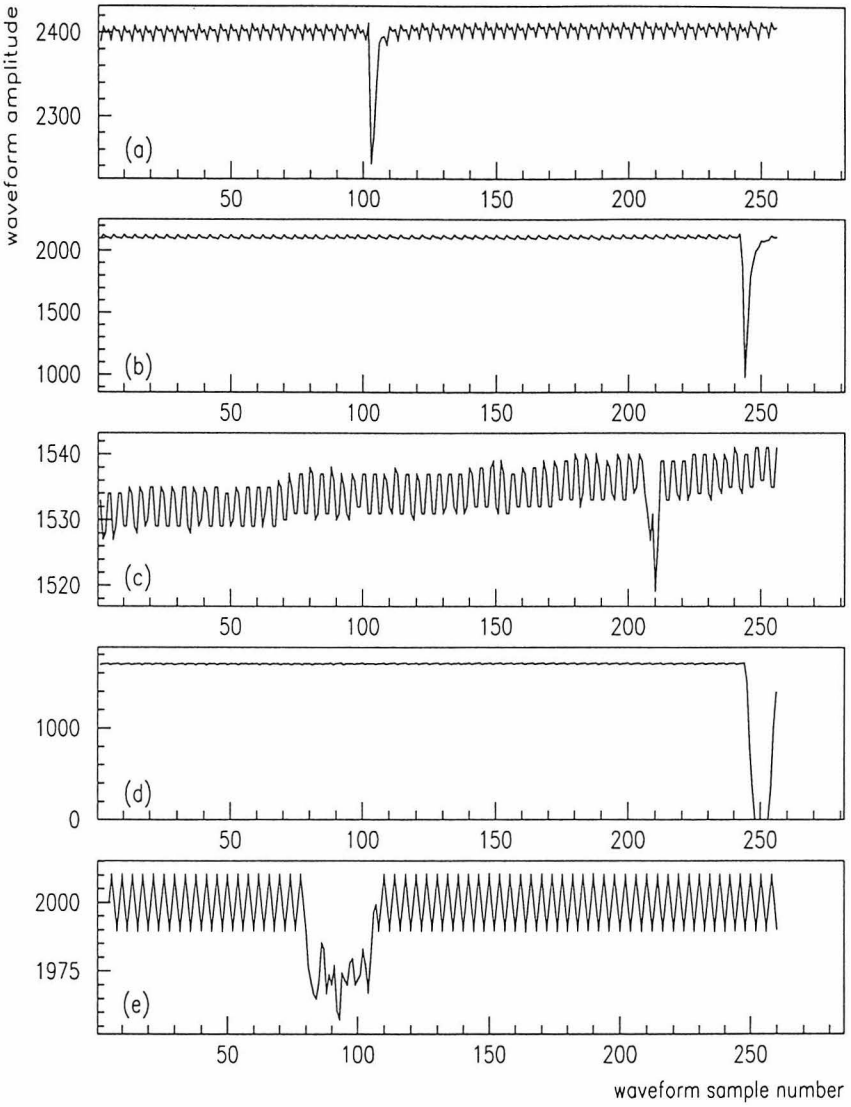

Figure 4.5: Typical MACRO waveforms as recorded by the LeCroy 2261 WFDs: (a) isolated radioactivity, (b) single muon (c) radioactivity pile-up (d) "fat" muon and (e) simulated monopole-like waveform corresponding to a monopole of $\beta = 10^{-3}$. Note that the vertical scale is not constant.

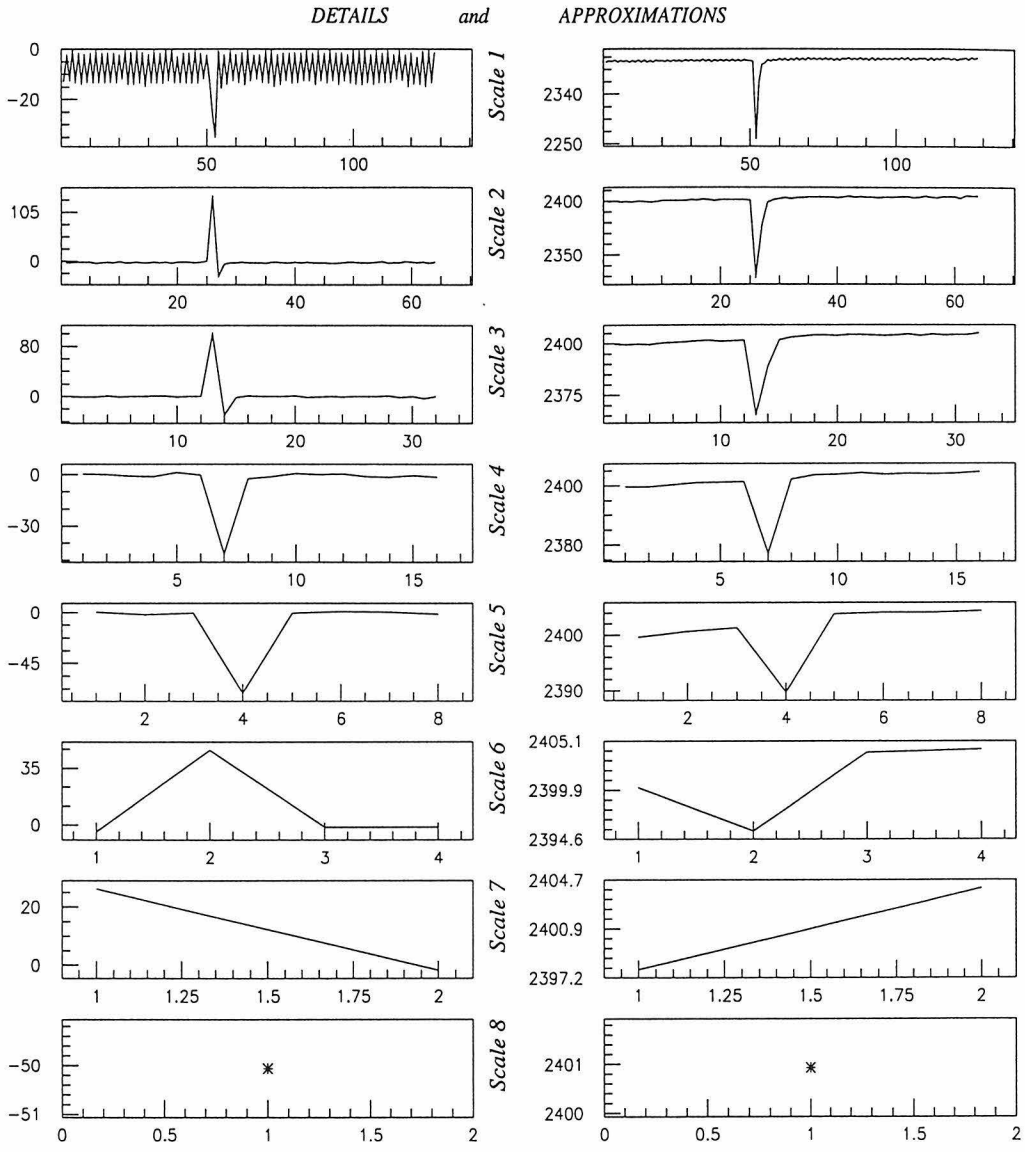

Figure 4.6: For the isolated radioactivity waveform plotted in figure 4.5a we here plot its Haar coefficients ("details," left) and its "approximations" (right). For each scale j, there are 2^{8-j} different coefficients, each one corresponding to groups of 2^j samples of the original waveform.

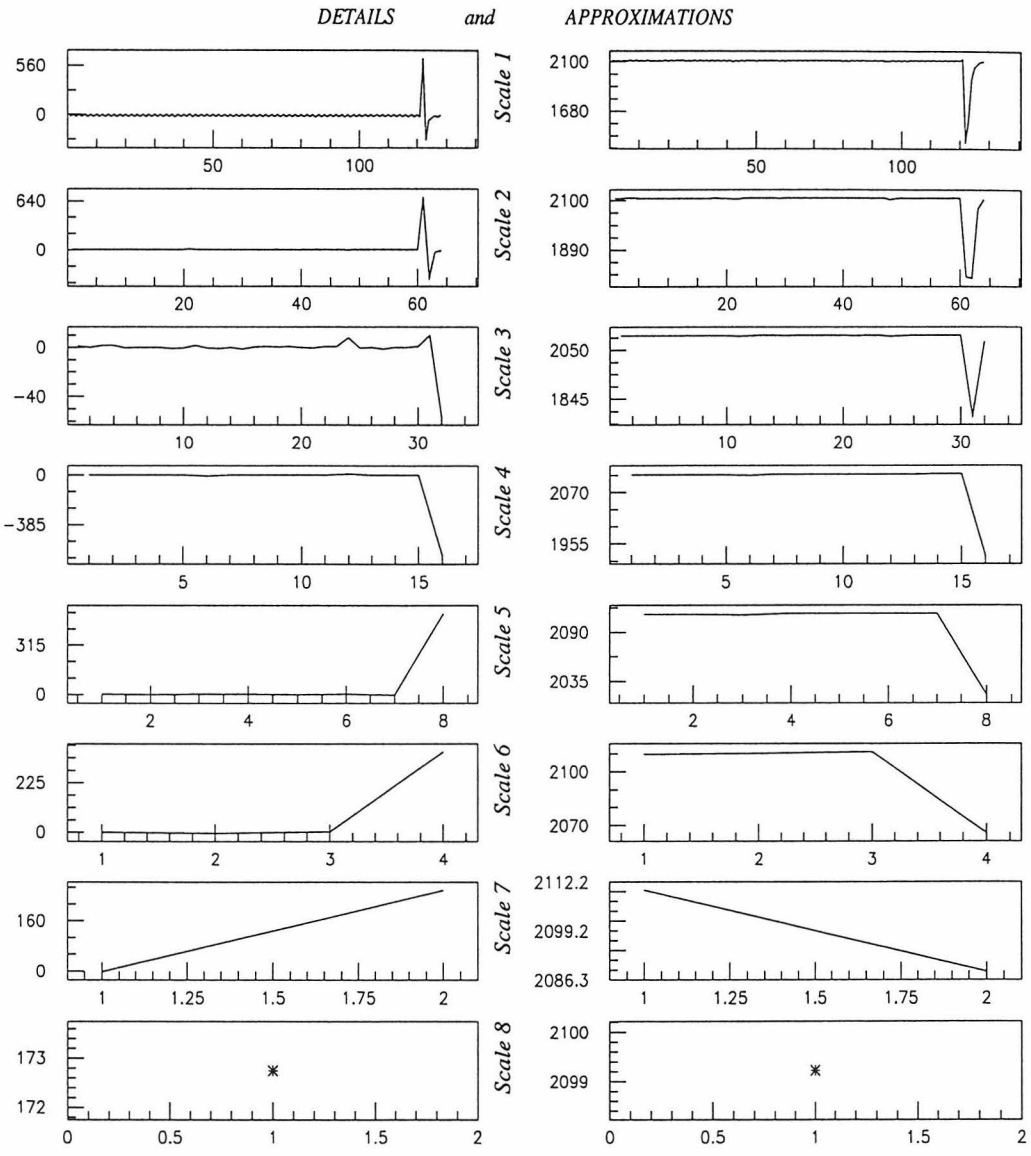

Figure 4.7: For the single-muon waveform plotted in figure 4.5b we here plot its Haar coefficients ("details," left) and its "approximations" (right). For each scale j, there are 2^{8-j} different coefficients, each one corresponding to groups of 2^j samples of the original waveform.

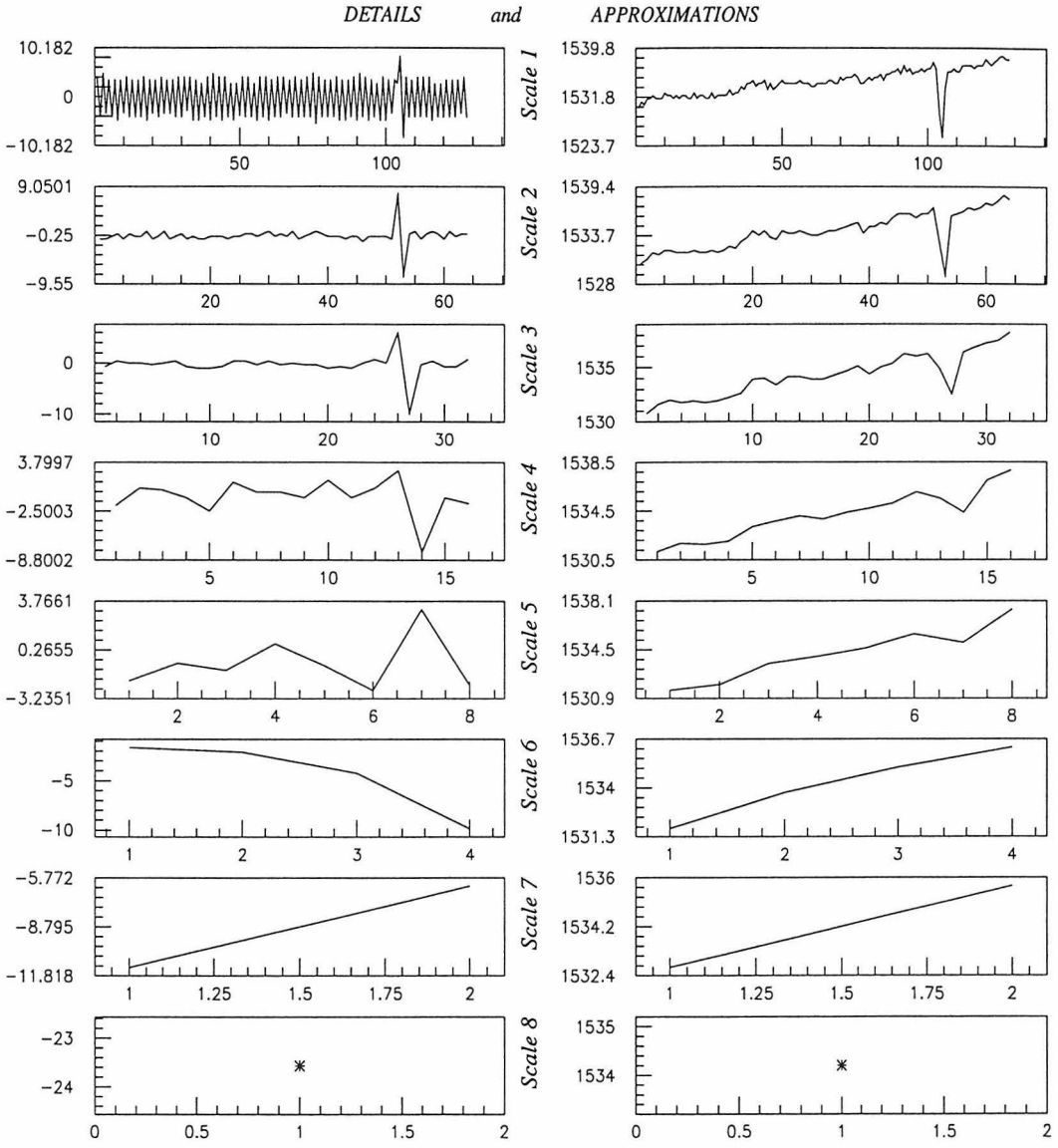

Figure 4.8: For the radioactivity pile-up waveform plotted in figure 4.5c we here plot its Haar coefficients ("details," left) and its "approximations" (right). For each scale j, there are 2^{8-j} different coefficients, each one corresponding to groups of 2^j samples of the original waveform.

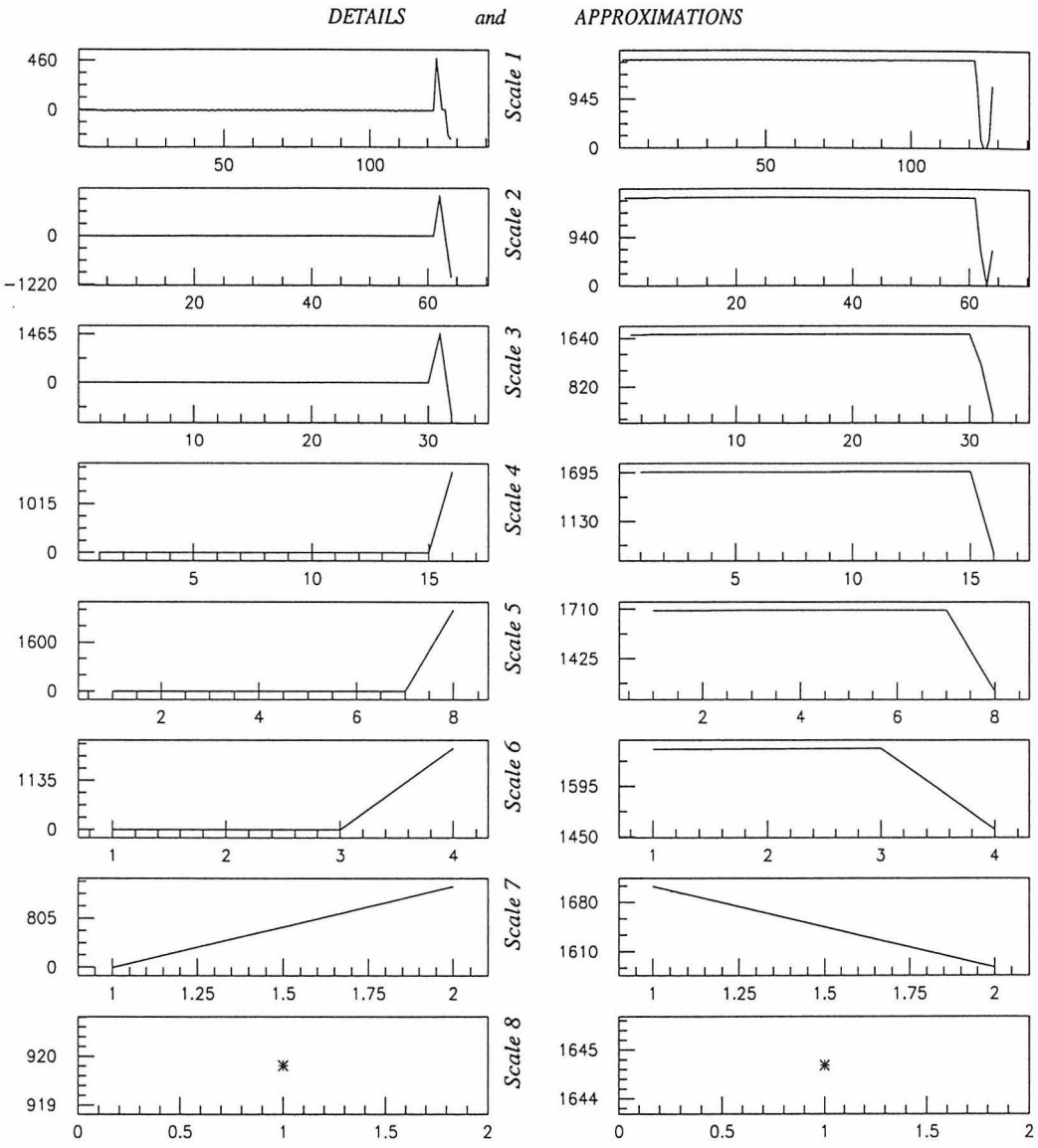

Figure 4.9: For the "fat" muon waveform plotted in figure 4.5d we here plot its Haar coefficients ("details," left) and its "approximations" (right). For each scale j, there are 2^{8-j} different coefficients, each one corresponding to groups of 2^j samples of the original waveform.

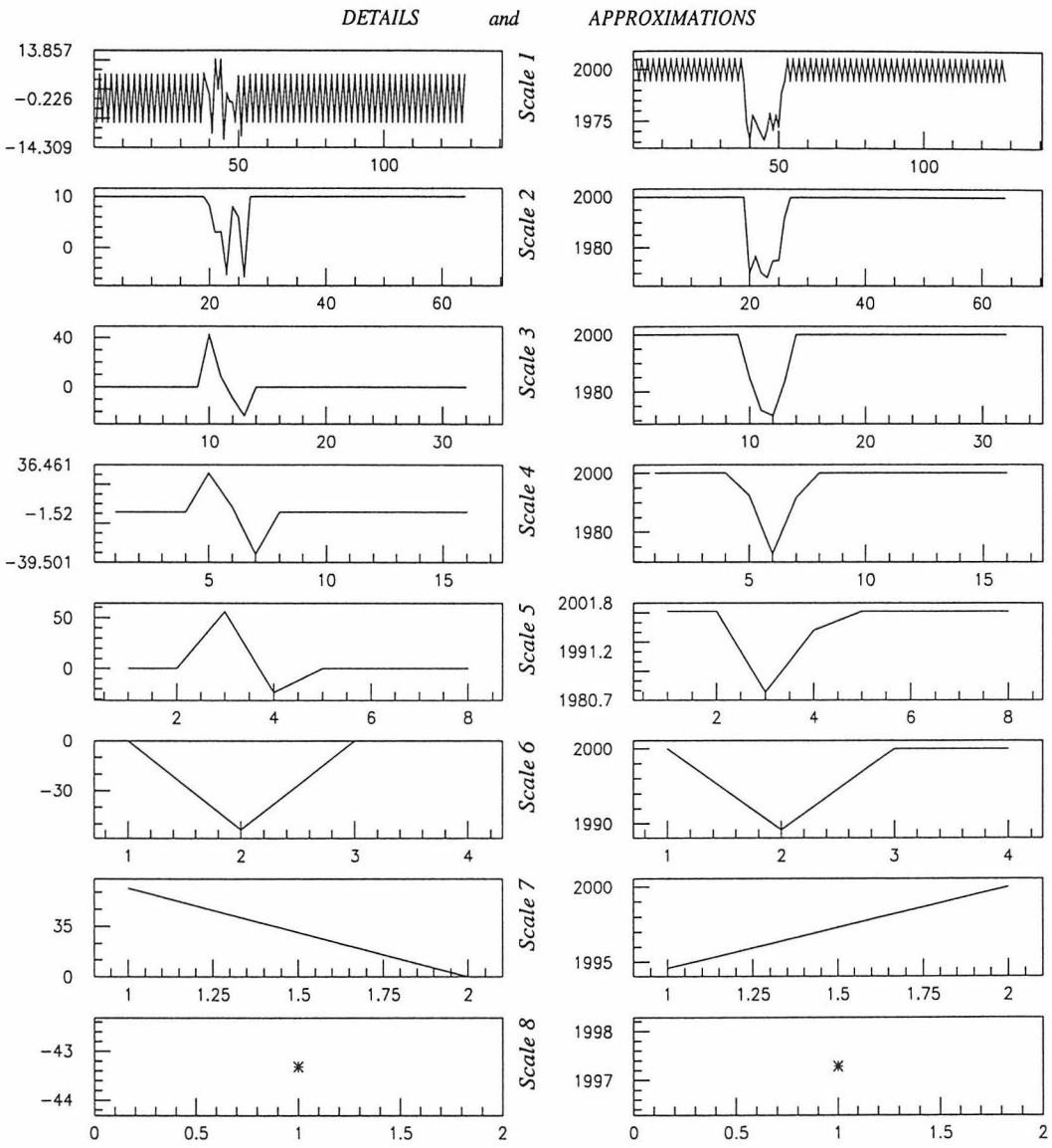

Figure 4.10: For the (simulated) monopole-like waveform plotted in figure 4.5e we here plot its Haar coefficients ("details," left) and its "approximations" (right). For each scale j, there are 2^{8-j} different coefficients, each one corresponding to groups of 2^j samples of the original waveform.

If the muon or radioactivity waveforms were Dirac's δ-like, the Haar coefficients at the point of sharp variation would have been monotonically decreasing over scales with the wavelet maxima propagating perfectly among consecutive scales. The finite width of the muon and radioactivity signals results in the propagation being "almost perfect" and the decreasing scheme being "almost" monotonic. But, let us quantify our notion of maxima propagation and maxima decreasing.

Definition 1: Let $t_j \in [0, 2^{J-j} - 1]$ be the location of the Haar maximum at scale j. We say that the maximum at scale j *propagates* to the maximum at the coarser scale $j+1$ if the location t_{j+1} of the Haar maximum at scale $j+1$ satisfies the following inequality:

$$t_j - 2 \leq 2t_{j+1} \leq t_j + 2. \tag{4.21}$$

We say that the Haar maxima are *aligned* if the above condition holds for *all* scales. As a short notation, in presenting the "alignment" of a Haar decomposition, we will use the decimal representation of a binary number whose bits are set to "1" for each scale that satisfies the condition above.

Definition 2: Let $\{h_i\}_{i=1}^{J-1}$ be the set of all the absolute maxima of the Haar transform for each scale i (i.e., $h_i = max|W_{\psi Haar}^{i,n} f|_{n=0}^{2^{J-j}-1}$). We call the "Haar global max" *hmax*, the maximum of h_i, and the "Haar focus" *hfoc*, the scale i where hmax occurs.

In analogy to the Fourier transform, we introduce as a measure of the "energy content" of a scale i the quantity ${h_i}^2$. Strictly speaking, the complete energy content of a scale is represented by the sum $\sum_{n=0}^{2^{J-j}-1} |W_{\psi Haar}^{i,n} f|^2$; however, ${h_i}^2$ makes the major contribution into this sum and more importantly reflects the point where the variation is maximum.

Definition 3: Let ΔE be the difference of the "energy content" of the lower scales minus the one of the higher scales defined as follows:

$$\Delta E = (|h_1|^2 + |h_2|^2 + |h_3|^2) - (|h_5|^2 + |h_6|^2 + |h_7|^2), \tag{4.22}$$

where we assumed that the original signal is composed of 256 samples and analyzed over 8 resolution scales.

We will say that our signal is "low frequency biased" if $\Delta E \leq 0$; otherwise, we will say that it is "high frequency biased."

Based on the Haar profile of the five types of waveforms we have been analyzing and according to definitions 1 through 3, we fill the following table:

Table 4.3: Haar multiscale profiles for various types of waveforms.

Waveform	Alignment (decimal/binary)	hmax	hfoc	ΔE
radioactivity	63/111111	140	2	23040
muon	63/111111	694	2	426405
radioactivity pile-up	31/011111	11	7	-2
"fat" muon	60/111100	2663	5	-8912050
monopole-like	56/111000	61	7	-7738

For radioactivity and muon waveforms, since they are relatively sharp, their Haar coefficients decay among consecutive scales thus resulting in hmax being present in and the "energy content" being strongly focused at the *first scales.* Their "alignment" is perfect among all scales while the value of hmax relates to the maximum pulse height of the waveform. On the other hand, for the radioactivity pile-ups, "fat" muon and monopole-like waveforms, the kind of discontinuity that is picked up by the Haar transform is qualitatively different: it is no longer sharp which translates to Haar coefficients that increase among consecutive scales resulting in hmax being present in and the "energy content" being strongly focused at the *last scales.* We will thus move ahead in constructing the fundamental terms of our *"wavelet dictionary"*

by means of which we will perform pattern recognition.

Definition 4: For a 256 sample signal $f(t)$, for which we have constructed its Haar decomposition over 8 scales, we define as the *"sharp signal filter"* the requirement that the Haar transform be "high frequency biased" ($\Delta E > 0$), be aligned and have the global max present within the first four scales (i.e., $hfoc \leq 4$). On the other hand, we define as the *"wide signal filter"* the requirement that the Haar transform simply be "low frequency biased" ($\Delta E < 0$), not necessarily aligned, and the global max be present within the last five scales (i.e., $hfoc \geq 3$).

Although at this moment the parameters we have chosen for the filters construction may seem to be *ad hoc*, their selection will be justified by the detailed study of the filters' performance on real and simulated waveforms coming up on the next chapter.

Chapter 5

Trigger and Analysis Efficiency Studies

In previous chapters we described both the dedicated hardware and the proposed software tools for performing this monopole analysis. One of the first considerations for a detector is its sensitivity, which in our case translates into studying MACRO's capabilities for detecting a slow moving particle of a given velocity and ionization yield. During the six-month run, light-emitting diodes (LEDs) have been used to simulate monopole events of various velocities and light yields. In this chapter we are going to use this calibration data to study the performance of both the Slow Monopole Trigger (SMT) system as a slow particle trigger and the wavelet filter as a pattern recognition method.

5.1 The LED Calibrations

Consisting mainly of two Hewlett Packard (HP) programmable pulse generators and a sophisticated pulse distribution network, the LED calibration system installed in MACRO[1] offers great capabilities in simulating the passage through MACRO of particles of various trajectories, velocities and ionization yields. Each HP pulser offers two analog outputs which are fully programmable in pulse height, width and delay. Having two HP pulsers allows us to drive the four PMTs at the ends of two scintillator boxes in an independent way, thus creating *any* two tank interaction that we want. As we have described in chapter 2, for all of the monopole events, the Latching Scaler (LS) provides the fundamental TDC information while the LeCroy waveform digitizers (WFD) provide the ADC information. Using the LED calibration system, we can calibrate both of them. The TDC calibrations consist mainly of calculating

[1] See chapter 2 for details.

the slope and offset that will convert the latching scaler counts to time, while the ADC calibrations will measure the sensitivity of the WFDs for detecting a monopole or any other slowly moving particle as a function of its velocity and light yield.

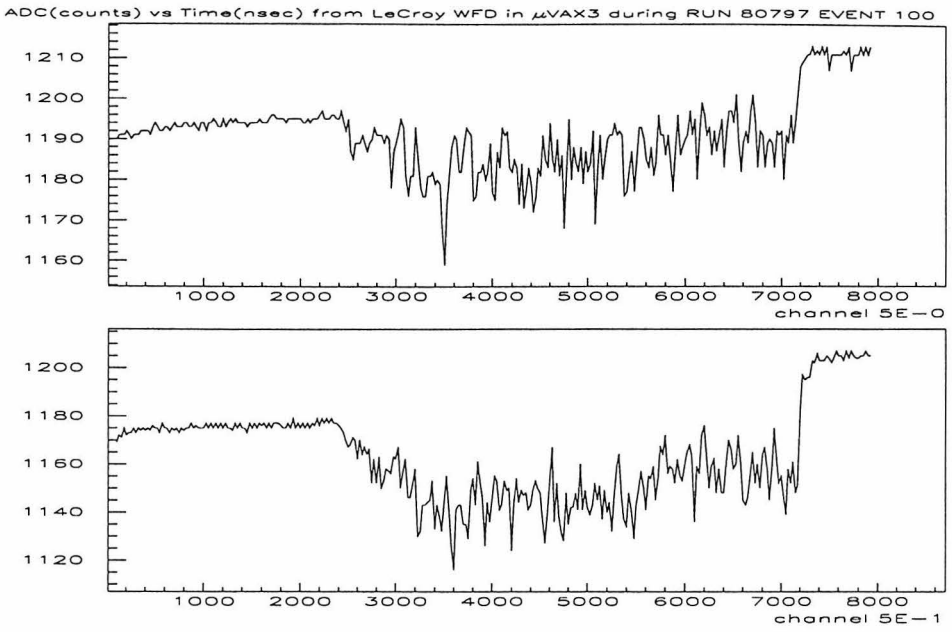

Figure 5.1: Typical LED-induced event as recorded by the WFDs during RUN 80797. The pulse width driving the LEDs was approximately $5\mu s$. The recorded waveforms show the typical LED risetime. A few thousand photoelectrons are included in each of the waveforms.

5.1.1 TDC calibrations

During the timing calibrations, by varying the delay between the pulses driving the two tanks, we may simulate any TOF and compare the expected number with the one that the latching scaler records. In general, for every delay setting, the pulse width is adjusted so that the ratio of pulse width to pulse delay is consistent with the passage of a particle of constant β, i.e., the ratio should be equal to the ratio of the pathlengths that the hypothetical particle traverses when going through a single scintillator box and when going through MACRO (from one face to the other) for the simulated trajectory. We have generated a series of delay settings covering the full range of the expected monopole velocities. In figure 5.2b we plot the TOF as

measured by the latching scaler in μVax 3 when the delay was set to 50 μsecs. Various two-tank combinations were fired during that LED calibration run; as a result, the obtained measurement spreads over a range of values that (primarily) reflects the different trigger processing times of the individual Leaky Integrator (LI) channels that were involved in each two-tank combination[2]. On occasions where the same two-tank combination is involved in the measurement, the spread is appreciably lower, reflecting only the latching scaler time resolution and the possible jitter in the trigger formation. This is shown in plot 5.2a. For each delay setting, we calculated the mean latching scaler TDC value and its standard deviation and we performed a weighted linear fit in order to obtain the slope and offset. Using calibration data from two LED runs, we show in plot 5.2c the result of the fitting for the latching scaler in μVax 3. The slope reflects the fact that the latching scaler is being clocked by a 10MHz clock, while the offset is small enough to be ignored. For the purpose of the slow monopole analysis, the obtained slope and offset parameters provide good handles for calculating the β of a slow monopole candidate with reasonable accuracy. Although periodic checks of the latching scaler timing calibration parameters indicated some slight variation (less than 0.5% for the slope and a few counts for the offset), for all practical reasons we will consider them as stable and uniform in all MACRO[3].

[2]Prior to the beginning of the six-month run, we had carefully checked the trigger processing time of all the LI cards in MACRO; at that time, we had observed variations of the order of 500ns among different LI cards which is consistent with what is shown in plot 5.2. This is basically due to the variation in the values of the resistors and capacitors used on the LI boards.

[3]After all, this is not an upward going muon type of analysis which relies heavily on the TOF measurement with a resolution at the level of $0.5ns$ and where the timing calibrations are essential.

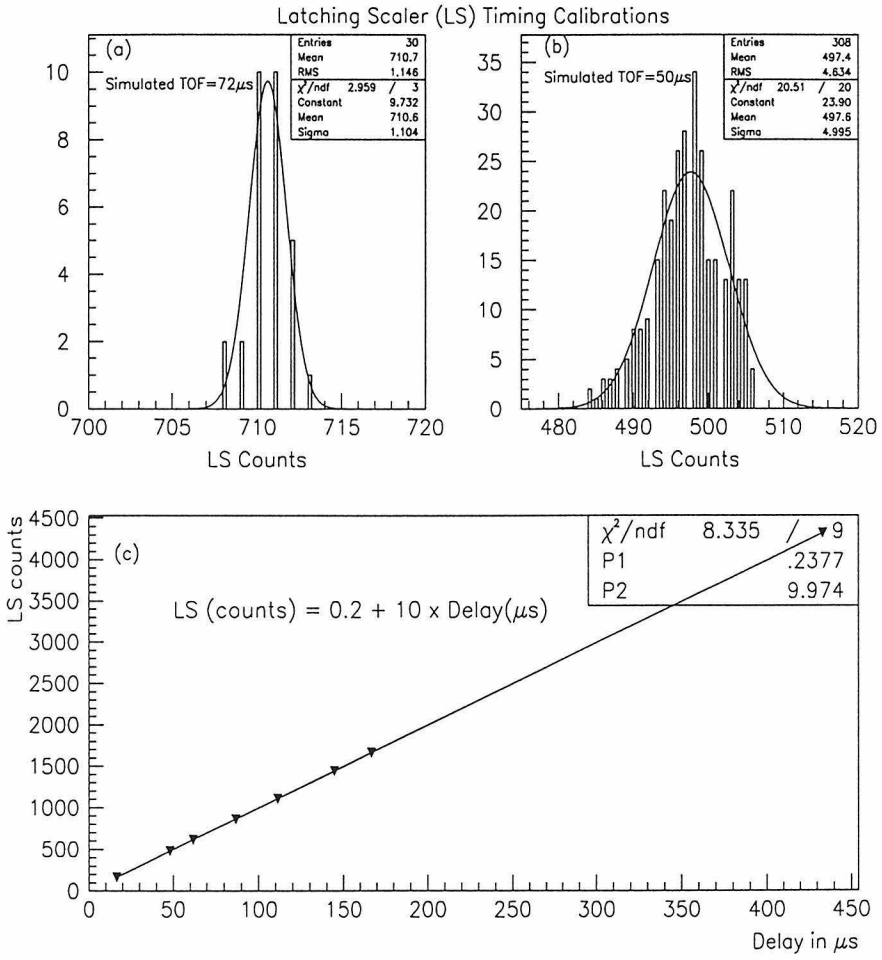

Figure 5.2: Typical timing calibration plots for (a) a single two-tank combination and (b) several two-tank combinations superimposed. The variation of the trigger processing time of the various LI cards involved results in the apparent widening of the TOF distribution in (b). When only a single two-tank combination is used to perform the measurement, the distribution is significantly narrower with its width reflecting the LS resolution and the possible trigger jitter. The averages and standard deviations of this kind of plots are used as entries in the linear fit shown in plot (c).

5.1.2 ADC calibrations

In order to validate our monopole search result, it is essential to demonstrate the sensitivity of the apparatus in detecting one. This is the purpose of the LED ADC calibration runs. During these runs, by adjusting the pulse width D of the pulses driving the LEDs, we are able to simulate the passage of particles of various velocities; for each pulse width setting, by changing the amplitude of the pulse driving the LEDs, we are able to simulate various monopole light yields L, measuring in each one of them the detector's efficiency. As for the timing calibrations, ADC calibrations took place regularly during the six-month run (almost on a weekly basis). However, not all of them covered the same velocity and ionization yield ranges. Scanning the whole velocity-ionization parameter space with high statistics is a rather lengthy procedure which would have resulted in dramatic detector downtime if performed in its full length on a weekly basis. During these calibration runs, for each WFD channel, only one scintillator box belonging to that channel was fired at a time in order for the recorded waveforms to have a one-to-one correspondence with the SMT triggers. We have actually used these recorded waveforms in order to calculate the amount of light L that was involved in each trigger. In figure 5.3 we plot a histogram of the waveform integral values (L) for one of the LED light settings corresponding to the passage of a monopole that spent $3.8\mu s$ inside a scintillator tank. For this given width ($3.8\mu s$), several other settings of the LED pulse height scanned the response of the SMT at various light levels L.

Knowing how many events were generated[4], and counting in how many of them the SMT did fire, we thus obtain the SMT efficiency versus the amount of light L "seen" by the PMT (and measured with the WFD) for every given pulse width D. In order to present our sensitivity measurement in detector-independent units, we normalize the average light yield (waveform integral) of each setting to the average light yield of the minimum ionizing particle L_{min} (see appendix B[5]), while for every

[4]Roughly 500 for every LED pulse width - pulse height combination.

[5]We use the conservative estimate of 30V×ns for the waveform integral of a minimum ionizing muon traversing 19cm of scintillator.

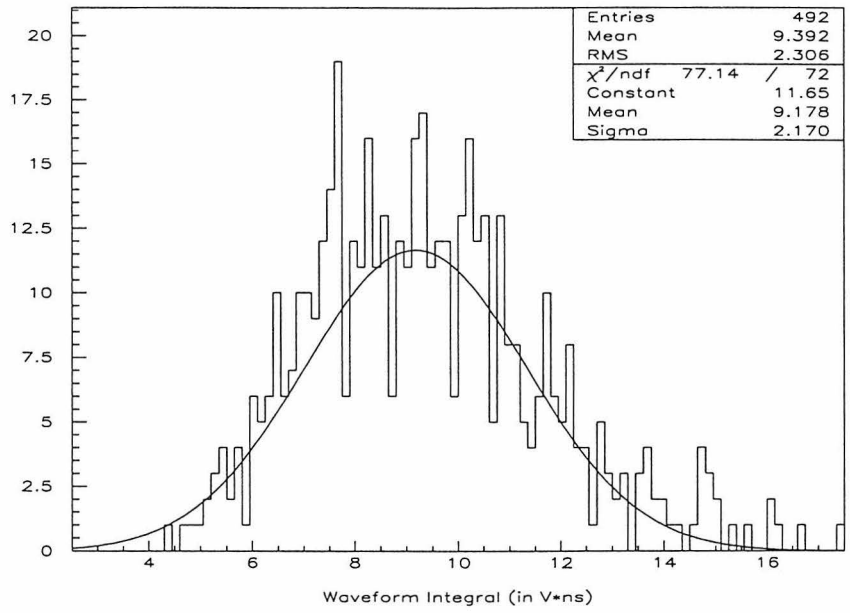

Figure 5.3: Amount of light as measured by the WFDs for a group of roughly 500 events that were simulating a $3.8\mu s$ long monopole-like pulse. A Gaussian fit of the distribution can also be seen.

given pulse width we calculate the $\beta = v/c$ of the simulated particle, assuming a pathlength of $19cm$ inside a scintillator box. In figure 5.4 we plot the SMT efficiency versus L/L_{min} for $D = 4.8\mu s$. As we can see, SMT remains highly (more than 90%) efficient over a wide range of ionization yields. The only appreciable variation in the sensitivity measurement that occurs at very low light levels ($< 0.5L_{min}$) is the result of some minor counter to counter PMT gain variations[6] and maybe some systematic error in the waveform integral calculation.

From plots similar to the one in 5.4, we graphically determine the light yield above which the slow monopole trigger circuit fires with probability greater than 90% for a slow moving particle of a given velocity. This is plotted in figure 5.7.

[6]The sensitivity measurement was performed on 16 different counters belonging to all 8 different faces of SM5 and SM6.

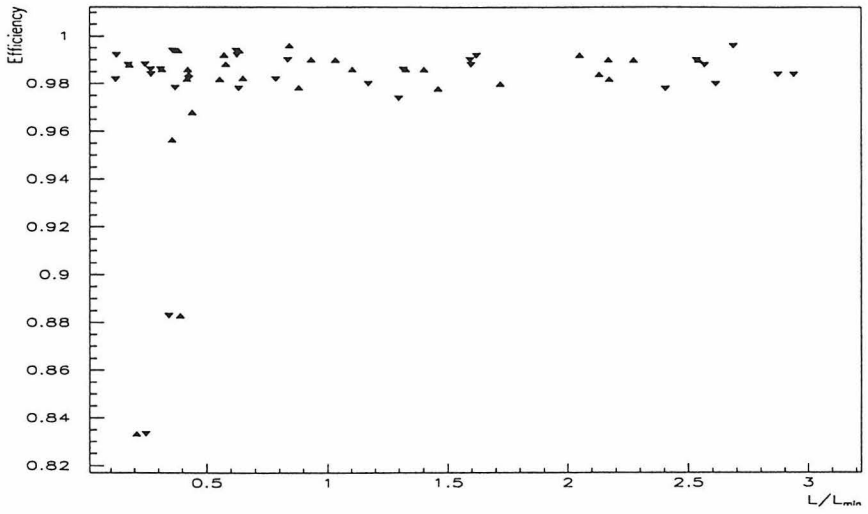

Figure 5.4: SMT trigger efficiency as a function of light yield (in units of the minimum ionizing yield) for $4.8\mu s$ long simulated pulse trains corresponding to particles of $\beta = 1.3 \times 10^{-4}$. Our efficiency measurements extend to several tens of L_{min} at which the SMT remains more than 95% efficient. Being conservative, for this β, we will consider that SMT becomes 90% efficient at $L/L_{min} = 0.4$.

5.2 Wavelet-based Slow Particle Identification

Given the monopole-like rich data sample that the LED calibrations have to offer, they constitute a perfect dataset both for training and studying the efficiency of any pattern recognition algorithm. During the LED ADC calibration runs, we keep a detailed record of every event; this allows us to know *a priori* which waveforms should depict a monopole-like pulse (i.e., in which channels the LED did fire) and which should be empty (background). By means of this information, we are able to label the recorded waveforms as monopole-like and monopole-less (i.e., flat baseline plus noise). We trivially identified these during a randomly selected calibration run (80562) and we Haar-decomposed all of them. Since the Haar transform is a dyadic decomposition, as a first approach, we used *only the first 256* out of the 320 samples that every waveform consists of. In figure 5.5 we plot the Haar features that we extracted from the Haar decomposition of the monopole-like (left column) and monopole-less (right column) waveforms. We can clearly see the differences among the two classes of

waveforms: monopole-less waveforms result in small global Haar maxima which have no preference of alignment among the consecutive resolution scales. The vast majority of their global maxima occur at the very first scales and they immediately "die" since the Haar transform smears out any of their variations as we follow down the Haar "ladder" (see figure 4.4). As a result, the energy content of the low scales is bigger than that of the high scales. On the other hand, the monopole-like waveforms result in global maxima that are found in the very last resolution scales and the energy content is strongly focused at the high scales (negative energy contrast). We can now see how the application of our "wide signal filter" (as defined in chapter 4) can select the vast majority of the monopole-like events while accepting a tiny fraction of the background. This background introduction is actually of no direct interest for this monopole search since the *presence of an SMT trigger will be a prerequisite before applying our Haar-based filter.* However, should any SMT trigger have resulted from noise and depicted featureless (background) waveform, the Haar-based filter would have effectively rejected it[7]. So far, we have Haar-decomposed only the first 256 out of the 320 samples of a waveform; in order to access the full waveform information of each channel we "slide" the 256-bucket wide window from the left-most position of the 320-bucket wide original waveform to the right-most, performing its Haar decomposition one more time. Apparently, if the monopole signal were in the last 64 buckets of the waveform window we would have never found it, had we processed only the first 256. The *logic or* of the Haar "wide signal filter" decision in each of the cases flags a waveform as a monopole candidate.

[7]This is where the Haar decomposition reveals itself as a powerful stand-alone trigger: we can imagine a piece of electronics performing the Haar transform of a signal coming from a digitizing machine and reaching a trigger decision based on the signal's Haar features.

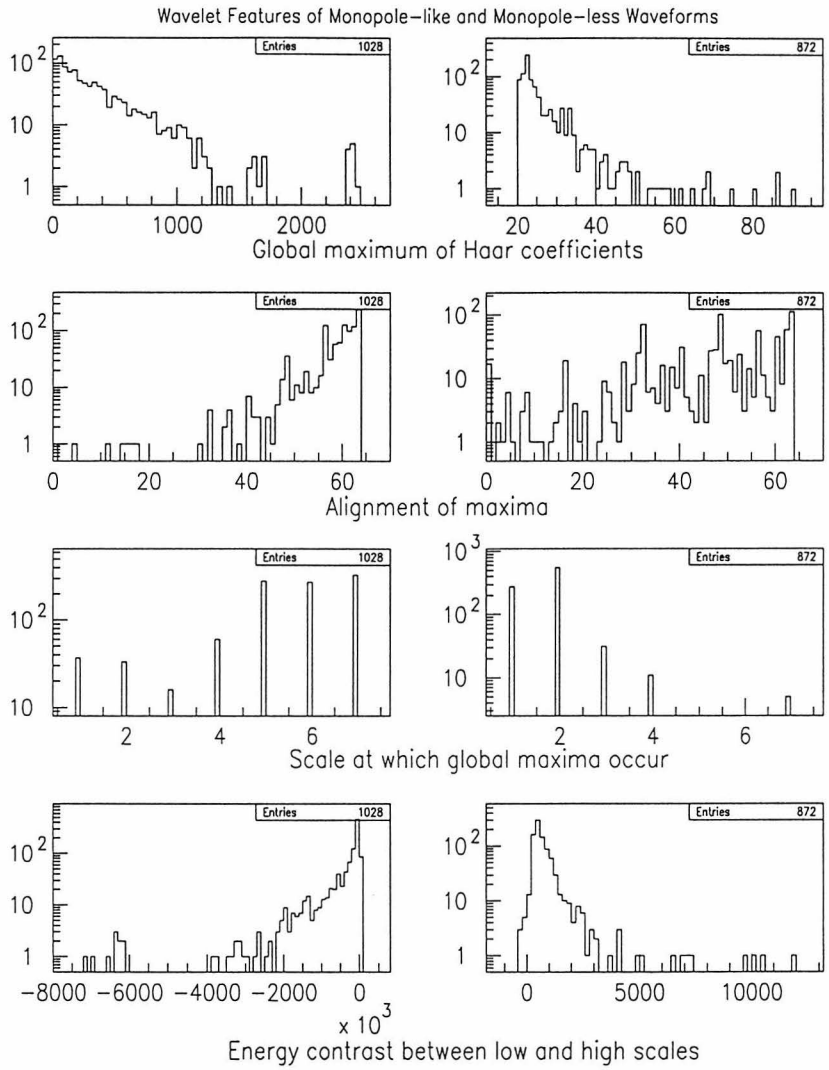

Figure 5.5: Features of the Haar decomposition of monopole-like (left column) and background (right column) waveforms. In each of these plots there is one entry per waveform. Only the first 256 buckets of a waveform channel have been processed and, for the background waveforms, a global Haar maximum greater than 20 is required (see chapter 4 for definition of terms used in this plot). The Haar wide-signal filter requirements of negative energy contrast and Haar focus above the second scale accept 937 out of the 1028 monopole-like waveforms. One may notice the different horizontal scales of the left and right columns in the top and bottom plots.

As we have seen in the previous section, by varying the width and height of the pulses driving the LEDs we were able to measure the sensitivity of the slow monopole trigger circuit; using the same points in the light yield versus velocity parameter space, we may trivially measure the *SMT plus Haar efficiency* just by checking which monopole-like waveforms pass the Haar wide signal criteria as described above. The SMT plus Haar efficiency from now on will be referred to as the *analysis* sensitivity. Similarly to figure 5.4, we can now plot the analysis sensitivity (defined as the ratio of events that had an SMT trigger *and* passed the Haar wide signal criteria to the number of events generated) versus L/L_{min} for any given D. This is shown in figure 5.6 for $D = 4.8\mu s$.

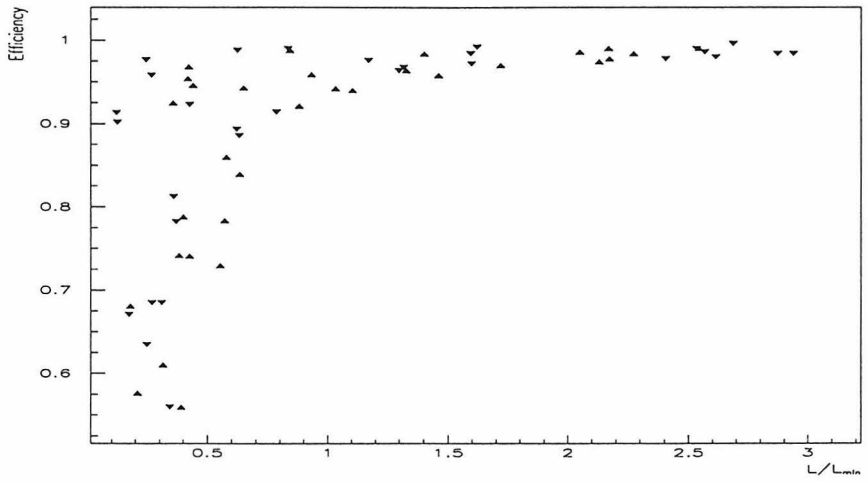

Figure 5.6: SMT plus Haar filter efficiency as a function of light yield (in units of the minimum ionizing yield) for $4.8\mu s$ long simulated pulse trains corresponding to particles of $\beta = 1.3 \times 10^{-4}$. The same dataset that was used to produce figure 5.4 is used also here. The requirement for the monopole-like waveforms to satisfy the Haar criteria results in loss of sensitivity at low light yield levels. This basically shows the limitations of the Haar-based pattern recognition method. For this β, we will consider the 90% sensitivity threshold at $L/L_{min} = 0.6$.

Performing similar measurements for various D (i.e., β), we obtain the dashed line of figure 5.7 which shows the required light yield as a function of velocity in order for our *analysis* to be 90% efficient.

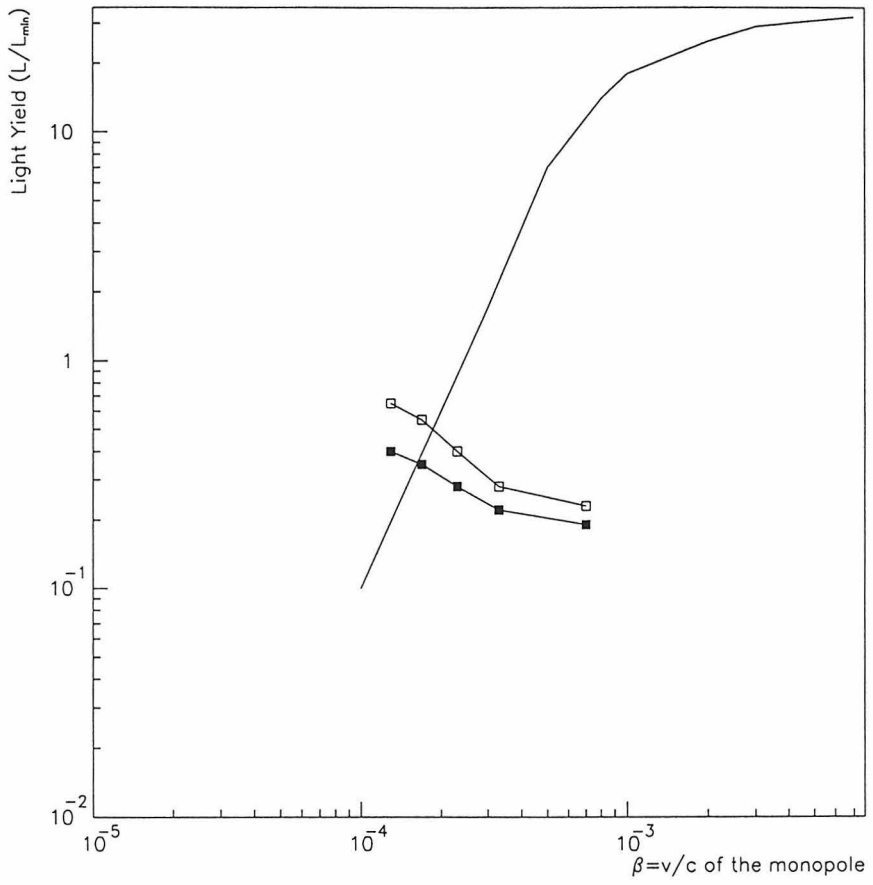

Figure 5.7: Slow Monopole Trigger and analysis sensitivity measurements. The stars define the SMT's sensitivity curve: for a particle of given β, the SMT becomes more than 90% efficient at light levels (in units of the minimum ionizing particle light yield) above the ones defined by the stars. The crosses define the 90% sensitivity curve for our analysis (SMT plus Haar). For comparison, the light yield of a magnetic monopole is also plotted.

Chapter 6

Analysis of Monopole Candidates

As we have described in chapter 3, our primary event selection yielded a total of 8219 *monopole coincidence events*. In this chapter, we are going to apply the wavelet ideas we have described in chapter 4 in order to make the final event selection which will yield our *monopole candidate events*. The waveforms of the candidate events will eventually be scanned visually in order to make the final decision.

6.1 Slow Monopole Candidate Selection Using Haar Filters

The waveforms of all the detector faces that were involved in a monopole coincidence event were fed into our wavelet algorithm. This involved the Haar decomposition of a minimum[1] of 4 different waveforms (2 tank-ends for a minimum of 2 faces) which were checked to see if they satisfied the Haar criteria[2]. As we have shown in chapter 5, our Haar filter can effectively suppress isolated radioactivities and cosmic ray muons while efficiently selecting pulses that have wide structure; thus the requirement that these criteria be satisfied on a (tank) end-to-end, face-to-face basis arises rather naturally. In this way, the application of the Haar filter reduces the number of events to 1261. In figure 6.1a we plot the event number versus the run number for each of the events that survived. As we can see in this plot, there are still few runs with high event density; however, in order to pursue a monopole search that is as much open-minded as possible, we will accept *all the events* that passed the Haar criteria.

[1] Notice that since we *do not* impose any cut on the maximum number of faces involved in a monopole coincidence event, the maximum number of waveform channels that can be involved in a single event is 48, the total number of waveform channels in MACRO.

[2] From now on, when we make mention to the Haar criteria/filter we will imply the Haar *wide signal filter*.

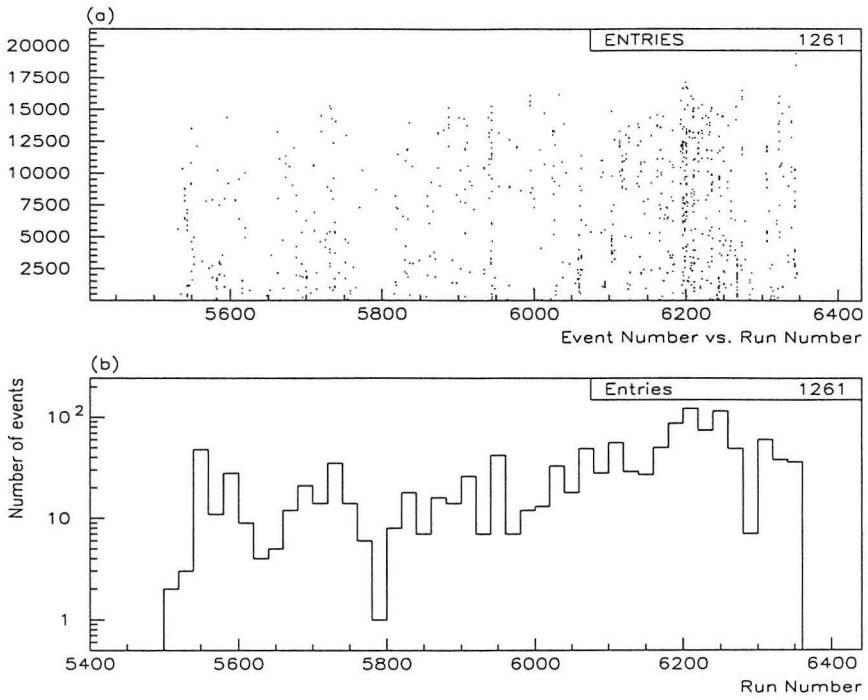

Figure 6.1: Monopole coincidence events that passed the Haar criteria. These constitute our monopole candidate events. Every event is identified by its run and event numbers. A scatter plot of these pairs for all the monopole candidate events is depicted in figure (a). This is essentially a time distribution plot: the run number axis reflects the elapsed time since the beginning of data-taking and the event number axis reflects the time elapsed since the beginning of any given run. In the bottom figure (b), we see the projection of figure (a) onto the run number axis. Notice that Runs with numbers greater than 80000 have been renumbered starting from 5500.

6.2 Visual Scanning of Candidates

For the 1261 events that satisfied the Haar criteria we visually scanned all of their waveforms. Based on our observations, we classified these into four groups:

- muon-related events, 202 in total
- calibration-related events, 81 in total
- noise-related events, 977 in total
- radioactivity events, 1 in total

6.2.1 Muon-related events

The first group of monopole candidate events includes these which occurred upon the passage of a muon through our detector. As we have seen in chapter 2, MACRO offers high redundancy in recording cosmic ray muons when crossing it: two independent scintillator-based muon systems offer the trigger decision while two independent ADC/TDC systems (one of which is the LeCroy Waveform Digitizers (WFDs)) perform time and energy measurements. On top of that, the streamer tube system provides high resolution tracking allowing us to localize muons in space. In our analysis, in dealing with these events, we have used *primarily* the ADC/TDC information that the monopole system itself has to offer. However, for demonstration purposes only, we will occasionally present in parallel both the information obtained from the monopole system itself and the information obtained from the streamer tubes and/or the dedicated scintillator-based muon triggers.

Starting with these muon-related events, we may first identify those where the *CSPAM muon trigger failed* to fire and as a result the CSPAM trigger software cut could not eliminate them. The failure of the CSPAM trigger to fire may be attributed in most of these events to obvious trigger hardware problems that resulted in the CSPAM being dead in one or more of its channels for a short or extended period of time. For example, in figures 6.2a,b we plot the CSPAM trigger rate for the supercounters 4E-L0 and 4E-L1 as a function of run number. One can clearly see supercounter 4E-L0 "disappearing" around run 5810 and then "reappearing" around run 5845; this was the result of an unplugged cable that remained unnoticed for several runs until it was finally repositioned.

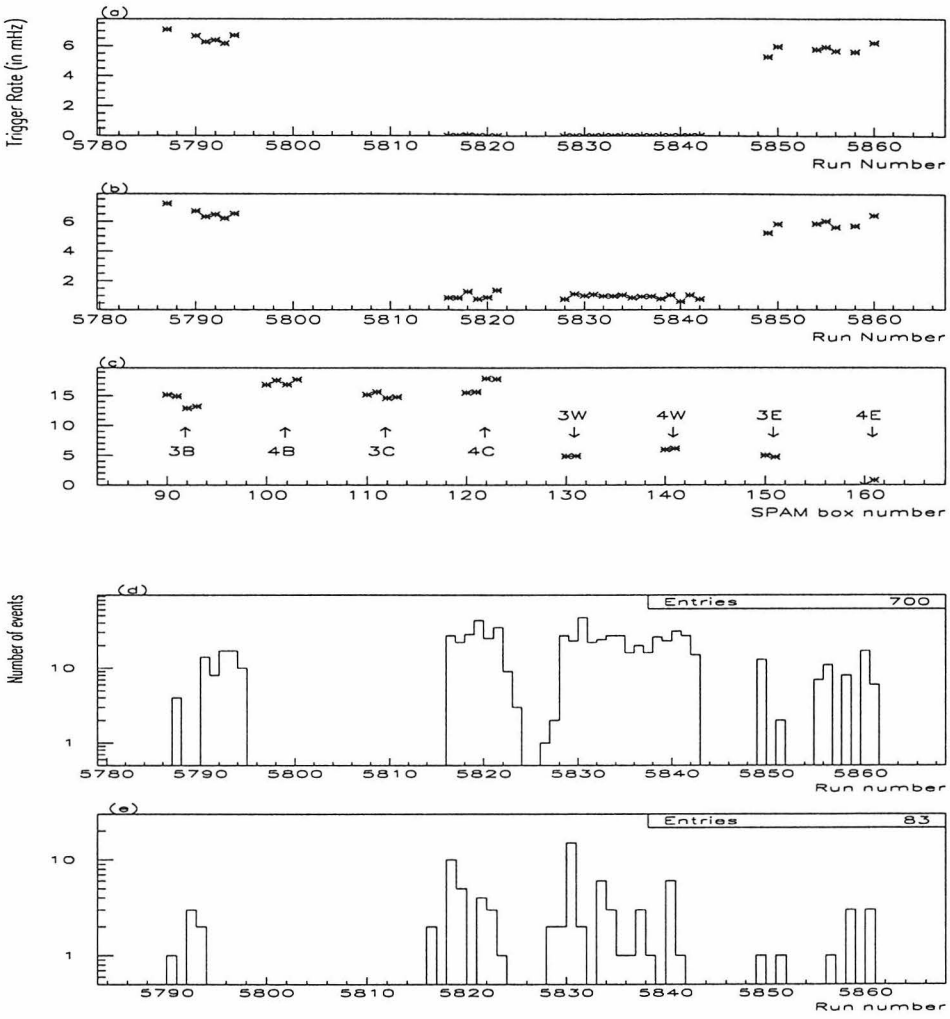

Figure 6.2: CSPAM trigger rate for supercounters 4E-L0 (a) and 4E-L1 (b). In doing these plots we have selected runs that lasted at least 100 minutes; this leads to the missing entries for some runs. In figure (c) we plot the CSPAM trigger rate for every supercounter in μVax 2 during run 5828. Note the almost zero rate for 4E. Run 5828 was randomly selected among the runs during which the CSPAM was suffering from hardware problems. (d) Number of monopole coincidence events vs run number. One may notice the anticorrelation between CSPAM rates and number of monopole coincidence events. (e) Number of monopole candidate events for the same period of running. The application of the Haar filter has eliminated most of the muon-related events.

Over the same period of time, as we can see in figure 6.2d, the number of monopole coincidence events had a dramatic increase simply because of all the muons that managed to fire the Slow Monopole Trigger (SMT) but failed to be vetoed by the CSPAM software cut. Our wavelet analysis tools offer significant help in rejecting the *vast majority* of these events. Since most of them are coming from muons crossing our detector, they fail to satisfy our Haar filter and they are thus eliminated. Nonetheless, for that period of running, there are 83 events (figure 6.2e) that did satisfy the Haar criteria. One may ask how these events –if typical muons– fulfilled the Haar criteria.

As it turns out, the muon-related events that pass the wavelet criteria do *not* have typical muon waveforms. Most of them result from electromagnetic showers and multi-muons in which the energy deposited in the scintillator counters is significantly higher than that of a minimum ionizing muon[3]. As a result, the PMTs saturate in most of these cases and the apparent width of the pulse that is recorded by the WFDs is increased. Of course, it is true that in showers and multi-muons there are many particles involved which hit our detector at different times, of the order of tens of nanoseconds apart. However, this can not explain the pulse widths of hundreds of nanoseconds that we observe. Unfortunately, the present multiplexing of waveform channels (16 PMT signals for every WFD channel in the case of horizontals and 7 PMT signals for every WFD channel in the case of verticals) does not allow us to study in detail the response of *each* PMT *individually* to such events. Recording the analog sum of PMT signals coming from an SM's face results in observing many signals on top of each other, including not only the primary PMT pulses but also their afterpulses. PMT afterpulsing occurring at different times for different PMTs that are fanned into the same WFD channel makes another contribution to the "fattening" of the observed waveforms.

In order to obtain an overall –although quantitative– picture of the nature of these events and of the functionality of the Haar filter, we have constructed simple waveform processing routines in order to determine various pulse characteristics of the

[3]The energy measurement with ERP yields 35 MeV as the most probable amount of energy deposited in a scintillator counter by a muon. In the case of multi-muons and showers, we have observed events where several hundred MeV of energy is deposited in the counters.

recorded waveforms. Quantities like the maximum pulse height, the waveform integral (charge) and the pulse width at various discriminator levels were among these that we have calculated. We selected waveform channels where both the ERP muon trigger and the SMT had at least one hit coming from the same scintillator box and, in addition, we required the maximum pulse height of the recorded waveform to be at least 100mV. In figure 6.3 we first plot the total number of scintillator boxes (within a face) that gave an ERP muon trigger during an event. The unhatched histograms correspond to the monopole coincidence events while the hatched ones correspond to the monopole candidate events, i.e., the coincidence events that satisfied the Haar criteria on a (tank) end-to-end, face-to-face basis. In the first plot, a clear peak appears at 1, mainly corresponding to single muons which manage to fire the SMT and escape from the CSPAM, while the tail reaches up to 16 (the maximum number of scintillator boxes in a detector face). The events outside the peak correspond mainly to showering and multi-muon events that naturally spread over a wide area when hitting our detector. Having very narrow waveforms (around 55ns at half maximum, see figure 6.3b), the vast majority of single muons fail to pass the Haar filter and the only ones that "escape" into the candidate dataset are these with waveforms where the Haar algorithm detected a monopole-like signal at a WFD bucket location *other than* the one where the muon occurred. On the other hand, "fat" (Full Width at Half Maximum FWHM$> 200ns$) pulses are efficiently identified by the Haar filter; the only ones that are thrown away are these which fail to fulfill the end-to-end and/or the face-to-face requirement.

In the bottom figure of 6.3 we plot the total energy (in MeV) that was deposited in a scintillator *face*. In order to obtain this number, we added the ERP reconstructed energies for each of the individual boxes of the face that gave a muon trigger.

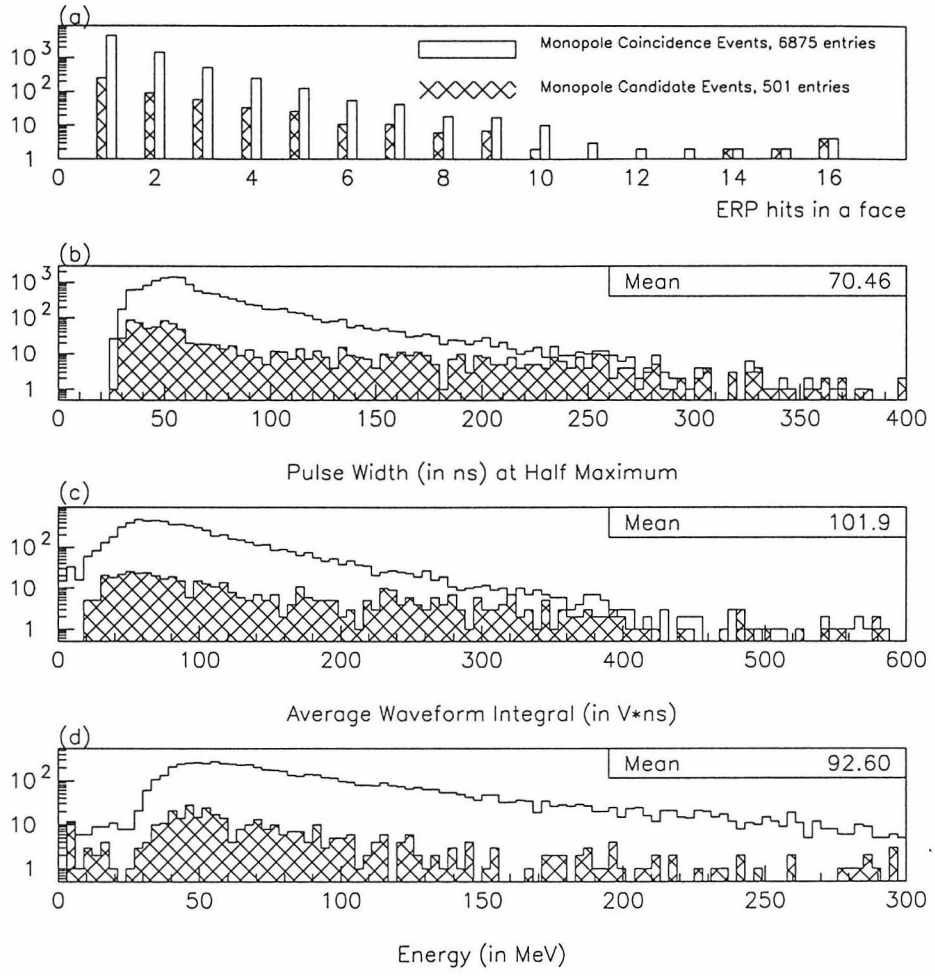

Figure 6.3: Muons that fired the SMT: for the monopole coincidence and candidate events that were accompanied by an ERP muon trigger, we plot in (a) the total number of ERP boxes in the face that fired, in (b) the pulse width at half maximum, in (c) the integral of the waveform (charge) averaged between the two ends of the tanks and in (d) the ERP reconstructed energy summed over all the boxes that gave a muon trigger within a detector face. The peaks of *all* these distributions are mostly (roughly 95%) populated by single muons that manage to fire the SMT and fail to be vetoed by the CSPAM. The mean value that is printed on each of the plots represents the mean of the monopole coincidence events distribution. See text for detailed discussion.

As in all the other plots of figure 6.3, the peak of the distribution is populated mainly by muons that hit 1 or 2 scintillator boxes in a face; with their energies peaked at roughly 50 MeV, one may notice that muons that fire the SMT are significantly *more energetic* and *"fatter"* than the average muons that arrive in MACRO[4].

A typical representative of the kind of event that falls under this category is shown in figure 6.4. Here we show MACRO's event display depicting a muon shower hitting the center face of SM5 and exiting from its west[5] face. The CSPAM muon trigger failed to fire on this event but our Haar algorithm picked it up due to the significant width of its waveforms. Actually, the waveform corresponding to the center face of SM5 (see figure 6.5) for this event is one of the most spectacular among these collected during the six-month run data showing the effects of waveform "fattening" we have been talking about. As for most of the muon-related events, for this one too, using the waveform and latching scaler timing information we may reconstruct the muon's time-of-flight (TOF) to be essentially zero within 100 ns accuracy[6]. Indeed, if T_C and T_W are the times at which the events occurred at the two faces of the detector, then we may write

$$TOF = T_W - T_C = (T_W - T_C)^{stop} + (T_W - T_C)^{wfd}, \tag{6.1}$$

where $(T_W - T_C)^{wfd}$ is the apparent time difference between the start of the two waveforms and $(T_W - T_C)^{stop}$ is the time difference between the WFD STOP signals as measured by the latching scaler. For the event shown in figure 6.5, (figure 6.6 is a zoom down of 6.5 into the time interval where the events occurred) we may determine by eye:

$$(T_W - T_C)^{wfd} \approx -750ns, \tag{6.2}$$

[4]The most probable energy deposition for muons in a single counter is ~35MeV, while the most probable FWHM of the resulted PMT pulse is ~50ns.

[5]East and West faces can not be discriminated in the kind of plot like 6.4. However, MACRO's event display offers separate "views" of the vertical faces which allow us to see which of the two vertical faces have hits.

[6]The accuracy is determined primarily by the clock of the latching scaler which is 10MHz.

while the latching scaler recorded

$$(T_W - T_C)^{stop} = 700ns, \tag{6.3}$$

and so, substituting in equation 6.1 yields $T_W - T_C \approx -50ns$ which falls within $100ns$ of the expected TOF of approximately $50ns$. A better estimate of the TOF may be obtained from the ERP information for the same event. Indeed, if ${T_W}^{ERP}$ and ${T_C}^{ERP}$ are the ERP reconstructed times averaged over all the scintillator boxes of the corresponding faces, then we may easily find

$${T_W}^{ERP} - {T_C}^{ERP} = (-363.1)ns - (-399.6)ns = 36.5ns. \tag{6.4}$$

As with this typical example we have just worked out, pulse shape and timing arguments reject the muon-related events where the CSPAM trigger failed to fire.

Another kind of muon-related events are those which resulted from us being *open-minded* on handling events which were accompanied by the CSPAM muon trigger. As we have explained in chapter 3, before vetoing an event due to the presence of a CSPAM muon trigger, we checked that *every* box giving an SMT trigger had also a corresponding latch in the CSPAM hit registers. Similarly to the events in which CSPAM was inefficient, these events are also through-going muons that managed to fire the SMT. The extra hit[7] that is present in the SMT is due to (a) muons belonging to multi-muon bundles which triggered SMT but not CSPAM, or (b) radioactivities, or (c) just noise which managed to fire SMT and did not trigger CSPAM (as expected).

Finally, in the same group of muon-related events are those which depict muon waveforms in one of the detector faces and noise and/or radioactivities in the other(s). For most of these events, we believe that these "radioactivities" belong to the sequence of afterpulses that follow the big PMT pulses that result when energetic muons (including multi-muons and muon showers) hit MACRO. This can be seen in figure 6.7 which shows the waveforms from an event of this type. A muon shower hit the 4E

[7]On some occasions the SMT registered more than one hit in excess of the ones that had a corresponding CSPAM latch.

face of MACRO and the WFDs recorded the "fat" pulses shown in channels 4E-0 and 4E-1, which –as we have seen– are typical of muon showers. Upon exit from face 4B of MACRO, the SMT fired on the afterpulses that followed the main PMT pulse and this is what we see in channels 4B-0 and 4B-1. One may notice that the left end of 4B has barely missed the main PMT pulse coming from the muon; this is a limitation due to the maximum time window that the LeCroy WFDs can record.

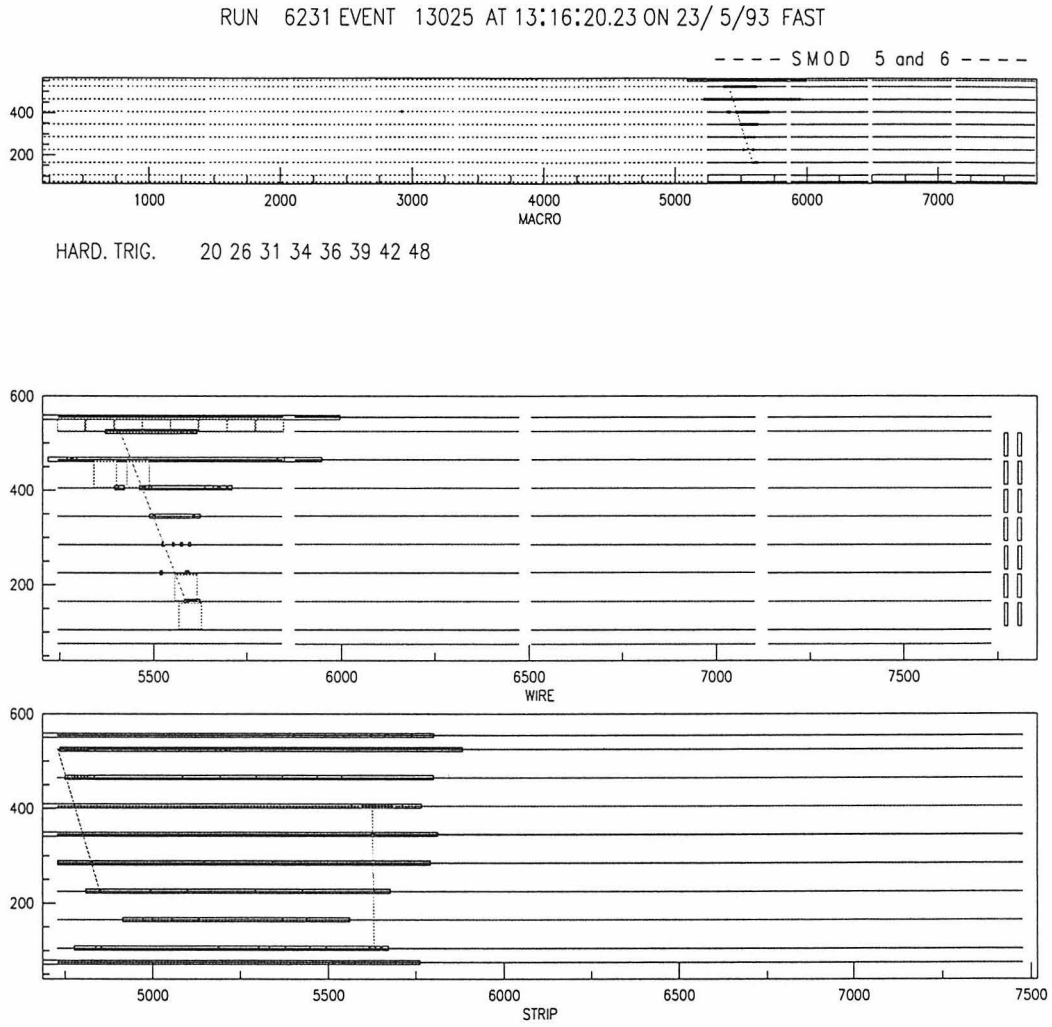

Figure 6.4: MACRO's Event Display during RUN 6231, EVENT 13025. The top figure shows the full detector picture while the bottom two figures depict the streamer tube wire and strip views. The (green) boxes indicate the horizontal and vertical scintillator boxes where the ERP muon trigger fired. The dotted lines show the tracks reconstructed by the tracking algorithm.

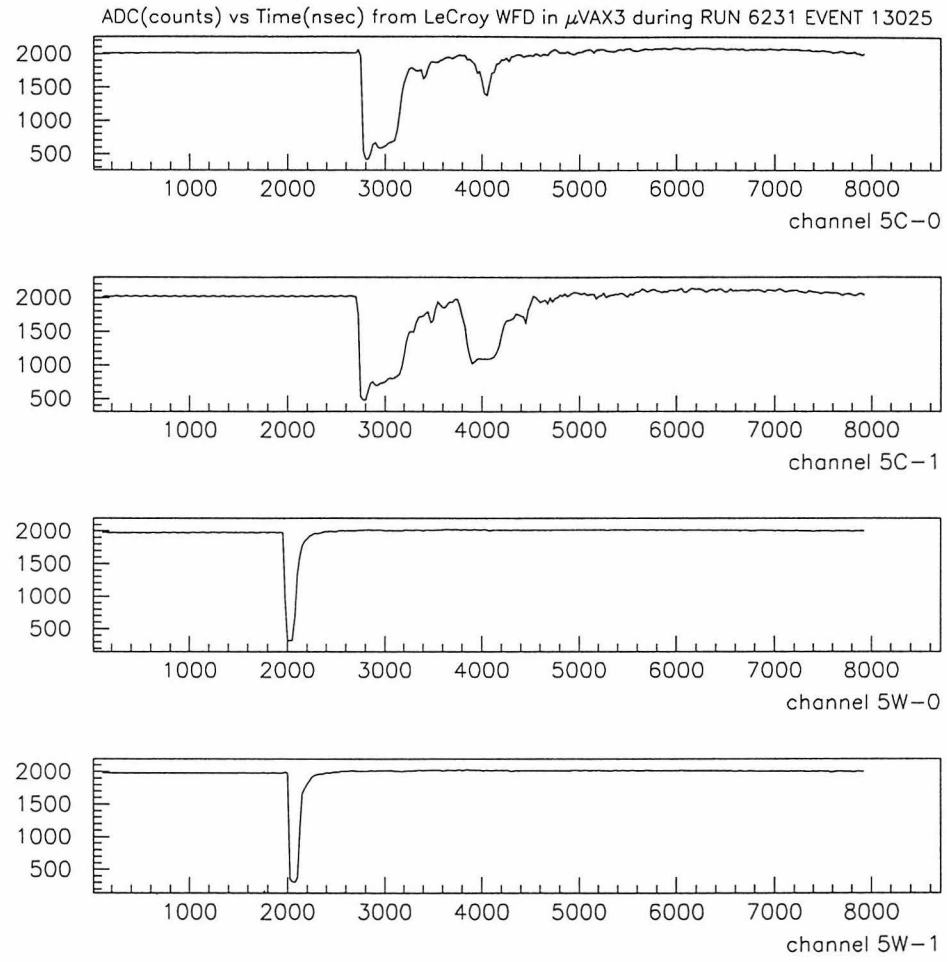

Figure 6.5: LeCroy WFD data for channels 5C and 5W. The horizontal axis is the time in nanoseconds while the vertical is the pulse height in mV. The plotted waveforms seem as if they did not reach the maximum count; this is because our waveform plotting software rescales the waveform data to a pedestal of 2000 counts.

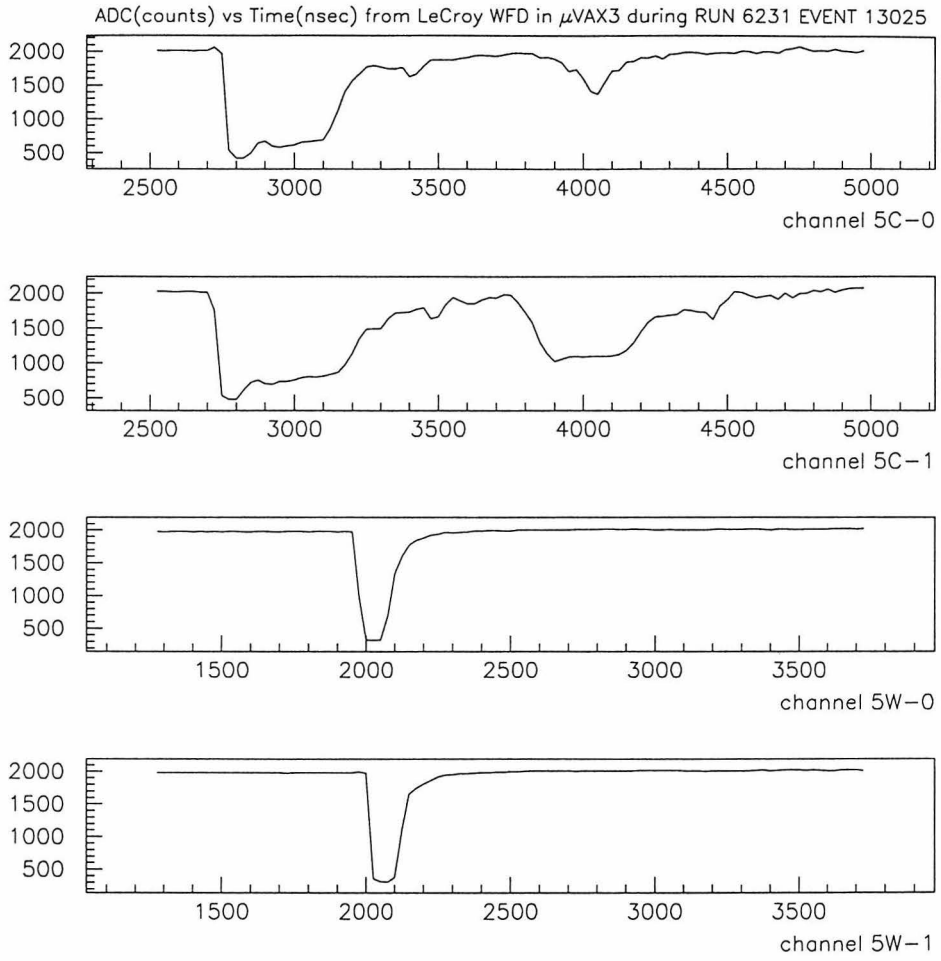

Figure 6.6: Zoom into the time domain of the LeCroy WFD data for channels 5C and 5W. See caption of figure 6.5 for details.

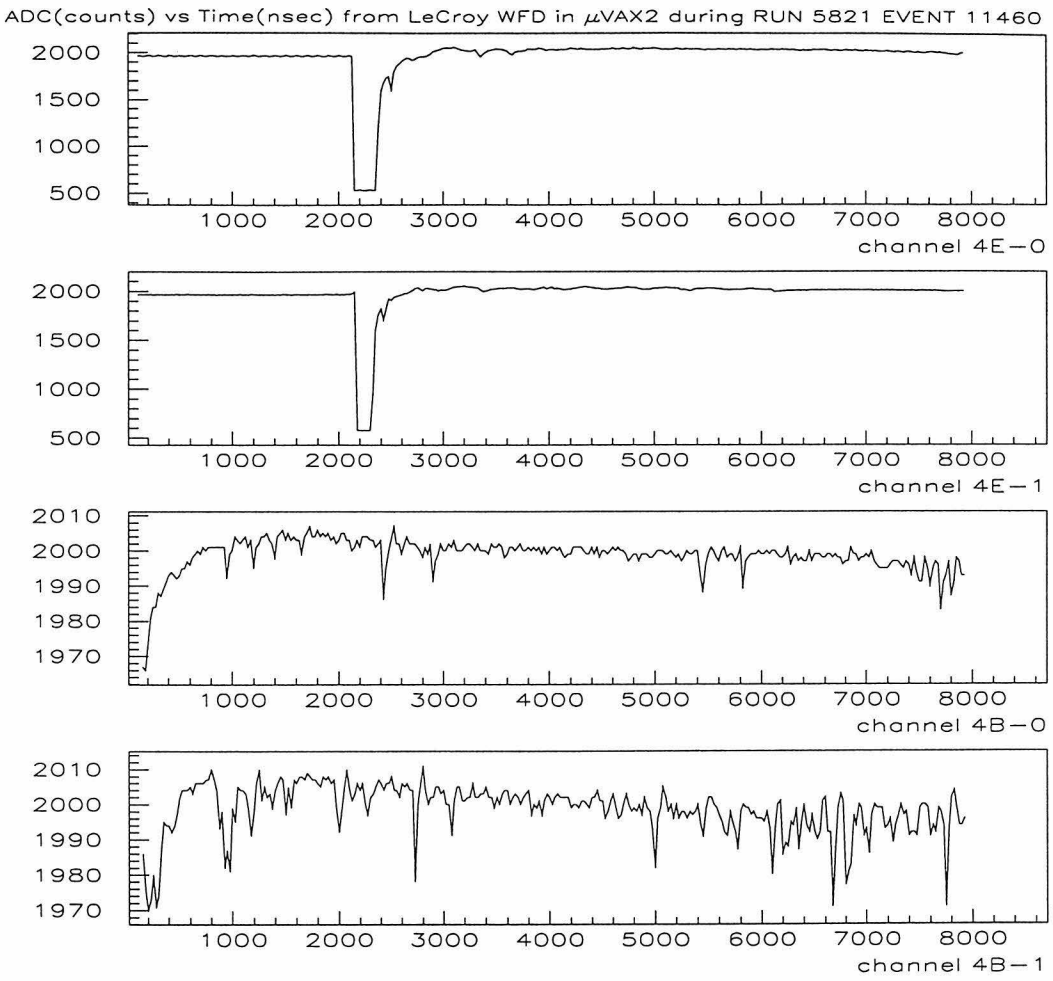

Figure 6.7: Muon shower hitting MACRO; a "fat" muon pulse is recorded in the "entrance" channels (4E) and the sequence of PMT afterpulses is shown in the "exit" channels (4B). See text for discussion.

6.2.2 Calibration-related events

The second group of monopole candidate events includes those with waveforms that depict pulses which were *not* produced by the scintillation light of an ionizing particle that went through our detector's scintillator tanks; instead, these events are related to the calibration system hardware. The question that naturally arises is what can cause such pulses.

As we have described in chapter 2, two independent calibration systems, namely the Laser and LED, that may produce artificial light, are implemented throughout our whole detector. Although during MACRO's six-month run we made reasonable effort to guard ourselves against Laser and/or LED pulses from "escaping" into the data stream during normal runs, accidental firing of either one of them resulted in some events of this type. For the laser-induced events, the simultaneous presence of "fat" waveforms in all the waveform channels rejects any hypothesis that they result from the passage of a particle(s) through MACRO. The absence of any streamer tube information and/or the ERP reconstructed position occurring at the center of the tank, where the laser fibers live, supports further the laser-induced hypothesis. Most of the LED induced events occurred while part of the detector was being calibrated and part of it was taking normal data. The LED calibrations in MACRO involve camac controlled operations of programmable pulsers which fire LEDs placed close to each of the PMTs. Cross-talk on the camac controlled LED switchboxes resulted in firing the wrong LEDs or even keeping some of them on beyond the end of the calibration procedure. The latter resulted in LED induced events "escaping" into the normal datastream even when the full detector was in acquisition. There is a common pattern for all these LED induced events: they occur between the detector's vertical (east and west) faces, when the LED in one end of the tank fires. The PMT close to the LED that fires usually saturates while the opposite one "sees" part of the emitted light. The observed pulse width is of the order of 500ns (at the base) and assuming a pathlength of 20cm this implies a β of the order of 1.3×10^{-3}. On the other hand, the measured TOF between the faces involved (east and west) is in general much bigger

than what is expected for a particle with that β traveling between the east and west faces of the detector. This makes invalid any hypothesis that these waveforms were registered upon the passage of a real particle through MACRO. Figure 6.10 shows one of this kind of event that occurred during a run when the *full detector* was in acquisition. One may notice the difference in pulse amplitude between the two ends of the tanks; this is because the "0" end of the east and west face LED(s) fired and saturated the corresponding PMT, while the "1" end PMTs saw the LED light that was attenuated after traveling through the full length of the MACRO scintillator tanks. For the same event, we can see that there are very few streamer tube hits present in the MACRO event display that is shown in figure 6.9.

Another kind of calibration-related pulse that was recorded by the WFDs includes those that were produced by the calibrations' "fake box" discriminator. Without getting into the details of the calibration system [68], we will try to explain how this may happen. For timing calibration purposes, four PMT fanout channels in each of MACRO's supermodules (SM) are labeled as "fake" and are driven (instead of by four PMT signals coming from two scintillator boxes) by a discriminator which is nominally set whenever the Laser and/or the LEDs are being fired. However, due to the multiplexing scheme of the WFDs, these discriminator-generated NIM pulses were fed (via the PMT fanouts) into the CSPAM logic and consequently into the WFDs. This mistake in our calibration system setup was left unnoticed during the first 2.5 months of running and this is where all these events came from[8]. During this period, when *electronic noise* was present in the detector, it occasionally succeeded in triggering this discriminator and had these pulses registered in the WFDs. The vast majority of these events have noise present in every WFD channel and the fake pulse is present in the *east* face. This is because in every SM, one of the calibration "fake boxes" is fed into the PMT fanout that is handling the SM's east face. The kind of pulse that is recorded in this face is shown in figure 6.12. Coming from the same discriminator channel, both ends of the same WFD channel have roughly *identical waveforms* (in pulse shape, width and height). As we can see in the same figure,

[8]This problem was eventually fixed and this kind of pulses stopped being recorded by the WFDs.

the fake pulse is in simultaneity with the glitches (noise) that are present in the rest of the WFD channels in this μVax, thus making impossible any suggestion of them corresponding to a real particle(s) going through our detector. During these events, noise was present also at the streamer tubes as depicted in figure 6.11, indicating that the whole detector was suffering from noise.

For each of the 81 events which we characterized as calibration-related, we plot in figure 6.8 the solar time in hours (after midnight) at which they occurred. As we can see, the vast majority of them occurred during the typical hours of human presence and activity on the detector; for example, the right-most peak in figure 6.8 resulted from some calibration-related events (identical to these shown in figure 6.10) occurring during run 5547. During this run, MACRO was collecting data in μVax 2 and 3 while calibration data (LED monopole-like simulation run 80368) was being collected in μVax 1. In the same plot, the left-most peak comes from calibration-related events which occurred around 2:00 a.m. during run 5616 and is due to the spontaneous firing of the Laser[9] in SM 5.

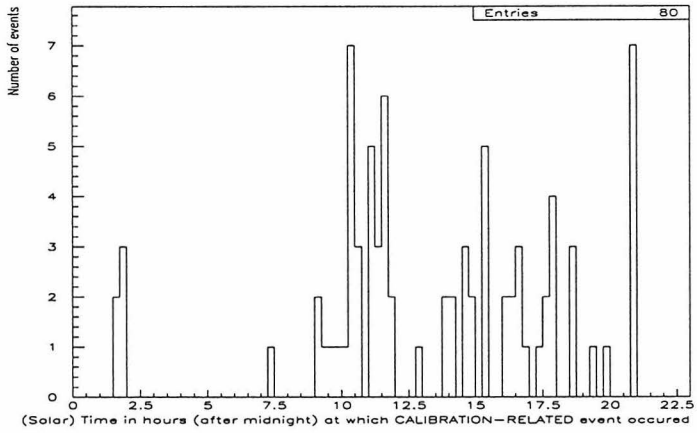

Figure 6.8: Time (in hours) at which calibration-related events were registered by MACRO. This indicates their correlation with the human presence and activity in MACRO. See text for discussion.

[9]This is actually the only case of a calibration-related event registered during non-typical working hours. A power glitch was the most probable cause of that spontaneous Laser firing.

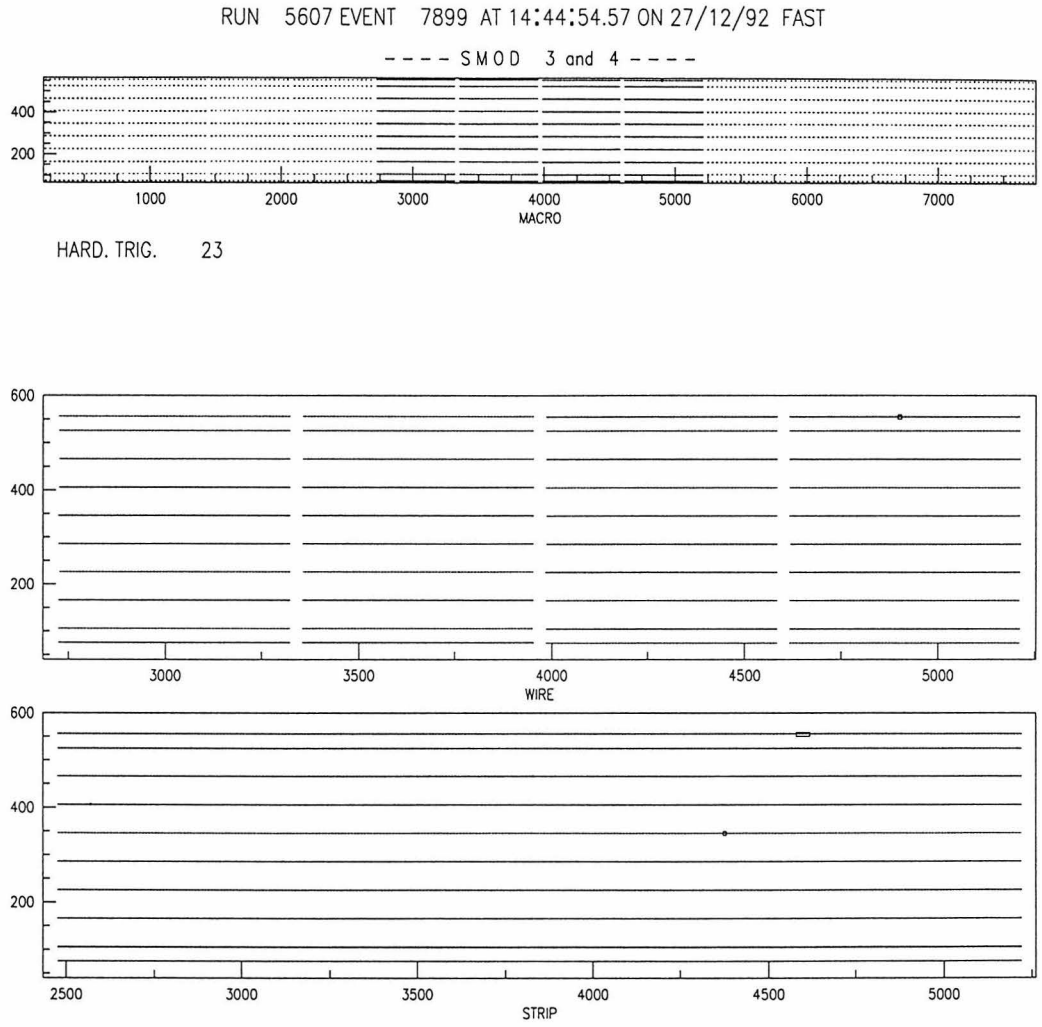

Figure 6.9: MACRO's Event Display during RUN 5607, EVENT 7899. The top figure shows the full detector picture while the bottom two depict the streamer tube wire and strip views. One may notice the very few accidental streamer tube hits that are present.

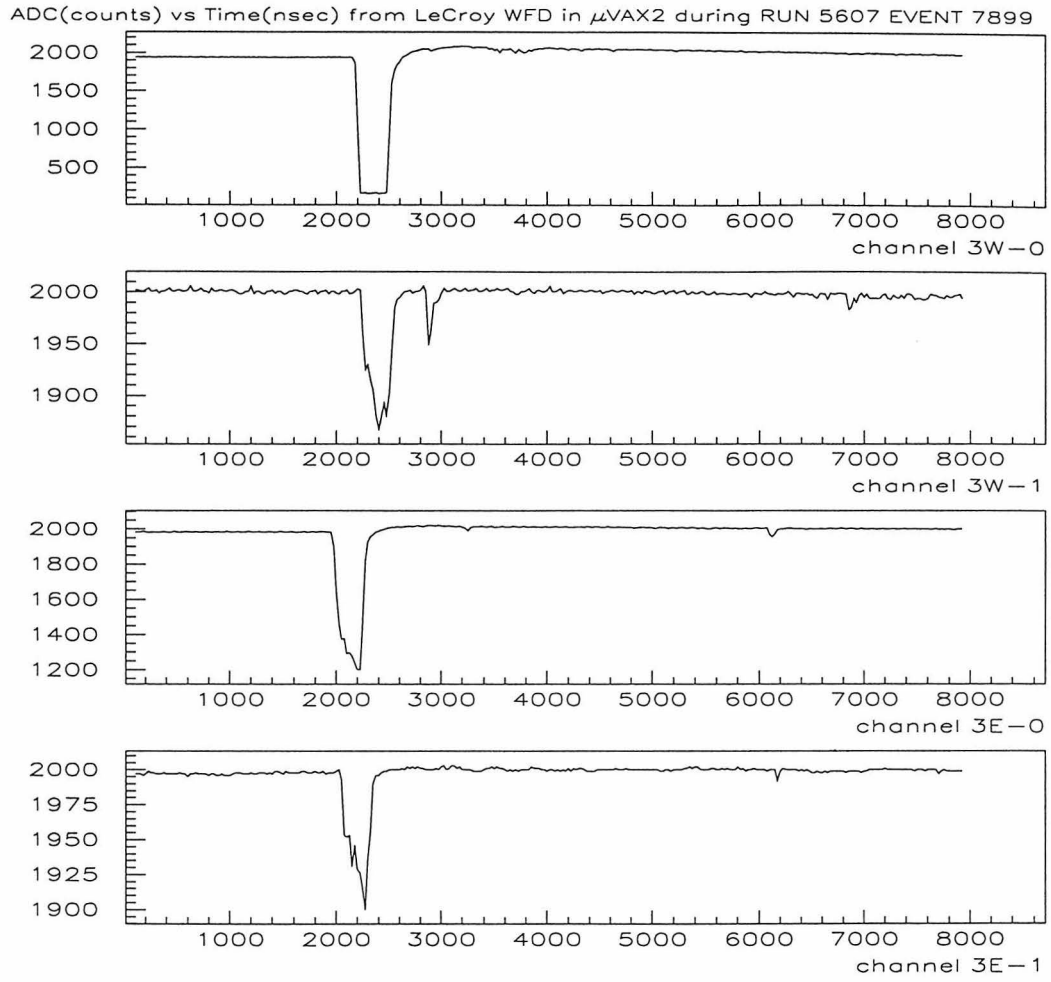

Figure 6.10: LeCroy WFD data for channels 3E and 3W during RUN 5607, event 7899. The horizontal axis is the time in nanoseconds while the vertical is the pulse height in mV (notice the different vertical scales). This is an LED-induced event that occurred while the full detector was in acquisition. The recorded TOF between the two faces was 462μsec, significantly more than the TOF expected for a real particle traveling from the east to the west face (a minimum distance of $12m$) and leaving a 400nsec wide pulse while traversing each one of them (nominally $20cm$ of pathlength). As in figure 6.5, our waveform plotting software has rescaled the waveform data to a pedestal of 2000 counts; this is why the "0" end waveforms seem as if they were not saturated.

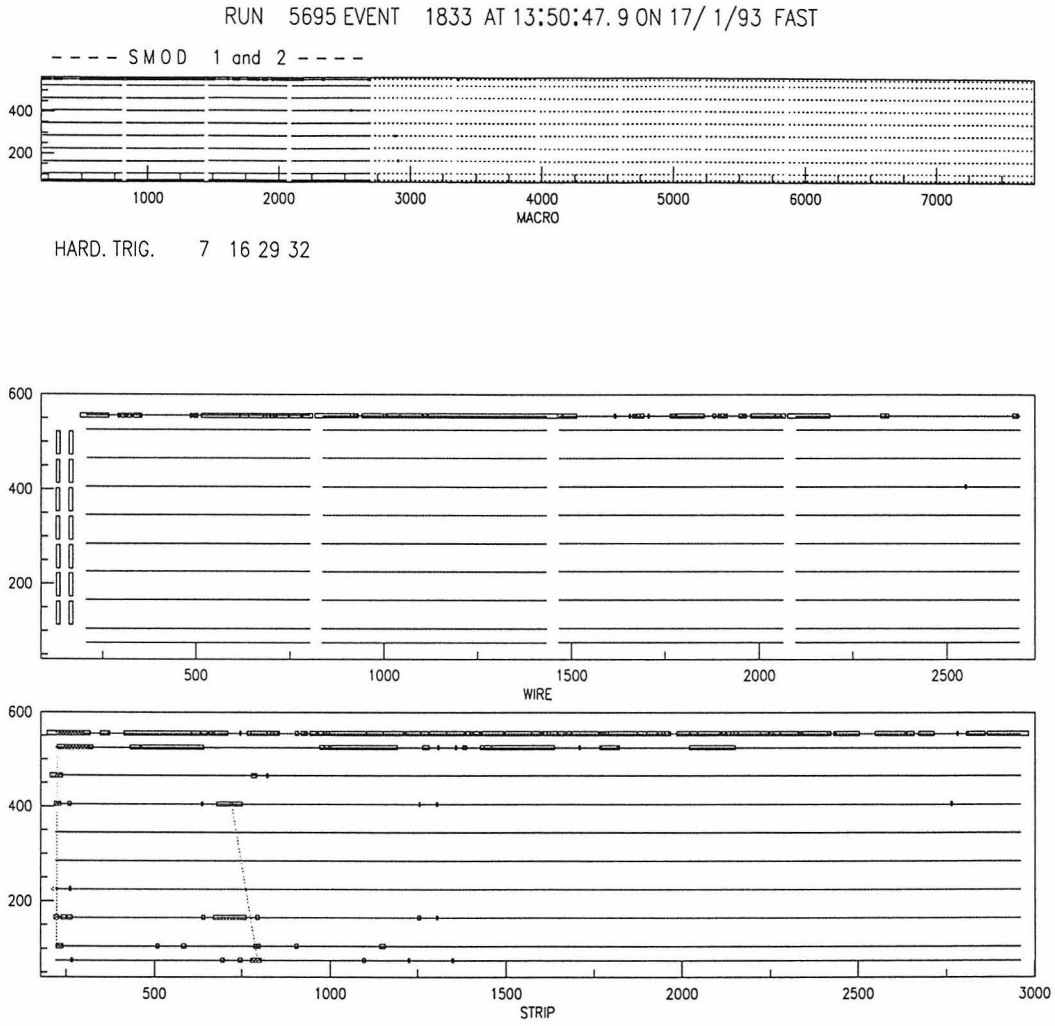

Figure 6.11: MACRO's Event Display during RUN 5695, EVENT 1833. The top figure shows the full detector picture while the bottom two depict the streamer tube wire and strip views. One may notice the streamer tube noise present in the center layer of SM 1 and 2. Almost certainly, this noise and the one recorded by the WFDs (see next figure) is of the same origin.

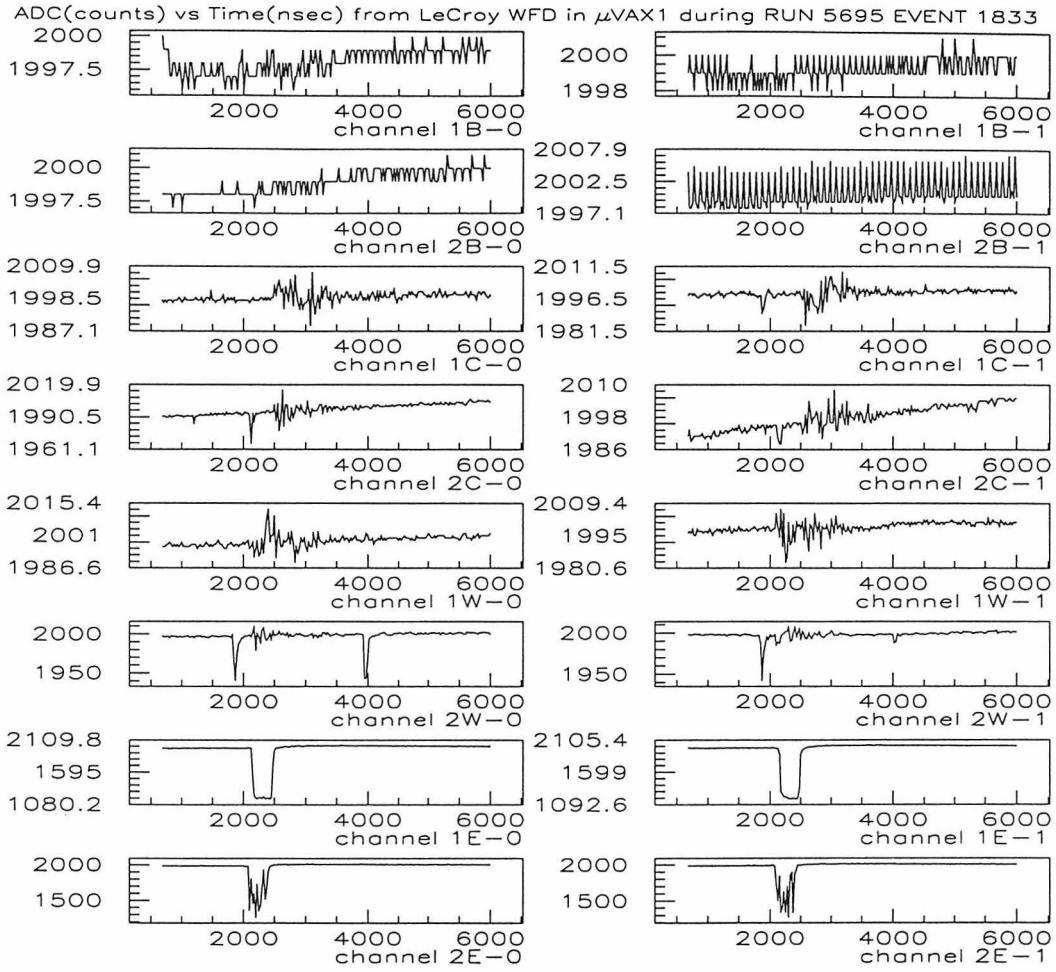

Figure 6.12: LeCroy WFD data for all the channels in μVax 1. The horizontal axis is the time in nanoseconds while the vertical is the pulse height in mV. The fake pulses present in channels 1E and 2E come from the discriminator that drives the "fake box." Notice that these pulses are in simultaneity with the glitches that are present in the rest of the WFD channels.

6.2.3 Noise-related events

This group represents the vast majority of the monopole coincidence events. Electrical noise is an inevitable guest in a detector of the size and complexity of MACRO. For most other physics analyses though, this noise remains transparent, basically because the signal that we want to detect is significantly above the ambient noise levels. This is *not* the case with the slow monopole trigger which is designed to detect signals at the level of a few mV; this is what makes it especially susceptible to noise. In the MACRO environment, possible sources of noise include the power distribution lines and radio-frequency pick-up. A great variety of heavy equipment[10] had to be operated while MACRO was taking data; these cases commonly resulted in bursts of noisy events. In general, as with the calibration-related events, there is a strong correlation between the noise events and the human presence and activity in the immediate vicinity of MACRO. In figure 6.13 we plot the (solar) time in hours after midnight of all the noise events that occurred during the six-month run. With only few exceptions, all of them occurred during the typical hours of human activity in the experimental hall.

In roughly 80% of the noise-related events, the TOF measured by the latching scaler was less than 1 μsec; also in more than 80% of the noise-related events *all* detector faces within a μVax had an SMT trigger. Most of them were also accompanied by noise in the streamer tubes, indicating that noise was widely present in the experimental hall.

The waveforms of the vast majority of noise-related events depict slow ($< 1MHz$) or fast ($> 1MHz$) bipolar oscillations present in most of the WFD channels of a μVax. Figure 6.14a,b shows some typical examples of this kind of waveform. In other occasions, a bipolar glitch like the one of figure 6.14c is present in every WFD channel. Besides typical oscillations and glitches, there are events depicting very idiosyncratic waveforms; in figure 6.15 we show some representative ones. Finally, events with featureless waveforms and occasional radioactivities have also been included in this

[10]That includes freight elevators and cranes.

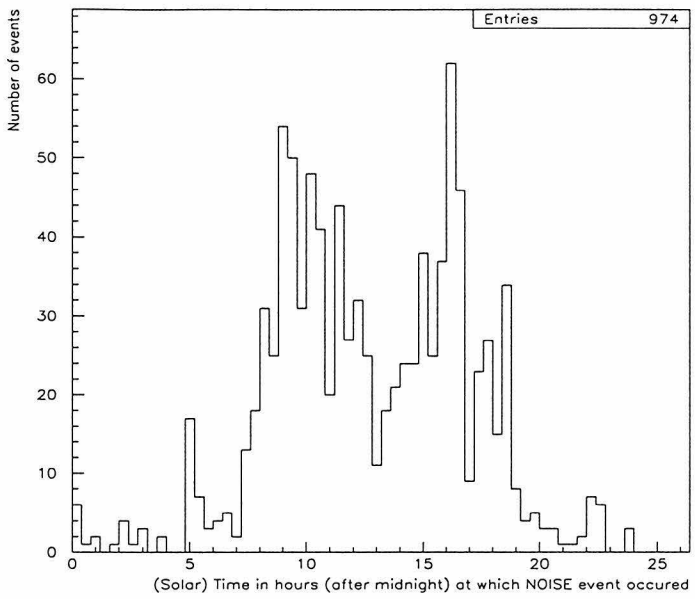

Figure 6.13: Time (in hours) at which noise events were registered by MACRO. This indicates their correlation with the human presence and activity in MACRO.

group since some sort of noise affecting only the monopole trigger circuit (but not reaching the WFDs) is assumed responsible for having generated the trigger. As with the muon-related events, in order to obtain an overall picture of the nature of the waveforms that were classified as noise-related, we plot in figure 6.16 the difference between the positive and negative parts[11] of the waveform integral and the waveform maximum. Being predominantly of bipolar nature, the noise-related waveforms have some sort of axial symmetry (the axis of symmetry is the fitted pedestal) which causes the positive and negative waveform integrals and maxima to differ only by a few counts.

None of the noise-related events has time of flight and waveform pulse shape consistent with the passage of a particle (or particles) through our detector and therefore they were rejected as possible monopole signatures.

[11] After fitting the pedestal, positive is this part of the waveform that is above the pedestal while the part below is the negative.

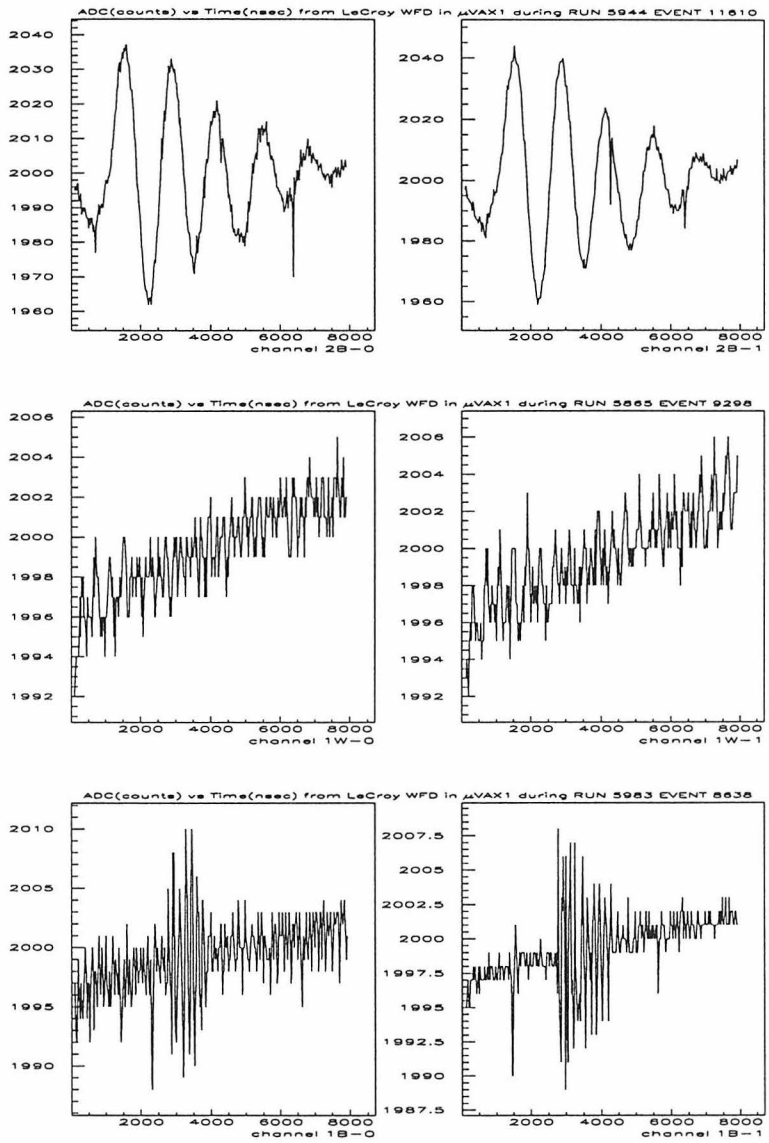

Figure 6.14: Typical waveforms of noise-related events. The top one depicts a "slow" oscillating waveform, the middle one, a "fast" oscillating one and the bottom one, a typical glitch. During these events, waveforms identical to those shown here were present in the rest of the WFD channels.

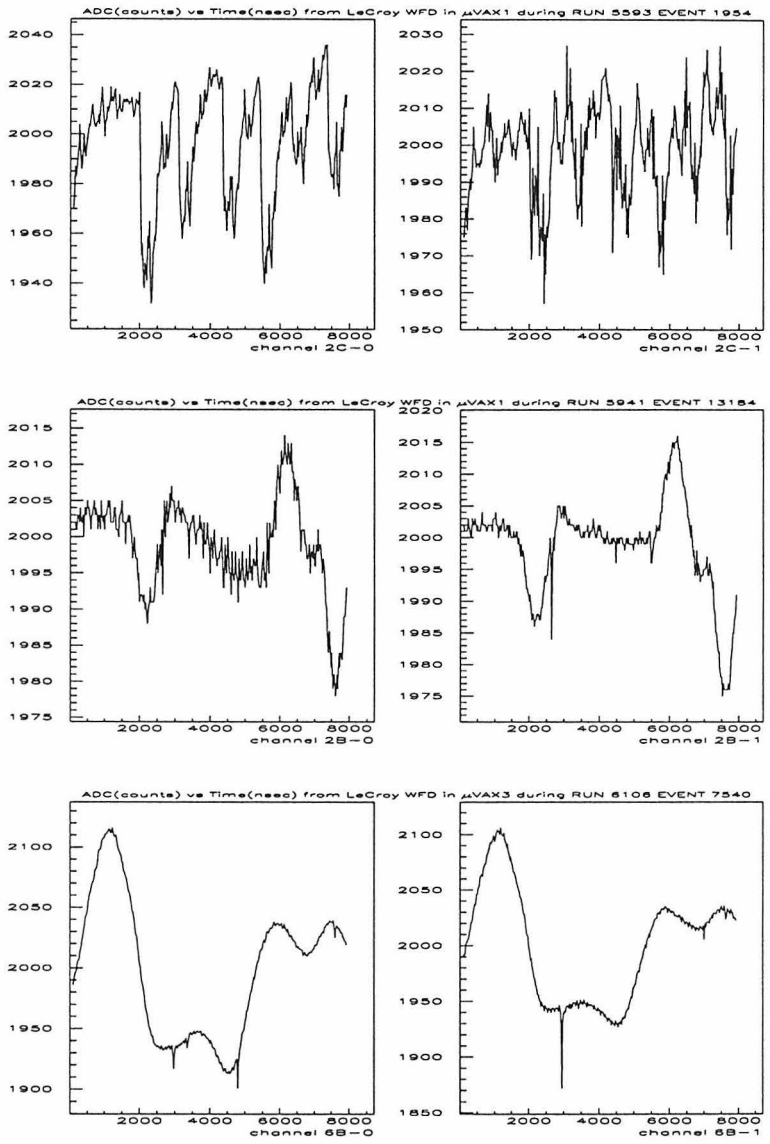

Figure 6.15: Idiosyncratic waveforms of some noise-related events. They were recorded during specific runs and the events came in bursts. During these events, similar pulse shapes were recorded in the rest of the WFD channels. Interestingly enough, the TOF recorded for many of these was of the order of tens or hundreds of μsecs; the pulse shape, however, is completely unphysical (if assumed to arise due to scintillation light in the tank).

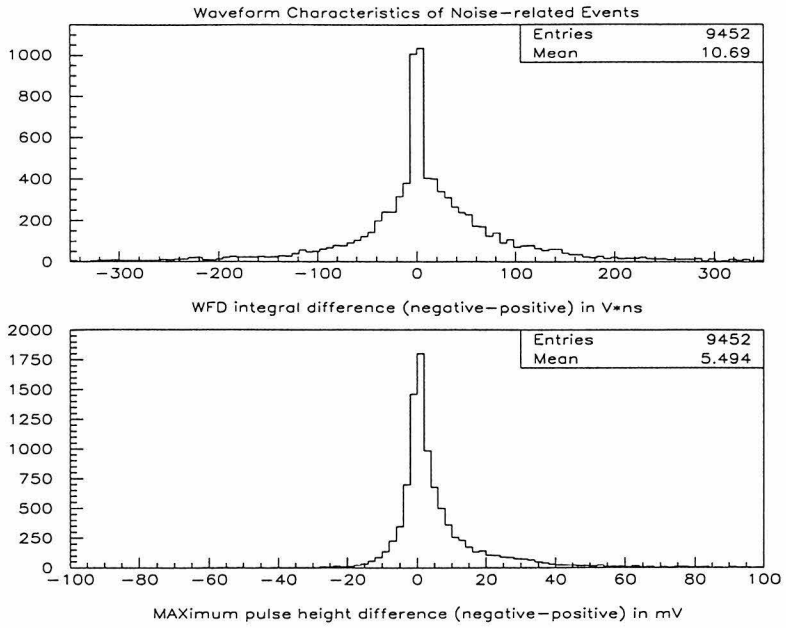

Figure 6.16: Differences (of integrals and maxima) between the negative and positive parts of the noise-related waveforms. More than 96% of the total noise-related events are included in this plot. Both distributions are strongly peaked around zero supporting our symmetry observation. Note that for every noise-related event, there are as many entries in this histogram as the number of detector faces that had at least one SMT trigger during that event.

6.2.4 Radioactivity event

The visual scanning of waveforms yielded one event which was depicting pileups of radioactivity pulses occurring in two faces of the detector. These waveforms are shown in figure 6.17. The trigger involved the scintillator tanks 1E07 and 2C16 and the latching scaler for this event had reached its maximum count, thus suggesting that the corresponding time-of-flight for a hypothetical slow particle was greater or equal to 1.64 msec. Given the fact that the pathlength between these two tanks (1E07,2C16) can be anything from 12m to 28m, the observed transit times in each tank require pathlengths of less than 1cm in order to make the observed waveforms consistent with the passage of a slow particle. Our acceptance Monte Carlo has shown that for an isotropic flux of particles hitting two detectors faces, the requirement for

the pathlengths within the two faces to be less than $1cm$ represents less than 0.01% of the total acceptance.

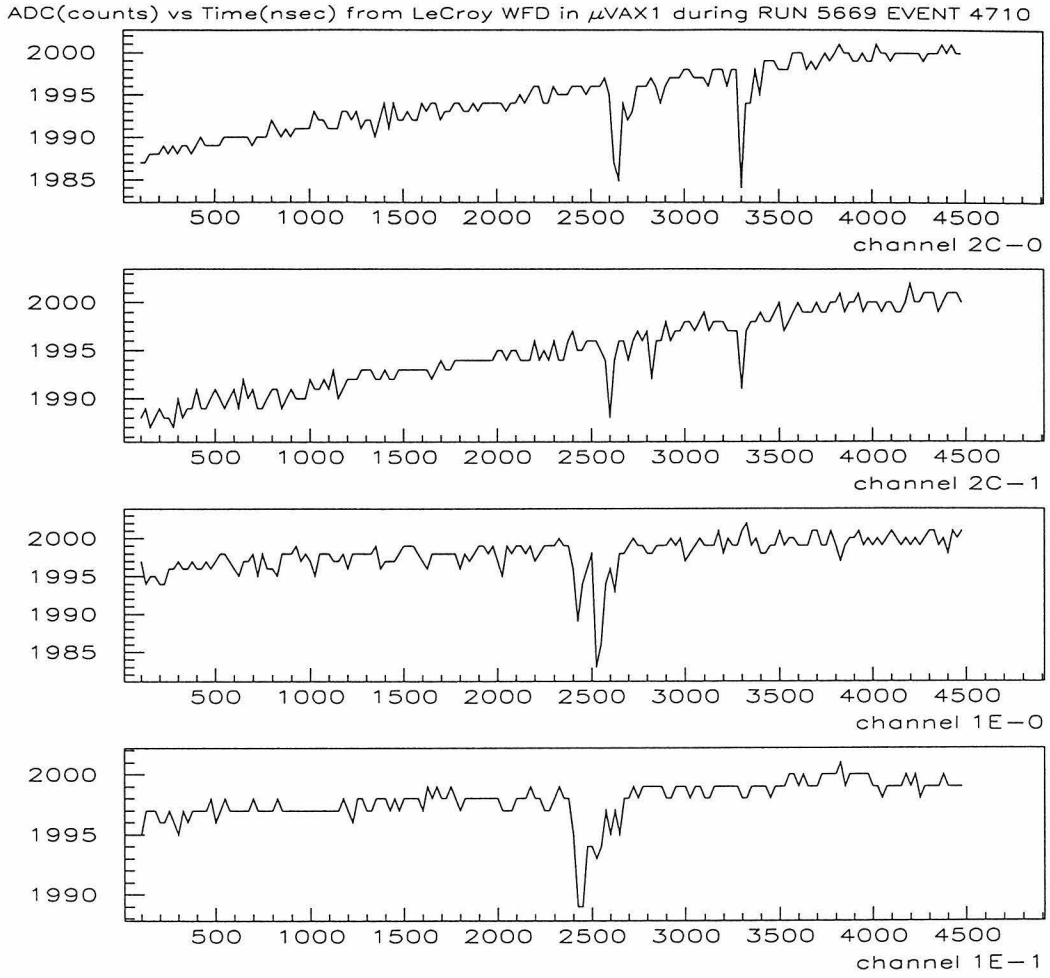

Figure 6.17: Radioactivity present in two different detector faces. The TOF recorded for this event was 1.64 msec. If we make the assumption that these waveforms resulted from a single particle that went through a typical (see fig. E.2) pathlength of 19cm within a scintillator tank, then based on the TOF measured between the two faces we find a pathlength (from face to face) of more than 300m, a distance that is not consistent with MACRO's geometry.

6.3 Analysis Conclusions

At this point we have completed the presentation of the events that we characterized as monopole candidates. Based on our waveform's pulse shape characteristics and the recorded time of flight, none of them was consistent with the passage of a particle (or particles) within the velocity range ($1.5 \times 10^{-4} < \beta < 4 \times 10^{-3}$) at which MACRO's slow monopole trigger is sensitive. This null search will be interpreted as an upper flux limit after calculating the detector's acceptance and livetime.

6.4 Monopole Flux Limit

Although our experiment has not recorded any magnetic monopole event, this does not mean that it has disproven the theory of monopoles. Based on this negative result, we may set an upper limit on the monopole flux. If we assume that there exists a steady isotropic flux of magnetic monopoles F_M, then its upper limit at the 90% confidence level[12] is given by

$$F_M \leq F_{max} = \frac{2.3}{\int \epsilon dA(\theta, \phi, t) d\Omega dt}, \tag{6.5}$$

where $\int dAd\Omega$ is the detector's acceptance to an isotropic flux of particles at instance t and ϵ is the efficiency in identifying a through-going particle as a monopole. We have approximated the integral that appears in the above inequality with respect to t with a sum over the number of MACRO runs that we have analyzed: $\epsilon \sum_i (A\Omega)_i T_i$. Throughout the six-month run MACRO has collected data under various configurations; this involved mostly variations is the number of supermodules and the exact scintillator tanks that were in acquisition. In addition, part of the WFD modules –a crucial part of this analysis– was not functioning properly for part of the running period. For each run i, we have used a Monte Carlo simulation to calculate the detector's acceptance $(A\Omega)_i$ which we then multiplied with the corresponding SMT's

[12] i.e., the probability for the monopole flux limit F_M to be less or equal to F_{max} is 0.9.

livetime T_i. Furthermore, we have corrected T_i for the computer dead time, conservatively taken to be 1% for all the runs. The efficiency ϵ was finally assumed to be constant over the whole running period and equal to 90%.

Our Monte Carlo simulation has taken into account the exact geometry of the MACRO detector and all the requirements that we imposed in analyzing our monopole dataset (see chapter 3). More specifically, for every simulated particle trajectory we required it to traverse a minimum amount of scintillator l_{min} in order to yield the minimum pulse width to trigger the SMT ($t_{min} \sim 160ns$). This minimum pathlength is β-dependent ($l_{min} = 0.5\beta_4 cm$ where $\beta_4 = \beta/10^{-4}$) and it is the one that limits the acceptance for particles faster than $\sim 3 \times 10^{-3}c$. For particle velocities less than this we have chosen the conservative minimum pathlength of $10cm$ within a scintillator tank. The simulated particle trajectories were required to hit two (or more) scintillator tanks corresponding to two detector faces that belong to any two adjacent supermodule combination. Moreover, the scintillator tanks hit by a simulated particle were required to be alive during that run and the corresponding WFD channels to be well-functioning (see appendix E). The pathlength from one face hit to another L_{min} was calculated in order to make sure that the particle "spent" at least $1\mu s$ inside MACRO. As pointed out in chapter 3, this portion of the acceptance is lost as we may not *a priori* claim that any such slow particle with a face-to-face time of flight less than $1\mu s$ will not trigger CSPAM. Like with l_{min}, L_{min} is also β-dependent ($L_{min} = 0.03\beta_4 m$) and has a minor effect in the high-β regime.

In this way we obtained a total effective exposure of $5.6 \times 10^{14} cm^2 sr^1 sec^1$ which corresponds to an upper flux limit to an isotropic particle flux of $4.1 \times 10^{-15} cm^{-2} sr^{-1} sec^{-1}$. The flux limit starts curving up for particle velocities greater than $3 \times 10^{-3}c$ as both the geometry (due to the SMT minimum time-of-flight requirement) and the Haar identification efficiency reduce the effective exposure.

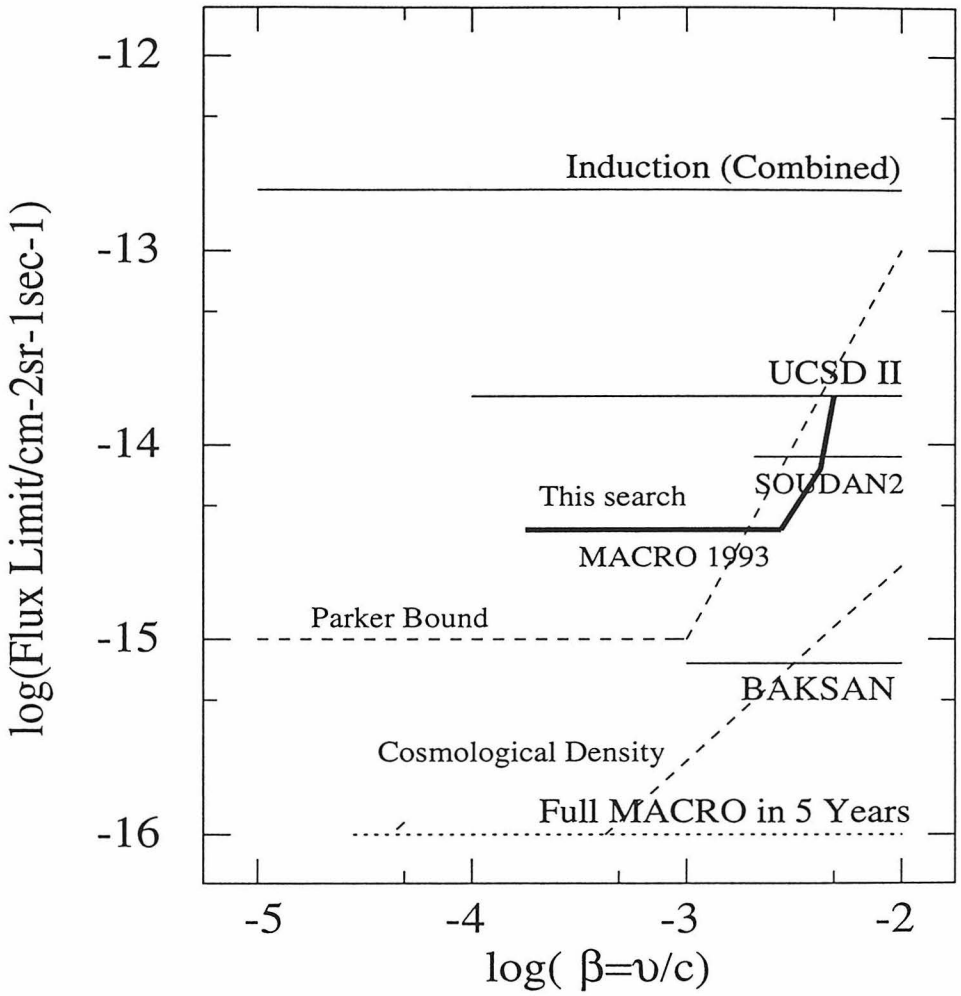

Figure 6.18: Monopole flux limit obtained with MACRO's six-month run (labeled as MACRO 1993). It stands at $4.1 \times 10^{-15} cm^{-2} sr^{-1} sec^{-1}$ (at the 90% confidence level) and it is valid for monopoles traveling with velocities $1.5 \times 10^{-4} c < v < 4 \times 10^{-3} c$. Monopole upper flux limits obtained from other experiments are also shown (see chapter 1 for details). Finally, monopole limits derived from astrophysical and cosmological arguments are also depicted with the assumption that the monopole mass is $\sim 10^{17} GeV$ (see equations 1.13, 1.18, 1.19 and 1.11 of chapter 1).

Chapter 7

Epilogue

We have performed an analysis of the most recent monopole data that the scintillator system of the MACRO detector has collected looking for a signature of a slow moving magnetic monopole going through our apparatus. With no such evidence we have established an upper flux limit of $4.1 \times 10^{-15} cm^{-2} sr^{-1} sec^{-1}$ for monopoles traveling with velocities $1.5 \times 10^{-4} c \lesssim v \lesssim 4 \times 10^{-3} c$. This limit improves by more than 25% an earlier MACRO result which was based on the analysis of its 1989-91 one-supermodule data [77]. In establishing the low velocity threshold we have assumed the Ficenec's et al. curve for the scintillation of slow protons [43]. This search may be used to set flux limits to other supermassive particles that are expected to be moving within our sensitive β-range and be ionizing at least as much as the magnetic monopoles.

One of the problems that this analysis had to overcome was the enormous amount of background events coming from various noise sources and cosmic ray muons, both of which have proven to be the worst enemy of the slow monopole searches with MACRO. Completely human-performed scanning of rare events are always subject to unpredictable systematics and biases and quite often they require collective work in order to cope with the data volume. With these things in mind, we have put forward for the first time the need for an automated method of candidate event selection and investigated the applicability of the Haar decomposition in order to perform the waveform classification based on their *pulse shape*. The proposed Haar transform has the advantage of processing the *raw waveform* information by performing simple additions and subtractions thus making the selection algorithm a very simple, fast and non computationally intensive tool. The Haar transform is only the simplest of a family of functions called "wavelets" which provide time-frequency localization of the signals that they analyze and it should not be taken as the end of the analyses

framework. As the full MACRO detector is currently being equipped with new waveform digitizer equipment which will allow MACRO to perform even more sensitive searches, new wavelet bases may be investigated or even constructed [33] in order to match the hardware's sensitivity. Needless to say, the hunt for the supermassive magnetic monopole is not over yet. The full MACRO detector will start collecting monopole data within a few months awaiting for confirmation of Cabrera's event [26] until the turn into the third millennium. However, for the time being we can not do anything else but reinforce J. Preskill's remark [94] almost ten years after it was made: *" ... as of this writing (early 1984), it is not certain that nobody has ever seen one (monopole). What seems certain is that nobody has ever seen two."*

Appendix A

The MACRO Collaboration

S. Ahlen[3], M. Ambrosio[12], R. Antolini[7], G. Auriemma[14,a], R. Baker[11], A. Baldini[13], G.C. Barbarino[12], B.C. Barish[4], G. Battistoni[6,19⋆], R. Bellotti[1], C. Bemporad[13], P. Bernardini[10], H. Bilokon[6], V. Bisi[16], C. Bloise[6], C. Bower[8], S. Bussino[14], F. Cafagna[1], M. Calicchio[1], D. Campana[6], M. Carboni[6], S. Cecchini[2,b], F. Cei[13], V. Chiarella[6], R. Cormack[3], A. Corona[14], S. Coutu[11], G. DeCataldo[1], H. Dekhissi[2,c], C. DeMarzo[1], I. De Mitri[9], M. De Vincenzi[14,d], A. Di Credico[7], E. Diehl[11], O. Erriquez[1], C. Favuzzi[1], D. Ficenec[3,e], C. Forti[6], P. Fusco[1], G. Giacomelli[2], G. Giannini[13,f], N. Giglietto[1], M. Goretti[14], M. Grassi[13], P. Green[15,18⋆], A. Grillo[6], F. Guarino[12], P. Guarnaccia[1], C. Gustavino[7], A. Habig[8], K. Hanson[11], R. Heinz[8], J.T. Hong[4,3⋆], E. Iarocci[6,g], E. Katsavounidis[4], E. Kearns[3], S. Klein[3,h], S. Kyriazopoulou[4], E. Lamanna[14], C. Lane[5], D. S. Levin[11], P. Lipari[14], G. Liu[4], R. Liu[4], M.J. Longo[11], Y. Lu[15], G. Ludlam[3], G. Mancarella[10], G. Mandrioli[2], A. Margiotta-Neri[2], A. Marin[3], A. Marini[6], D. Martello[10,17⋆], A. Marzari Chiesa[16], P. Matteuzzi[2], M.N. Mazziotta[1], D.G. Michael[4], S. Mikheyev[7,i], L. Miller[8], M. Mittelbrun[5], P. Monacelli[9], T. Montaruli[1], M. Monteno[16], S. Mufson[8], J. Musser[8], D. Nicoló[13], R. Nolty[4] S. Nutter[11], C. Okada[3], G. Osteria[12], O. Palamara[10], S. Parlati[4,7⋆], V. Patera[6,g], L. Patrizii[2], B. Pavesi[2], R. Pazzi[13], C.W. Peck[4], J. Petrakis[8,17⋆], S. Petrera[10], N.D. Pignatano[4], P. Pistilli[10,14⋆], A. Rainó[1], J. Reynoldson[7], F. Ronga[6], G. Sanzani[2], A. Sanzgiri[15], F. Sartogo[14], C. Satriano[14,a], L. Satta[6,g], E. Scapparone[2], K. Scholberg[4], A. Sciubba[6,g], P. Serra Lugaresi[2], M. Severi[14], M. Sitta[16], P. Spinelli[1], M. Spinetti[6], M. Spurio[2], J. Steele[5], R. Steinberg[5], J.L. Stone[3], L.R. Sulak[3], A. Surdo[10], G. Tarlé[11], V. Togo[2], V. Valente[6], C.W. Walter[4], R. Webb[15], and W. Worstell[3].

(MACRO Collaboration)

1. Dipartimento di Fisica dell'Università di Bari and INFN, Bari, 70126, Italy

2. Dipartimento di Fisica dell'Università di Bologna and INFN, Bologna, 40126, Italy

3. Physics Department, Boston University, Boston, MA 02215, USA

4. California Institute of Technology, Pasadena, CA 91125, USA

5. Department of Physics, Drexel University, Philadelphia, PA 19104, USA

6. Laboratori Nazionali di Frascati dell'INFN, Frascati (Roma), 00044, Italy

7. Laboratori Nazionali del Gran Sasso dell'INFN, Assergi (L'Aquila), 67010, Italy

8. Depts. of Physics and of Astronomy, Indiana University, Bloomington, IN 47405, USA

9. Dipartimento di Fisica dell'Università dell'Aquila and INFN, L'Aquila, 67100, Italy

10. Dipartimento di Fisica dell'Università di Lecce and INFN, Lecce, 73100, Italy

11. Department of Physics, University of Michigan, Ann Arbor, MI 48109, USA

12. Dipartimento di Fisica dell'Università di Napoli and INFN, Napoli, 80125, Italy

13. Dipartimento di Fisica dell'Università di Pisa and INFN, Pisa, 56010, Italy

14. Dipartimento di Fisica dell'Università di Roma and INFN, Roma, 00185, Italy

15. Physics Department, Texas A&M University, College Station, TX 77843, USA

16. Dipartimento di Fisica dell'Università di Torino and INFN, Torino, 10125, Italy

17. Bartol Research Institute, University of Delaware, Newark, DE 19716, USA

18. Sandia National Laboratory, Albuquerque, NM 87185, USA

19. INFN Sezione di Milano, 20133, Italy

$\star$ Current address

a Also Università della Basilicata, Potenza, 85100, Italy

b Also Istituto TESRE/CNR, Bologna, Italy

c Also at Faculty of Science, University Mohamed I, Oujda, Morocco

d Also at Università di Camerino, Camerino, Italy

e Now at Physics Department, Washington University, St. Louis, MO 63130, USA

f Also Università di Trieste and INFN, Trieste, 34100, Italy

g Also Dipartimento di Energetica, Università di Roma, Roma, 00185, Italy

h Now at Department of Physics, University of California, Santa Cruz, CA 95064, USA

i Also at Institute for Nuclear Research, Russian Academy of Science, Moscow, Russia

Appendix B

Muon Light Yield

The passage of particles that carry electric or magnetic charge through MACRO's scintillator tanks results in energy loss that is converted to light via scintillation. As we have seen, for the purpose of this analysis, the LeCroy Waveform Digitizers (WFDs) was the main equipment that was used to record phototube (PMT) signals of all the events. Here, we are mostly concerned about estimating the light yield of a muon as recorded by this piece of hardware.

There are various factors that determine the number of photoelectrons (p.e.) seen by a PMT when a muon crosses a tank at distance x from the PMT. First of all is the energy deposited by the muon and the absolute scintillation efficiency (scintillator dependent) that determine the number of photons generated at the interaction point. Then, it is the light propagation and collection (scintillator and box geometry dependent) that determine the actual number of photons that reach the PMT, and finally is the photocathode efficiency of the PMT which converts photons to photoelectrons. So, we may write the observed number of p.e. as follows (assuming linearity of the scintillator):

$$pe = E_\mu R(x), \tag{B.1}$$

where E_μ is the energy deposited by the muon and $R(x)$ is the response function that tells us how may p.e. we should expect for every unit of energy deposited by the muon at distance x from the PMT. Being a function of the scintillator's characteristics, the tanks' geometry and the PMT's quantum efficiency, it is reasonable to assume $R(x)$ to

be the same for all the tanks[1]. We have used single muon[2] data to study the response of the WFDs to muons. From the recorded muon waveforms, after fitting the pedestal, we calculated the integral charge. In doing so, we *subtracted* the "positive"[3] part of the waveform from the negative one, making our calculation rather *conservative.* For all muon events, the ERP system offers accurate (within 10 cm, [35]) position determination along the scintillator tanks. In figure B.1a we plot for muon events the waveform integral versus the position in the tank. On the same figure we have superimposed the box response function $R(x)$ of the semi-empirical form [35]:

$$R(x) = \frac{a}{x^2} + be^{-x/\lambda_1} + ce^{-x/\lambda_2}, \tag{B.2}$$

where a,b,c are constants determined through calibrations and λ_1 and λ_2 are the attenuation lengths. Apart from the geometric term $1/x^2$, the two exponential terms were found to *fit* nicely the attenuation of light in the scintillator boxes[4]. The precise determination of the box response function is not important for the purpose of our analysis since we do not really rely on any energy measurement. Selecting muons that pass through the far end of a scintillator tank (with respect to the recording PMT), we plot in figure B.1b a histogram of the recorded waveform integrals. As we can see, the most probable value is roughly $30V \times ns$; we can then state that no matter where the muon hits a scintillator tank, the light recorded by the WFDs is *at least* $30V \times ns$ *in both ends.*

One may ask how this number is interpreted in terms of number of photoelectrons.

[1]The PMT quantum efficiency varies by approximately 10% from PMT to PMT while a similar variation might exist in the scintillator box geometric response. Although we have not performed a systematic study of neither of them, their effects on this analysis are minor.

[2]We define as single muons the CSPAM events with only one ERP hit in each face. Although the additional requirement of a streamer tube track would have selected 100% single muons, the radioactivity background introduced by relaxing it is negligible and makes contributions –if any– appreciably off the muon peak.

[3]We define as "positive" the part of a waveform that lies above the fitted pedestal.

[4]The attenuation of light is due to the scintillator opacity and due to the reflections. Since both processes occur simultaneously, one *should not* try to interpret the two lambda's in equation B.2 as coming from the two processes respectively. Equation B.2 is found to fit the data better than a single exponential and that is why it is used; its physical source is other than the two attenuation procedures.

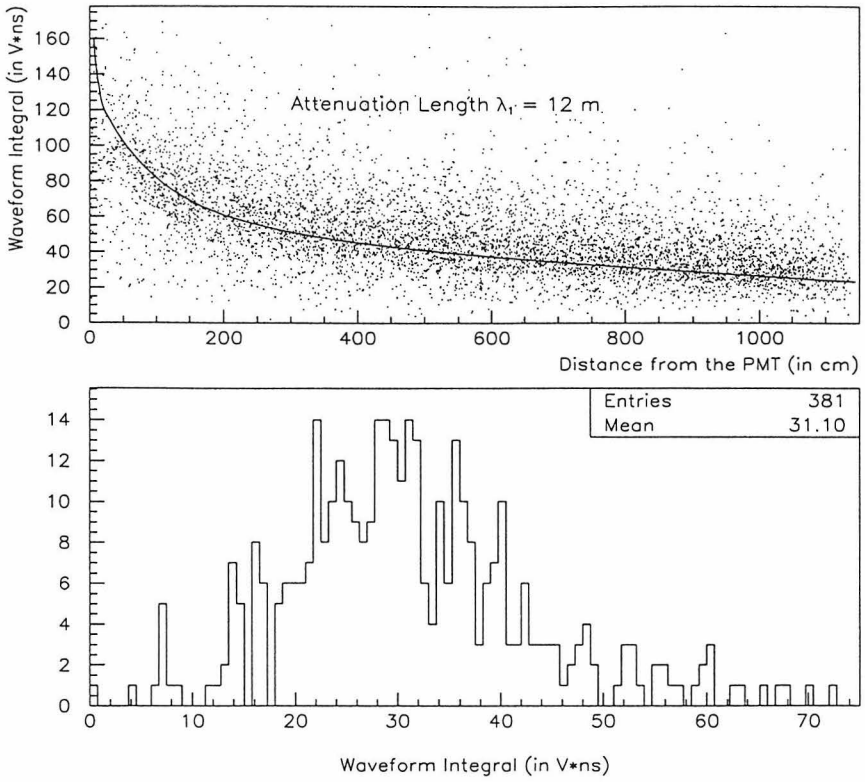

Figure B.1: Waveform Integral versus distance from the PMT (top plot). The superimposed curve is of the empirical form B.2 and it serves only as a guide to the eye; it is *not* a fit. The bottom plot shows the projection of the upper plot onto the waveform integral axis for muons crossing within one meter at the opposite side of the scintillator tank from the PMT.

First of all, let us state that the actual p.e. number is not needed in any step of our analysis or in our sensitivity measurement. In both cases, we use the WFDs to measure the charge (in units of $V \times ns$), and all the muon light yield does is offer a convenient detector-independent normalization. Nevertheless, in trying to address this question, it is obvious that we need to know the integral of the single photoelectron PMT pulses *as recorded by the* WFDs. Unfortunately, we do not have this number; however, we have an approximate measurement of the integral of PMT pulses at the single photoelectron level performed on a digital oscilloscope *directly at the* PMT *fanouts* [102]. The measurement yielded 50 $mV \times ns$, which translates the waveform integral of $30V \times ns$ to 600 photoelectrons. This is a *lower bound* since

in the above estimate we *did not* take into account the *attenuation* coming from the CSPAM fanins.

Appendix C

Wavelet Trigger Simulations

In chapter 5, we studied the sensitivity of the slow monopole trigger circuit and the Haar filter using calibration data. Here, we study the efficiency of the Haar algorithm using Monte Carlo methods in order to generate monopole-like signals.

Let us assume[1] a square monopole-like pulse train which we will model with a constant photoelectron density as function of time:

$$\lambda(t) = \lambda_0 \quad for \ t \in [0, T], \tag{C.1}$$

where λ_0 is the constant density of photoelectrons (p.e.) and T is the pulse duration. Given λ_0, we generate the time sequence of p.e. according to Poisson statistics:

$$t_{n+1} = t_n - \frac{1}{\lambda_0} log R, \tag{C.2}$$

where t_{n+1} is the time at which the $(n+1)^{th}$ p.e. occurred assuming the n^{th} one was at time t_n. R is a random number between zero and one. The single photoelectron pulse shape is modeled according to the following equation:

$$u(t) = -\frac{qe^2t}{w^2} exp(-\frac{et}{w}) h(t), \tag{C.3}$$

where q is the charge of single p.e. pulses, e is the base of natural logarithms (=2.71828...), w is their effective pulse width and $h(t)$ is the step function at $t = 0$.

[1]The pulse train generation described herein follows the ideas described by Jiang-Tao Hong in his Ph.D. thesis [54]. Jiang-Tao Hong provided the library of routines in order to generate monopole-like pulse trains for this simulation. We have simply adapted these routines to describe the exact detector (PMTs, WFDs) configuration.

The minus sign is present because MACRO's PMTs are operated with negative high voltage, thus resulting in negative-going pulses. As we have seen in chapter 2 (figure 2.7), the single p.e. charge spectrum for the EMI PMTs is described by a *Gaussian*; in our pulse train simulation we sample the p.e. charge from this *Gaussian* assuming an average charge of $g = 50mV \times ns$ and a sigma of $17mV \times ns$. With an average pulse height of $4mV$, single p.e. pulses have an effective width of $w = 12.5ns$; fluctuations in the single p.e. pulse width have also been taken into account by sampling w from a Gaussian of a mean of 12.5ns and a sigma of 3.0ns. The final pulse shape is obtained by summing all the single p.e. pulses that were generated:

$$S(t) = \sum_{n=1}^{N} u(t - t_n), \tag{C.4}$$

where N is the total number of p.e.'s in the train and u(t) is given by C.3.

In order to account for the oscillatory noise that was present in the WFDs during the six-month run, we have superimposed on $u(t)$ a sinusoidal noise of 10MHz frequency and 20mV peak-to-peak[2]. $S(t)$ is then digitized according to the operational characteristics of the LeCroy 2261 WFDs: 40MHz sampling rate and 1mV/count. The resulting digitized simulated pulse train is then fed through exactly the same algorithm that we used to select monopole waveforms from the real (and calibrated) event dataset. As in the calibration runs, by varying the width and the number of p.e.'s in the simulated pulse train, we map the Haar wide signal filter efficiency in the β versus light parameter space.

In figure C.1 we plot the Haar efficiency versus the light yield for pulse trains of various durations (i.e., β's). The efficiency was checked both for noise-free and noise-dominated waveforms. From these plots we may obtain the required light yield in order for the algorithm to be 90% efficient. The result is shown in figure C.2, where the 90% sensitivity curves and the expected monopole light yield [43] are drawn.

[2]Cross-talk on the clock distribution resulted in an oscillatory noise which was present in most of the WFD channels for most of the duration of the six-month run. Although its periodicity was consistently at 10MHz, its amplitude varied from a couple of mV to 10mV. Apparently, our assumption of 20mV peak-to-peak accounts for the *worst case scenario*.

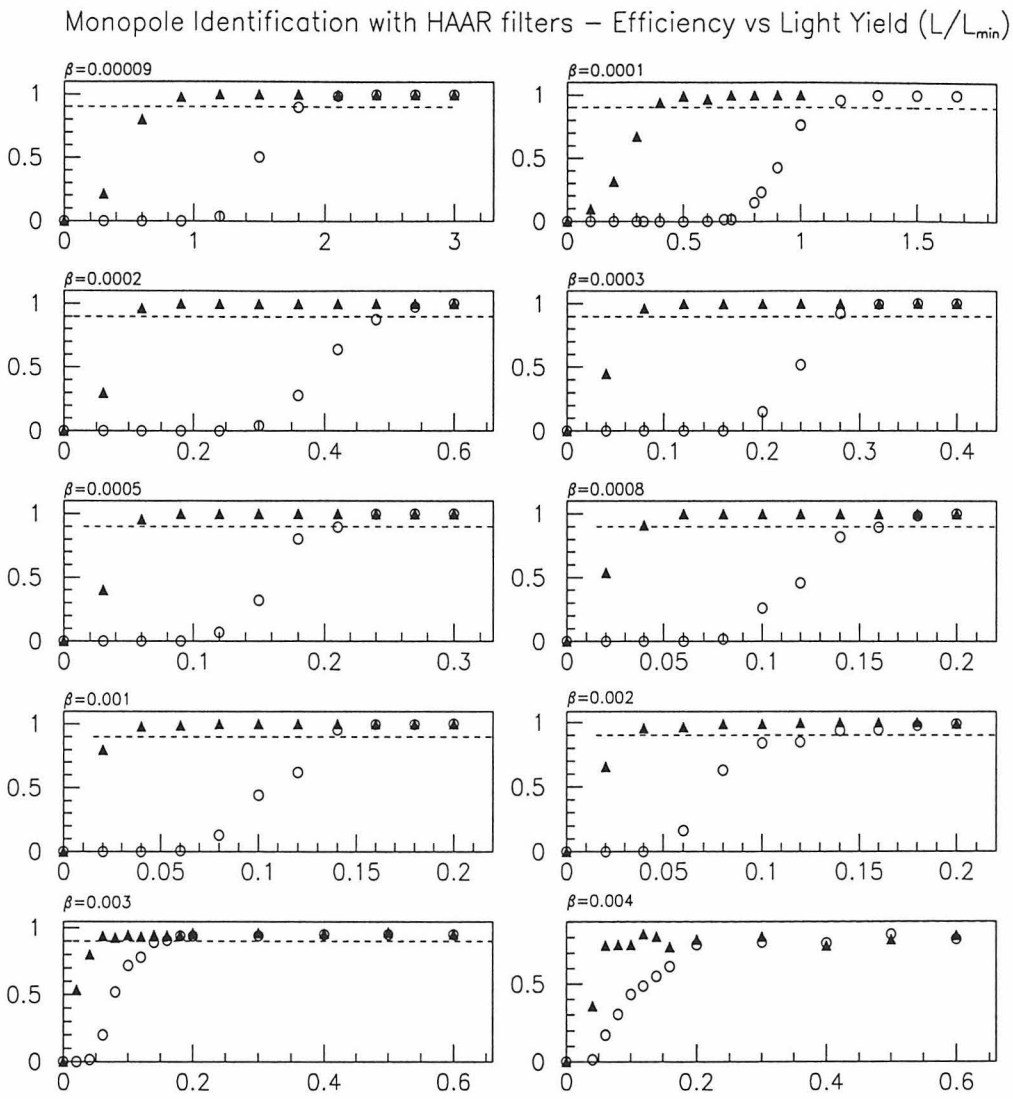

Figure C.1: Efficiency of Haar algorithm as a function of light yield (in units of L_{min}) for monopole-like waveforms generated according to [54] [43]. The β of the monopole determines the width of the pulse (assuming $19cm$ pathlength within a scintillator tank). The filled triangles correspond to noise-free waveforms while the open circles correspond to the case of oscillatory noise superimposed.

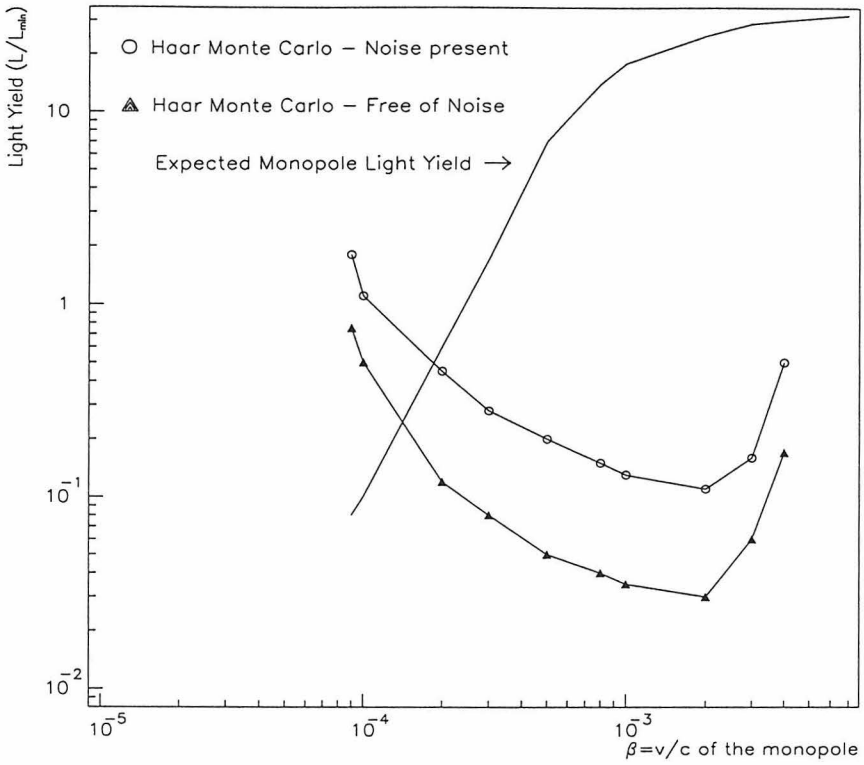

Figure C.2: 90% sensitivity curves for monopole identification using the Haar algorithm. For a monopole of a given β, the Haar algorithm becomes 90% efficient for light yields higher than the ones defined by the curves. Apparently, the presence of oscillatory noise reduces significantly the sensitivity of the algorithm over the whole velocity range. For $\beta = 4 \times 10^{-3}$ the points correspond to 80% efficiency, while for any β greater than that the sensitivity curves rise to infinity (zero efficiency).

Appendix D

Wavelets as a Muon Detector

In chapter 4, where we introduced the wavelet transform, we hinted at the use of Haar features to detect "sharp" signals. Here we study the capabilities of the Haar decomposition to detect such waveforms which are characteristic of muons and radioactivities.

As we have seen in chapter 2, the ERP is the primary muon hardware trigger for MACRO's scintillator system. The ERP triggers primarily on muons and –being a single box trigger– on radioactive decays that are energetic enough to satisfy its threshold at both ends of a scintillator tank. The WFDs readout upon ERP events thus provides us with waveforms for which we know *a priori* whether they should depict a "sharp" signal or just background in the WFD window[1]. In order to discard multi-muon and showering events (which we have shown to depict rather "fat" waveforms[2]), we have excluded events that had more than one ERP box fired within a detector's face. Starting off with the Haar decomposition of only 256 buckets (out of the 320 read), we plot in figure D.1 the wavelet features of waveforms where an ERP trigger is present (left column) and where it is not (right column).

We have already presented in chapter 5 Haar features of background waveforms; here we once again see them exhibiting small global Haar maxima which decay fast through the consecutive resolution scales resulting in almost no appreciable contrast between high and low scales and alignment which shows no strong preference.

[1]This is similar to the LED monopole calibrations where we knew a priori where (i.e., in which WFD channel) an LED had generated a monopole-like pulse.

[2]See chapter 6.

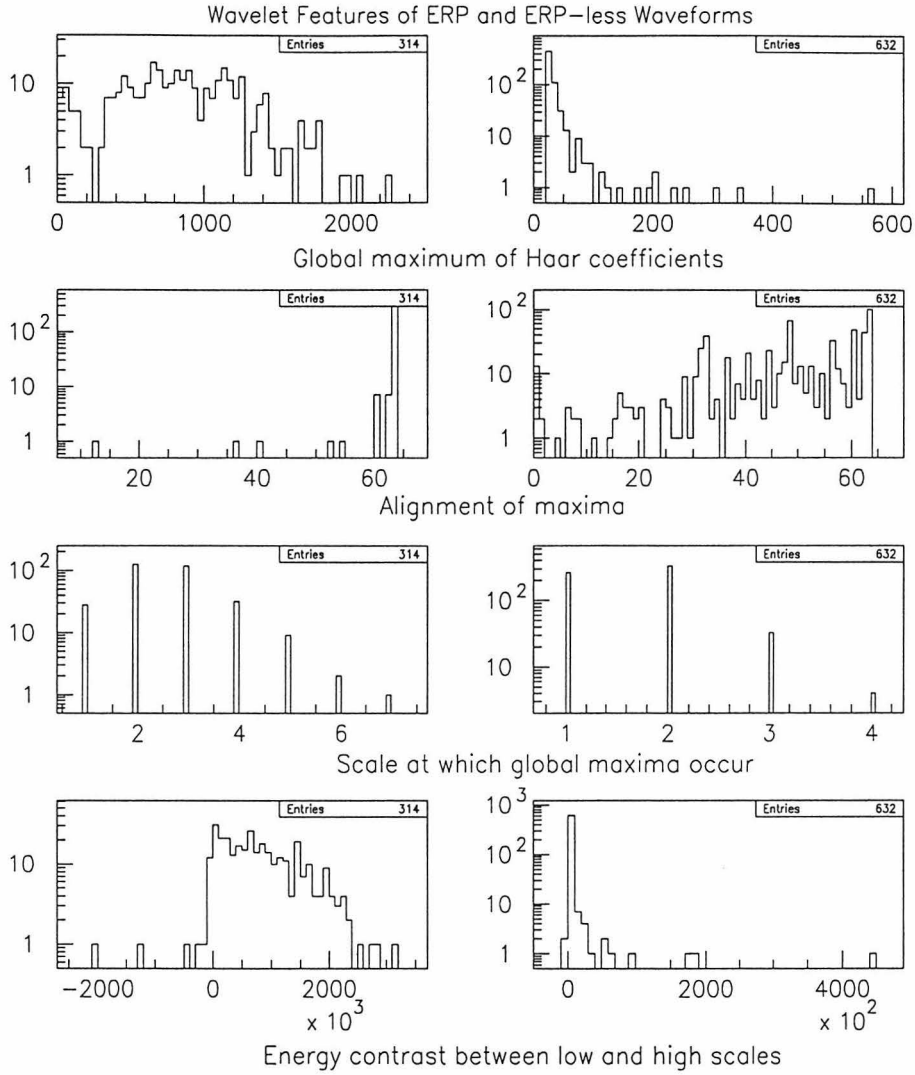

Figure D.1: Features of the Haar decomposition of ERP (left column) and background (right column) waveforms. In each of these plots there is one entry per waveform. Only (the last) 256 buckets of a waveform channels have been processed and for the background waveforms a global Haar maximum greater than 20 is required (see chapter 4 for definition of terms used in this plot). The Haar sharp-signal filter requirements of positive energy contrast, Haar focus below the fifth scale and full alignment of maxima accept 281 out of the 314 ERP waveforms. One may notice the different horizontal scales of the left and right columns in the top and bottom plots.

On the other hand, we can see the ERP waveforms having their maxima mostly aligned along all scales[3] and the energy strongly focused in the first scales. These are the underlying features of sharp waveforms which led us to the definition of the "sharp filter" in chapter 4: any waveform that has the maxima fully aligned, the global maximum occurring at the first four scales and the energy focused at the low scales will be labeled as a sharp one. However, one may straightforwardly observe that there are ERP waveforms which would fail to satisfy this requirement, while on the other hand, there can potentially be several background waveforms which would be classified into the sharp-signal category. It is thus essential to understand what kind of background waveforms fall into the "signal" region and vice versa and, furthermore, to attempt to estimate the algorithm's signal to noise detection capabilities.

By applying the additional requirement that the global Haar maximum be greater than a certain value, we plot in figure D.2 the fraction of the background (ERP-less) and ERP waveforms that were identified as having a sharp signal in them. The far right region of the top plot and the most left one of the bottom plot are the regions of interest since they will reveal inefficiencies of the ERP hardware trigger and the Haar algorithm respectively. Viewing the global Haar maximum of a waveform as a measure of the maximum pulse height present in it, we may understand the behavior of the sharp filter as a function of the global Haar maximum shown in figure D.2. Background waveforms may occasionally depict pulses of a few mV coming from radioactive decays; while these events are not energetic enough to trigger ERP, they can trivially satisfy the sharp filter criteria and thus be selected. The decay of the fraction of the background waveforms identified as sharp essentially reflects the decay of the radioactivity spectrum as pulse height increases. Given the ERP trigger's front-end discriminator threshold of several tens of mV[4], the Haar algorithm is expected to

[3]We check if for the wavelet maximum in a given scale there is a "corresponding" one in the next one. Doing this for the seven resolution scales, we construct a binary number (6 bits) whose bit state represents whether or not the alignment was present for that "step" of the scale progression. If the maxima along all the scales are aligned, the decimal representation of the resulting binary number is obviously $2^6 - 1 = 63$. See chapter 4 for details.

[4]For the ERP system the discriminator level *before* the energy trigger is at 100mV for the horizontal tanks and at 50mV for the vertical tanks.

be fully efficient in picking up the sharp signal as long as the global Haar maximum requirement is small enough. For the case of ERP waveforms, a further increase in the global Haar maximum selects muons of different light yields while for the background waveforms one would nominally expect to drive the sharp signal identification to *zero if the ERP is a 100% efficient trigger.*

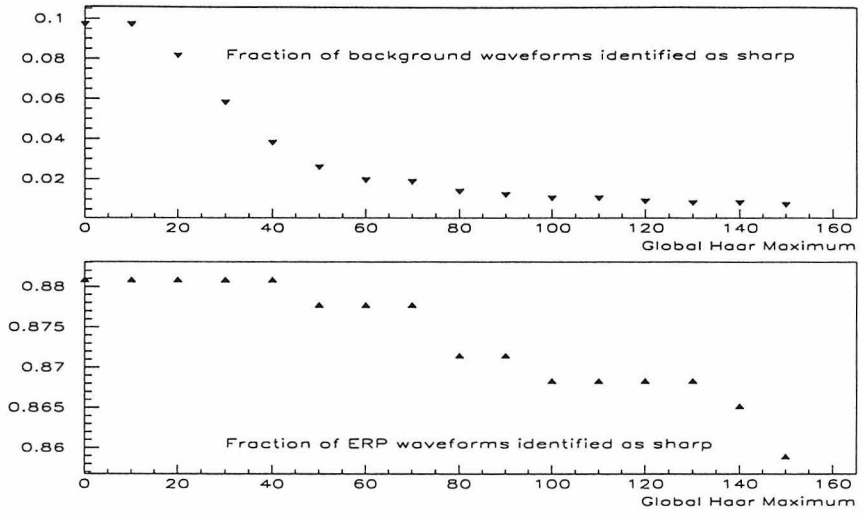

Figure D.2: Fraction of background (ERP-less, top plot) and ERP waveforms (bottom plot) that satisfied the sharp signal criteria with the further requirement that their global Haar maximum be greater than the abscissa value (notice the different vertical scales).

As suggested by both D.1 and D.2, sharp signal identification for background waveforms yielded of the order of 15 events (of the dataset that we examined) in the regime (gmax> 100) where one would expect ERP to trigger with a high probability. We have hand-scanned the waveforms of these events in order to further understand their nature: most of them are one-end-only events which fail to trigger the ERP simply because ERP is an end-to-end coincidence trigger. However, there are events depicting waveforms that would have nominally been enough to trigger ERP in *both* ends of a tank, thus suggesting some ERP inefficiency. An example is shown in figure D.3.

Going back to figure D.2, the question that remains to be addressed is the rather poor efficiency of the Haar sharp filter to identify ERP waveforms. This inefficiency

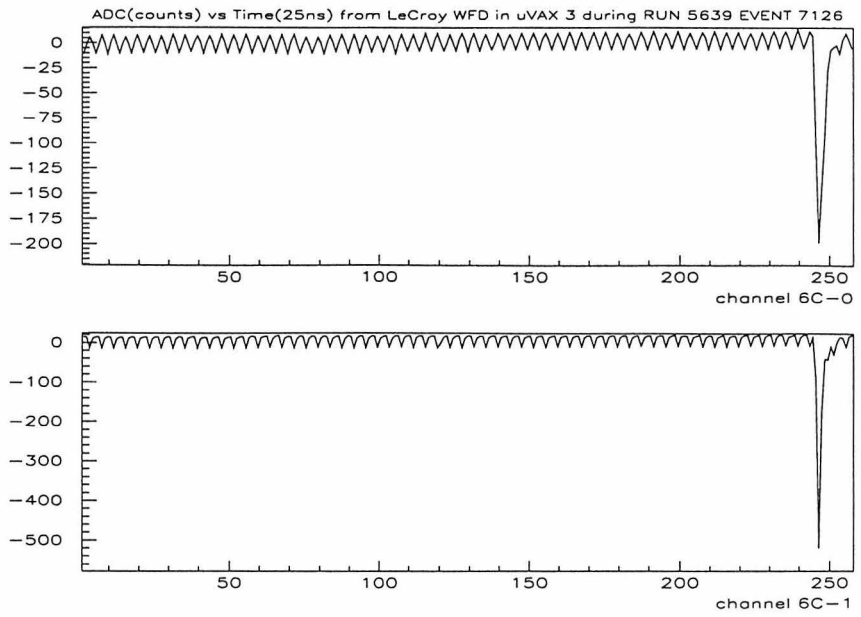

Figure D.3: Both of the above waveforms have been identified by means of the Haar transform as sharp ones. Although their apparent pulse height and pulse integral (number of photoelectrons) should have been enough to trigger the ERP in both ends of the tank, the ERP failed to fire.

has nothing to do with the further requirement on the global Haar maximum since it does not vary significantly as the Haar maximum requirement varies. Therefore, the inefficiency must be due to a rather systematic effect. As we may recall, we have performed the Haar decomposition of only the last 256 out of the 320 buckets of the waveform window; if for any reason the muon waveform happens to be outside this window, the "effective" waveform[5] will be just another background waveform which legitimately the Haar algorithm ignores! This is rather easy to fix: we shift the decomposition window in order to include the waveform buckets that were skipped before. Shifting the analyzing window and searching for sharp signals among the newly decomposed waveforms recovers roughly 25% of the "missing signal." One may notice that most of the remaining missed waveforms happened to have misaligned maxima between the first and second resolution scales[6]. This is as if the Haar decomposition

[5]i.e., the waveform "seen" by the Haar algorithm.

[6]Look at the alignment of maxima plot in figure D.1. Missing the alignment between the first and second resolution scale results in the binary number 111110 which is plotted as decimal 62 in

had missed the true location of the sharpest variation in the first resolution scale. This indeed can happen and it is the result of the dyadic sequence over which the Haar transform is performed. If we assume that the sharpest signal variation occurs between the waveform buckets $[n, n+1]$, then this will obviously *not* be detected if n is even[7]. This is shown in figure D.4 where we have zoomed down in the sharp signal region of a waveform and its Haar decomposition in the first scale that failed to be identified as sharp: because the sharp signal transition occurred in the [238,239] bucket pair, it was skipped and instead the bucket pair [243,244] was identified as carrying the maximum Haar coefficient. In order to account for this effect, we *shift* the waveform window by *one* and decompose it again; the true Haar maximum in the first scales is now found and the waveform is identified as sharp. Performing these additional decompositions of the shifted-by-one-bucket waveforms, we recover an additional 25% of the missing signal. The remaining 50% of the missing signal is mostly due to malfunctioning of the WFDs; hand-scanning of these waveforms reveals that there is actually *no sharp* signal to detect at all! Only less than 1% accounts for muon waveforms that were marginally rejected basically because they did not meet the requirement on the global Haar maximum (set at 80) or they were at the tail of the pulse width distribution making them to appear not sharp enough.

In conclusion, we may observe that our proposed wavelet-based algorithm for sharp signal detection is a very *fast* and *efficient* tool for muon and radioactivity signal identification from the waveform information *only*. This is quite important since muons and isolated radioactivities constitute a significant part of the background for monopole searches. Being able to probe the waveform information locally (in time), it may also be developed to provide significant help on handling waveform signatures expected from various types of physics processes. Although MACRO was not equipped to look for monopole catalyzed proton decay events during the six-month run[8], it is anticipated that we can do so in the near future with the new WFDs that

---

the above plot.

[7]Here we make the assumption that the waveform buckets are numbered starting with number one.

[8]See chapter 2.

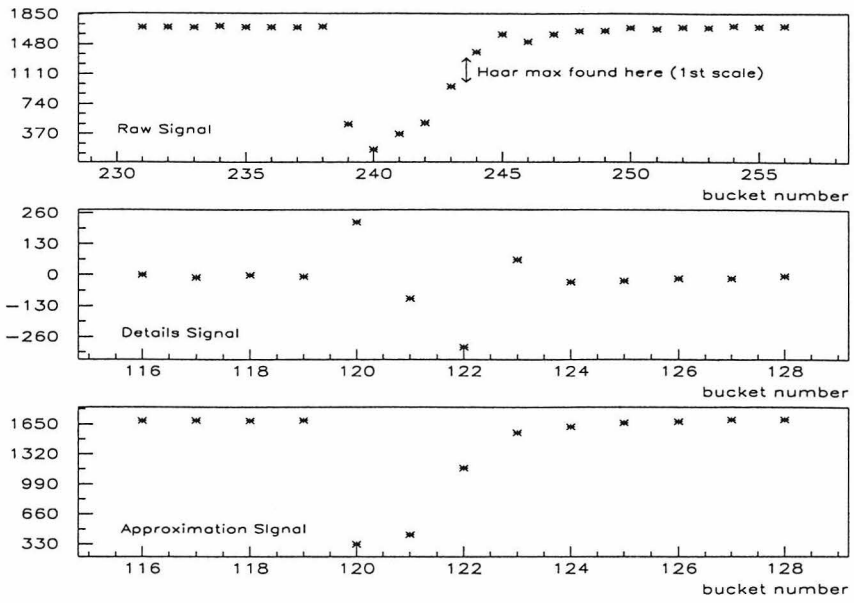

Figure D.4: The last 26 buckets of the original waveform (top) and the corresponding details and approximation signals of its first scale Haar decomposition (see chapter 4). The biggest variation of the original signal occurs between buckets [238,239] but it is missed; it may be recovered, however, if the waveform is shifted by one bucket. See text for discussion.

are currently being installed. For this kind of event, a sharp signal (coming from the relativistic electrically charged decay product) is expected to precede the monopole's wide pulse and by means of the wavelet transform such an early waveform can be routinely identified and subtracted. The remaining waveform could be then rechecked and searched for a monopole signature.

Appendix E

Detector Monitoring and Acceptance Calculation

In this appendix we describe the procedure we followed in monitoring the MACRO detector throughout the duration of the six-month run. In addition, we present some of the details of our acceptance Monte Carlo. These two are closely related since a reliable calculation of the acceptance requires full knowledge of the status of the detector at each moment.

As we have seen in chapter 2, the data acquisition of the MACRO detector organizes the data it collects in "runs" whose length is determined by the size of the output data file. During the six-month run, a monitor job was executed at the end of each run in order to perform basic statistics on the collected data and to check for possible problems with MACRO's hardware. Part of the output of this monitor job for a typical MACRO run is shown in the table E.1 at the end of this appendix. We have used the information contained in these files in order to define the Slow Monopole Trigger (SMT) livetime on a run-by-run basis as the maximum of the SMT's livetime among the microvaxes in acquisition. In addition, we define a scintillator box to be "alive" during a given run if it produced at least one slow monopole trigger. Besides a few boxes that were kept out of the data acquisition for the whole duration of the six-month run[1], there were individual boxes that were temporarily disconnected either because of their extremely high trigger rate or because of needed maintenance. For a scintillator box that produced at least one SMT trigger during a run, we consider as its livetime the SMT livetime defined above. Any possible error in the above scintillator box livetime definition is introduced when a box becomes inactive –for any reason– *during* the course of a run. In this case, its livetime is overestimated

[1]These boxes had mechanical problems that prevented us from filling them with scintillator and putting them in acquisition.

for a maximum of the average duration of a run. We have randomly examined the trigger rate of scintillator boxes on a time interval less than that of a MACRO run without observing any systematic of the above nature. There were only few (three) cases during which urgent detector maintenance forced us to disconnect a scintillator box while a run was going; all of these were documented in the official MACRO data logbook. However, given the acceptance attained by a single scintillator box ($\sim$1% of full MACRO) and the fraction of the livetime that was lost, we may ignore it safely.

For the purpose of the slow monopole analysis, besides the SMT hardware monitoring, the Waveform Digitizer (WFD) monitoring is of equal importance. We have used muon data in order to monitor the WFD hardware on a run-by-run basis. After fitting the pedestal of the muon waveform, the total integral, maximum pulse height and the pulse width at various discriminator levels was calculated. The averages (performed over the duration of a run) of the pedestal values and the full width at half maximum (FWHM) were used to determine the status of a WFD channel during a given MACRO run. A WFD channel was considered to be "alive" during a run if (a) its average pedestal value was in the interval [1500,2500] and (b) its average FWHM was less than $500ns$. These two quantities (among the several ones we have calculated for every waveform) seemed to have the strongest discriminatory power against WFD channels that experienced hardware problems. Broken WFD channels normally result in completely unphysical baselines and/or step-like pulses that can easily be identified by their systematically large ($> 500ns$) width (see figure 3.8).

The next question we had to address was what should be the minimum run duration in order for the aforementioned SMT and WFD criteria to be imposed. We have chosen to follow the procedure we have just described in order to determine the status of the MACRO detector for runs that lasted *more than three hours.* For those runs that lasted less than three hours, we have used their own data to determine which was the exact *supermodule (SM) configuration* for this run[2] but we relied on the exact scintillator tank and WFD configuration of the latest run that lasted at

[2]Looking at the "Scintillator Pattern Unit" section of the table E.1 at the end of this section, the status of the SMT trigger in individual SMs may be trivially read off.

least three hours and collected data from these SMs. Given that the mean SMT rate for an individual scintillator tank is $\sim 3hr^{-1}$, then the Poisson probability for *not* observing any SMT hit from a scintillator tank within n hours is $P(0) = exp(-3n)$. The minimum run length of three hours yields $P(0) \approx 10^{-4}$ which even if multiplied by the number of checked boxes ($\sim$ 300) and the number of affected runs ($\sim$ 100) results in an insignificant number of possible "misidentified" scintillator boxes.

An isotropic flux of particles was projected onto the MACRO detector with the detector's exact configuration as defined above on a *run-by-run* basis. Particle fluxes corresponding to various β's were also generated in order to obtain the β-dependence of the acceptance. The acceptance obtained in this way for every run is plotted in figure E.1. There were 595 runs during which all three μVax were taking data, 40 runs with two μVax and 45 runs with only one μVax taking data. Although these three groups of runs constitute the main configurations of the MACRO detector throughout the six-month run, changes in the exact tank and WFD channel configurations result in the spread of the calculated acceptance values for individual runs (fig. E.1).

Finally in figure E.2 we plot the typical pathlength distributions within a single detector face and for a pair of faces. As mentioned already, the typical pathlength within a detector face is of the order of $20cm$ (which is the height of the horizontal scintillators and the width of the vertical ones), while for pathlengths between face pairs, $4.5m$ (the vertical separation between the bottom and center scintillator layers) is their typical value.

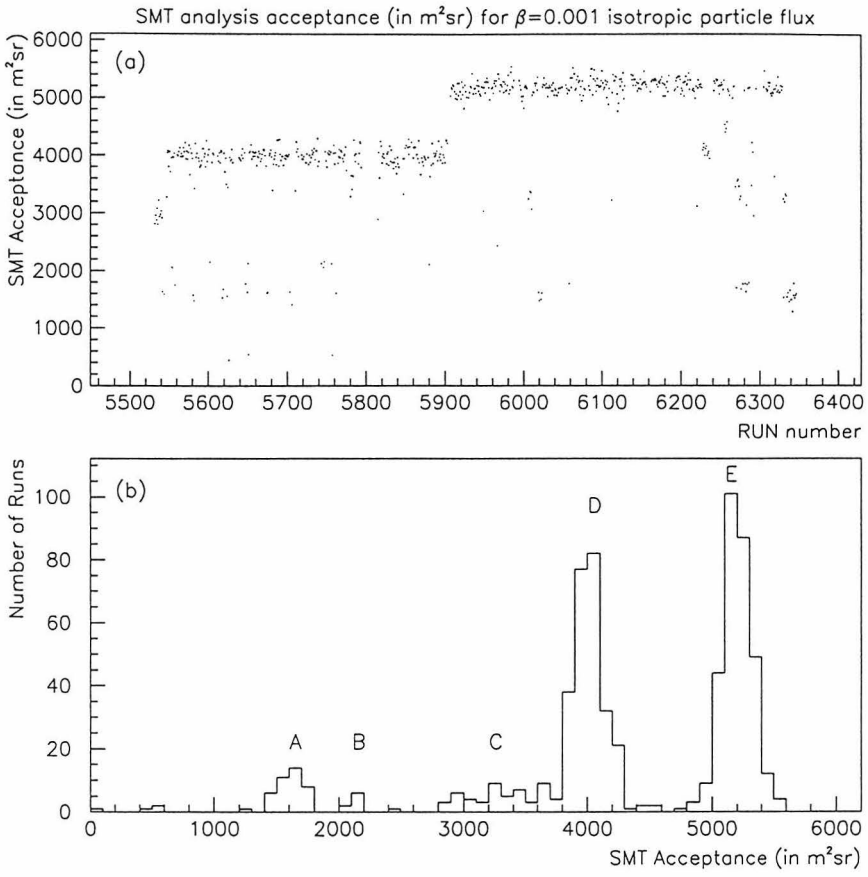

Figure E.1: For an isotropic flux of $\beta = 0.001$ particle we plot in (a) the SMT analysis acceptance versus the run number. The majority of the MACRO runs collected data from the full detector (6SM); the apparent step that appears in MACRO's acceptance around run 5900 is due to the some WFD channels in SM1 which were fixed at that time. The second plot (b) is a projection of (a) onto the acceptance axis. In this plot we may identify five peaks in the acceptance distribution which result from the various detector configurations throughout the six month run. The run-to-run variation in the status of the WFD channels is mainly responsible for the dispersion of the calculated acceptances among identical supermodule (SM) configurations. The observed five main peaks may be identified with the following detector conditions; A: 2SM, B: 4SM with problematic WFD, C: 4SM and some 6SM with problematic WFD, D: 6SM with problematic WFD and some 5SM and finally E: 6SM configurations.

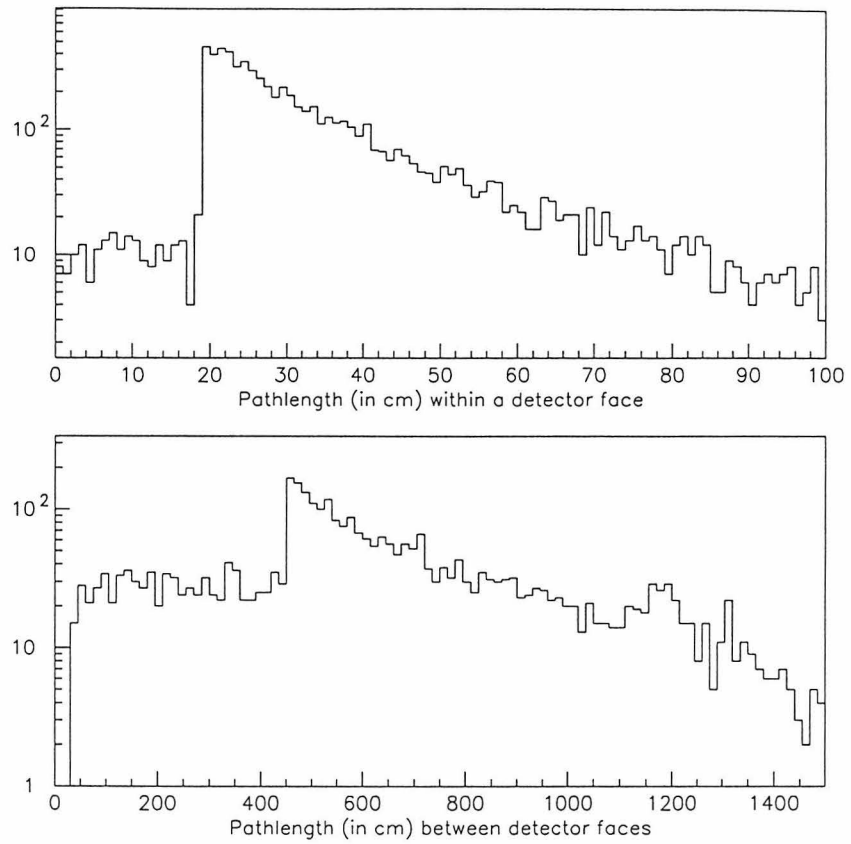

Figure E.2: For an isotropic flux of particles which was projected onto a *fully* functional MACRO detector (no dead tanks, no broken WFD channels) we here plot the distribution of pathlengths within a scintillator *face* (top) and between detector face pairs. The pathlength distribution within a face peaks at $\sim 19.5cm$ which is the nominal height of the (horizontal) scintillators. A similar plot of pathlength distribution within a scintillator *tank* may reveal that there are local maxima of this distribution corresponding to the transverse dimension of the horizontal and vertical scintillator counters ($\sim 74cm$ and $\sim 44cm$ respectively). The two peaks that appear in the pathlength distribution for face pairs correspond to tracks going through two horizontal tanks straight vertically and through two vertical tanks straight horizontally.

Table E.1: Detector Monitoring Output File.

```
**** START OF RUN   6000 STATISTICS ******************************************
This RUN started on : (DD-MM-YY) = 25- 3-1993 at  12.0063887 hours
This RUN ended   on : (DD-MM-YY) = 25- 3-1993 at  16.5552769 hours
This RUN lasted    272.933258 minutes
-- the above RUN length will be used below for calculating RATES --
TRIG # | in uVAX | first/last event | occurred at (VMS TIME)| live time (min)
  2      1 (SM2)      27/  9274      12.0130558/ 16.5247211      270.6998596
  2      2 (SM4)       9/  9285      12.0077782/ 16.5305557      271.3666687
  2      3 (SM6)       3/  9279      12.0063887/ 16.5266666      271.2166443
  2      1 (SM1)      40/  9282      12.0197220/ 16.5288887      270.5500183
  2      2 (SM3)      52/  9283      12.0238886/ 16.5286102      270.2833252
  2      3 (SM5)       9/  9277      12.0077782/ 16.5252781      271.0500488
  5      1 (SM2)     439/  9018      12.2216663/ 16.4005547      250.7333221
  5      2 (SM4)     511/  8926      12.2516670/ 16.3563900      246.2833557
  5      3 (SM6)     545/  8906      12.2638893/ 16.3486118      245.0833588
  5      1 (SM1)     524/  9083      12.2550001/ 16.4305553      250.5333405
  5      2 (SM3)     568/  8950      12.2738886/ 16.3686104      245.6833038
  5      3 (SM5)     471/  8896      12.2352781/ 16.3427792      246.4501190
  7      1            48/  9280      12.0227776/ 16.5272217      270.2666016
  7      2             4/  9283      12.0069447/ 16.5286102      271.2998962
  7      3             9/  9277      12.0077782/ 16.5252781      271.0500488
 12      3          4571/  4571      14.2066669/ 14.2066669        0.0000000
 13      1            27/  9280      12.0130558/ 16.5272217      270.8498840
 13      2             9/  9285      12.0077782/ 16.5305557      271.3666687
 13      3             9/  9285      12.0077782/ 16.5305557      271.3666687

++++ MACRO TRIGGER STATISTICS: ++++++++++++++++++++++++++++++++++++++++++++++++
 Trigger Summary for uVAX 1 (Counts/Rates (per hour))
 2 : ERP_MUON            1748          384.2697754
 4 : BARI_MU             2037          447.8017883
 5 : ERP_GC                38            8.3536901
 7 : CIT_MONO             772          169.7118225
10 : ST_MONOH            1261          277.2106323
13 : SPAM_MU             1466          322.2765808
15 : 1/3_EVNT              18            3.9570112
16 : 1/2_EVNT            1381          303.5906982

Trigger Statistics for the rest of the microvaxes follow ...

++++ SCINTILLATOR PATTERN UNIT STATISTICS: ++++++++++++++++++++++++++++++++++++
 SPU Summary for uVAX 1 (Counts/Rates (per hour))
 3 : TOHM1                380           83.5369034
 4 : TOHM2                403           88.5930862
 5 : CSPAM12              984          216.3166199
 7 : ERP1                 906          199.1695709
 8 : ERP2                 926          203.5662537
 9 : ERPGC1                17            3.7371774
10 : ERPGC2                21            4.6165133
12 : CSPAM23              960          211.0406036
15 : LASER                  1            0.2198340

Scintillator Pattern Unit Statistics for the rest of the microvaxes follow ...

++++ SPAM MUON STATISTICS (Counts/Rates (per hour)) : ++++++++++++++++++++++++
                     H1            H0            L1            L0
```

```
uVAX:1  2B:    247/  54.299   272/  59.795   227/  49.902   239/  52.540
uVAX:1  1B:    232/  51.001   244/  53.639   241/  52.980   241/  52.980
uVAX:1  2C:    270/  59.355   271/  59.575   239/  52.540   276/  60.674
uVAX:1  1C:    240/  52.760   239/  52.540   209/  45.945   222/  48.803
uVAX:1  2W:      0/   0.000     0/   0.000    87/  19.126    88/  19.345
uVAX:1  1W:      0/   0.000     0/   0.000    79/  17.367    81/  17.807
uVAX:1  2E:      0/   0.000     0/   0.000   104/  22.863   102/  22.423
uVAX:1  1E:      0/   0.000     0/   0.000    94/  20.664    92/  20.225
uVAX:1  2B:    248/  54.519   272/  59.795   227/  49.902   238/  52.320

SPAM muon (i.e., CSPAM) statistics for the rest of the microvaxes follow ...

++++ SPAM MONOPOLE STATISTICS (Counts/Rates (per hour)): ++++++++++++++++++++++
                      H1             H0             L1             L0
uVAX:3  4B:      1/   0.220     0/   0.000     0/   0.000     0/   0.000
uVAX:3  6B:      0/   0.000     0/   0.000     1/   0.220     1/   0.220
uVAX:3  6C:      1/   0.220     1/   0.220     0/   0.000     0/   0.000

+++++ SMT (TRIGGERS and ACTIVITIES) STATISTICS(Counts/Rates (per hour)) : +++++
--lines: 1st=TRIGGERS, 2nd=TRIGGER RATES ,3rd=ACTIVITIES, 4th=ACTIVITY RATES--
1B01 1B02 1B03 1B04 1B05 1B06 1B07 1B08 1B09 1B10 1B11 1B12 1B13 1B14 1B15 1B16
   3    3    3    8    7    2    2    7    4    6    6   10   12    2    9    7
 0.7  0.7  0.7  1.8  1.5  0.4  0.4  1.5  0.9  1.3  1.3  2.2  2.6  0.4  2.0  1.5
   3    3    4    8    9    3    3    7    5    6    7   11   12    2    9    7
 0.7  0.7  0.9  1.8  2.0  0.7  0.7  1.5  1.1  1.3  1.5  2.4  2.6  0.4  2.0  1.5
1C01 1C02 1C03 1C04 1C05 1C06 1C07 1C08 1C09 1C10 1C11 1C12 1C13 1C14 1C15 1C16
   1    6    3    3    7    3    8    8    4    0    6    0    4   40    3   11
 0.2  1.3  0.7  0.7  1.5  0.7  1.8  1.8  0.9  0.0  1.3  0.0  0.9  8.8  0.7  2.4
   2    6    4    4    7    3    8    8    4    0    6    0    4   40    5   13
 0.4  1.3  0.9  0.9  1.5  0.7  1.8  1.8  0.9  0.0  1.3  0.0  0.9  8.8  1.1  2.9
1W01 1W02 1W03 1W04 1W05 1W06 1W07 1LED 1E01 1E02 1E03 1E04 1E05 1E06 1E07 1LAS
  17   37    5    7   19    4   12    0   46   17    7   14    0   20    9    0
 3.7  8.1  1.1  1.5  4.2  0.9  2.6  0.0 10.1  3.7  1.5  3.1  0.0  4.4  2.0  0.0
  18   37    5    7   19    4   12    0   47   17    7   13    0   20    9    0
 4.0  8.1  1.1  1.5  4.2  0.9  2.6  0.0 10.3  3.7  1.5  2.9  0.0  4.4  2.0  0.0

SMT statistics for the rest of the Supermodules follow ...

++++ ERP MUON AND GC STATISTICS (Counts/Rates (per hour)) : ++++++++++++++++++++
--lines: 1st=MUON HITS, 2nd=MUON RATES ,3rd=GC HITS, 4th=GC RATES-------------
1B01 1B02 1B03 1B04 1B05 1B06 1B07 1B08 1B09 1B10 1B11 1B12 1B13 1B14 1B15 1B16
  53   40   36   66   48   54   52   48   42   36   45   44   50   50   37   43
11.7  8.8  7.9 14.5 10.6 11.9 11.4 10.6  9.2  7.9  9.9  9.7 11.0 11.0  8.1  9.5
 435  333  310  393  445  389  342  471  380  287  397  425  578  287  389  238
  95   73   68   86   97   85   75  103   83   63   87   93  127   63   85   52
1C01 1C02 1C03 1C04 1C05 1C06 1C07 1C08 1C09 1C10 1C11 1C12 1C13 1C14 1C15 1C16
  39   36   40   51   47   38   37   54   41   40   35    0   51   44   36   48
 8.6  7.9  8.8 11.2 10.3  8.4  8.1 11.9  9.0  8.8  7.7  0.0 11.2  9.7  7.9 10.6
 408  378  340  359  435  378  390  406  365  370  288    0  344  262  391  358
  89   83   74   78   95   83   85   89   80   81   63    0   75   57   85   78
1W01 1W02 1W03 1W04 1W05 1W06 1W07 1LED 1E01 1E02 1E03 1E04 1E05 1E06 1E07 1LAS
  20   15   21   25   20   20   19    0   23   29   20   22    0   23   23    0
 4.4  3.3  4.6  5.5  4.4  4.4  4.2  0.0  5.1  6.4  4.4  4.8  0.0  5.1  5.1  0.0
 114  141  197  106  173  140  284    0  178  143  254  277    0  150  178    0
  25   30   43   23   38   30   62    0   39   31   55   60    0   32   39    0

ERP statistics for the rest of the Supermodules follow ...

**** END OF RUN   6000 STATISTICS ********************************************
```

Bibliography

[1] F. C. Adams et al., *Extension of the Parker Bound on the Flux of Magnetic Monopoles*, Phys. Rev. Lett., 70 (1993) 2511-2514

[2] S. P. Ahlen, *Stopping-power Formula for Magnetic Monopoles*, Phys. Rev., D17 (1978) 229-233

[3] S. P. Ahlen and K. Kinoshita, *Calculation of the Stopping Power of Very-Low-Velocity Magnetic Monopoles*, Phys. Rev., D26 (1982) 2347-2363

[4] S. P. Ahlen, T. M. Liss and G. Tarlé, *Comment on Searches for Slowly Moving Magnetic Monopoles* and Groom et al. *Respond*, Phys. Rev. Lett., 51 (1983) 940-941

[5] S. P. Ahlen and G. Tarlé, *Can Grand Unification Monopoles be Detected with Plastic Scintillators?* Phys. Rev., D27 (1983) 688-691

[6] S. P. Ahlen et al., *Scintillation from Slow Protons*, Phys. Rev. Lett., 55 (1985) 181-184

[7] E. N. Alexeyev et al., *A Search for Superheavy Magnetic Monopole by Baksan Underground Scintillation Telescope*, Abstract, Proceedings of the 21st International Cosmic Ray Conference, Adelaide, 1990

[8] M. Ambrosio et al., *Strip Readout Electronics for the MACRO Detector*, Nucl. Instr. Meth., A301 (1991) 275-278

[9] M. Ambrosio et al., *The QTP System for the MACRO Experiment at Gran Sasso*, Nucl. Instr. Meth., A321 (1992) 609-616

[10] F. Anselmo et al., *The Convergence of the Gauge Couplings at E_{GUT} and Above: Consequences for $\alpha_3(M_Z)$ and SUSY Breaking*, Nuov. Cim., A105 (1992) 1025-1044

[11] G. Auriemma, *The Rock Overburden of the Gran Sasso Laboratory*, MACRO internal note 12/90 (1990) (unpublished)

[12] G. Auriemma et al., *Monopole Trigger for the Streamer Tube System in MACRO*, Nucl. Instr. Meth., A263 (1988) 249-254

[13] E. Barbarito et al., *A Muon Trigger for the MACRO Apparatus*, Nucl. Instr. Meth., A300 (1991) 581-585

[14] B. Barish, G. Liu and C. Lane, *Search for Grand Unification Monopoles and Other Ionizing Heavy Particles Using a Scintillator Detector at the Earth's Surface*, CALT-68-1441 also Phys. Rev., D36 (1987) 2641-2648

[15] B. C. Barish, *Neutrino Physics in MACRO at Gran Sasso*, Nucl. Phys., B (proc. suppl.) 31 (1993) 437-449

[16] G. Battistoni, *Tracking Techniques in Underground Physics*, Nucl. Instr. Meth., A279 (1989) 137-141

[17] G. Battistoni et al., *Electrodeless Plastic Streamer Tubes*, Nucl. Instr. Meth., 217 (1983) 429-431

[18] G. Battistoni et al., *Response of Streamer Tubes to Highly Ionizing Particles*, Nucl. Instr. Meth., A270 (1988) 185-189

[19] R. Becker-Szendy et al. (The IMB Collaboration), *New Magnetic Monopole Flux Limits from the IMB Proton Decay Detector*, Phys. Rev., D49 (1994) 2169-2173

[20] I. B. Berlman, *Handbook of Fluorescence Spectra of Aromatic Molecules*, Academic Press, New York and London, 1971 (p. 170-171, 291-294, 327)

[21] S. Bermon, *Cosmic-Ray Monopole Search at IBM-BNL Using Superconducting Induction Detectors*, IEEE Trans. Magn., 23 (1987) 441-449

[22] S. Bermon et al., *New Limit Set on Cosmic-Ray Monopole Flux by a Large-Area Superconducting Magnetic-Induction Detector*, Phys. Rev. Lett., 64 (1990) 839-842

[23] L. B. Berzukov et al., *Search for Superheavy Magnetic Monopoles in Deep-Underground Experiments at Lake Baikal*, Sov. J. Nucl. Phys., 52 (1990) 54-59

[24] L. Bracci et al., *Formation of Monopole-Proton Bound States in the Hot Universe*, Phys. Lett., B143 (1984) 357-362 and Errata, Phys. Lett., B155 (1985) 468

[25] K. N. Buckland et al., *Results of a Magnetic-Monopole Search Utilizing a Large-area Proportional-tube Array*, Phys. Rev., D41 (1990) 2726-2731

[26] B. Cabrera, *First Results from a Superconductive Detector for Moving Magnetic Monopoles*, Phys. Rev. Lett., 48 (1982) 1378-1381

[27] C. G. Callan Jr., *Dyon-fermion Dynamics*, Phys. Rev., D26 (1982) 2058-2068

[28] S. Cartwright et al., *A Nuclear-Track-Recording Polymer of Unique Sensitivity and Resolution*, Nucl. Instr. Meth., 153 (1978) 457-460

[29] S. Cecchini et al., *Calibration of the Intercast CR39*, Nucl. Tracks Radiat. Meas., 22 (1993) 555-558

[30] M. Chown, *British Physicists Find Magnetic Monopole*, New Scientist, 31 October 1985 p. 11

[31] C. K. Chui, *An Introduction to Wavelets*, Academic Press, 1992

[32] P. D. B. Collins, A. D. Martin and E. J. Squires, *Particle Physics and Cosmology*, John Wiley & Sons, New York, 1989

[33] I. Daubechies, *Ten Lectures on Wavelets*, SIAM, 1992

[34] I. Daubechies, S. Mallat and A. Willsky, *Special issue on wavelet transform and multiresolution signal analysis*, IEEE Trans. Infor. Theo., 32 (1992) 529-930

[35] E. B. Diehl, *Limits on Neutralino Dark Matter by a Search for Upward Muons in the MACRO Detector*, Ph.D. Thesis, University of Michigan (1994)

[36] S. Dimopoulos, J. Preskill and F. Wilczek, *Catalyzed Nucleon Decay in Neutron Stars*, Phys. Lett., B119 (1982) 320-322

[37] S. Dimopoulos et al., *Is There a Local Source of Magnetic Monopoles?* Nature, 298 (1982) 824-825

[38] P. A. M. Dirac, *Quantised Singularities in the Electromagnetic Field*, Proc. Roy. Soc., A133 (1931) 60-72

[39] T. Doke et al., *CR-39 Plastic for Massive Magnetic Monopole Search*, Nucl. Instr. Meth. Phys., B34 (1988) 81-88

[40] S. D. Drell et al., *Energy Loss of Slowly Moving Magnetic Monopoles in Matter*, Phys. Rev. Lett., 50 (1983) 644-648

[41] J. Ellis, S. Kelley and D. V. Nanopoulos, *A Detailed Comparison of LEP Data with the Predictions of the Minimal Supersymmetric SU(5) GUT*, Nucl. Phys., B373 (1992) 55-72

[42] *Expression of Interest for a Long Baseline Neutrino Oscillation Experiment Using a CERN Beam and a large Magnetic Sampling Calorimeter at Gran Sasso*, submitted to the scientific committee of the Laboratori Nazionali del Gran Sasso, May 1994

[43] D. J. Ficenec et al., *Observation of Electronic Excitation by Extremely Slow Protons with Applications to the Detection of Supermassive Charged Particles*, UM-HE-87-0001 January 21, 1987 and Phys. Rev., D36 (1987) 311-314

[44] R. Fleischer, P. B. Price and R. M. Walker, *Nuclear Tracks in Solids*, University of California Press, Los Angeles, 1976

[45] K. Freese and M. S. Turner, *Is the Local Monopole Flux Enhanced?* Phys. Lett., B123 (1983) 293-298

[46] A. Galli, *Are Grand Unified Theories Ruled out by the LEP Data?* Nuov. Cim., A106 (1993) 1309-1320

[47] H. Georgi and S. L. Glashow, *Unity of All Elementary-Particle Forces*, Phys. Rev. Lett., 32 (1974) 438-441

[48] G. Giacomelli, *Magnetic Monopoles*, Riv. Nuov. Cim., 7 (1984) 1-111

[49] D. E. Groom, *In Search of the Supermassive Magnetic Monopole*, Phys. Rep., 140 (1986) 323-373

[50] D. E. Groom, *Is There Any Place Left for a Massive Magnetic Monopole to Hide?* Proceedings of the 3rd Conference on the Interactions Between Particle and Nuclear Physics, Rockport, Maine, May14-19, 1988

[51] A. Grossmann and J. Morlet, *Decomposition of Hardy functions into square integrable wavelets of constant shape*, SIAM J. Math. Anal., 15 (1984) 723-736

[52] A. H. Guth, *Inflationary Universe: A Possible Solution to the Horizon and Flatness Problems*, Phys. Rev., D23 (1981) 347-356

[53] A. Haar, *Zur Theorie der orthogonalen Funktionensysteme*, Math. Ann., 69 (1910) 331-371

[54] J-T. Hong, *Search for GUT Magnetic Monopoles and Other Supermassive Particles with the MACRO Detector*, Ph.D. Thesis, California Institute of Technology (1993)

[55] M. E. Huber et al., *Search for a Flux of Cosmic-Ray Magnetic Monopoles with an Eight-channel Superconducting Detector*, Phys. Rev., D44 (1991) 636-660

[56] E. Iarocci, *Plastic Streamer Tubes and Their Application in High Energy Physics*, Nucl. Instr. Meth., 217 (1983) 30-42

[57] The ICARUS Collaboration, *Argon Purification in the Liquid Phase*, Nucl. Inst. Meth., A333 (1993) 567-570

[58] INFN-Laboratori Nazionali del Gran Sasso, *ANNUAL REPORT 1993*, LNGS - 94/98

[59] J. D. Jackson, *Classical Electrodymanics*, second edition, John Wiley & Sons, Inc., New York, 1974

[60] R. Katz and E. J. Kobetich, *Formation of Etchable Tracks in Dielectrics*, Phys. Rev., 170 (1968) 401-405

[61] T. W. B. Kibble, *Topology of Cosmic Domains and Strings*, J. Phys., A9 (1976) 1387-1398

[62] E. W. Kold and M. S. Turner, *The Early Universe*, Addison-Wesley, 1990

[63] A. K. Komives et al., *A Spectrophotometer for Measuring Long Attenuation Lengths*, Nucl. Inst. Meth., A317 (1992) 170-174

[64] K. Lee and E. J. Weinberg, *Nontopological Magnetic Monopoles and New Magnetically Charged Black Holes*, Phys. Rev. Lett., 73 (1994) 1203-1206

[65] W. R. Leo, *Techniques for Nuclear and Particle Physics Experiments*, Springer-Verlag, Berlin, 1992

[66] J. Lindhard, Mat. Fys. Medd. Dan. Vid. Selsk., 28, No. 8 (1954)

[67] J. Lindhard and M. Scharff, Phys. Rev., 124 (1961) 128

[68] G. Ludlam and C. Okada, *The LED Calibration System: Description and Users Guide*, MACRO internal note 1012/93 (1993) (unpublished)

[69] The MACRO Collaboration, *Arrival Time Distributions of High-Energy Cosmic Ray Muons in MACRO*, Nucl. Phys., B370 (1992) 432-444

[70] The MACRO Collaboration, *First Supermodule of the MACRO detector at Gran Sasso*, Nucl. Instr. Meth. Phys., A324 (1993) 337-362

[71] The MACRO Collaboration, *Improvements in the CR39 Polymer for the MACRO Experiment at the Gran Sasso Laboratory*, Nucl. Tracks Radiat. Meas., 19 (1991) 641-646

[72] The MACRO Collaboration, *Measurement of the Decoherence Function with the MACRO Detector*, Phys. Rev., D46 (1992) 4836-4845

[73] The MACRO Collaboration, *Muon Astronomy with the MACRO Detector*, Astroph. J., 412 (1993) 301-311

[74] The MACRO Collaboration, *Muon Astronomy and Search for Sidereal Anisotropies*, Proceedings of 23rd ICRC, Calgary, Vol. 4 (1993) 450-453

[75] The MACRO Collaboration, *Search for Neutrino Bursts from Collapsing Stars with the MACRO Detector*, Astroparticle Phys., 1 (1992) 11-25

[76] The MACRO Collaboration, *Search for Nuclearites using the MACRO Detector*, Phys. Rev. Lett., 69 (1992) 1860-1863

[77] The MACRO Collaboration, *Search for Slowly Moving Magnetic Monopoles with the MACRO Detector*, Phys. Rev. Let., 72 (1994) 608-612

[78] The MACRO Collaboration, *Study of the Ultrahigh-Energy Primary-Cosmic-Ray Composition with the MACRO Detector*, Phys. Rev., D46 (1992) 895-902

[79] The MACRO Collaboration, *Upward Going Muons in MACRO*, To be published (1995)

[80] S. Mallat, *A theory of multiresolution signal decomposition: the wavelet representation*, IEEE Trans. Patt. Anal. Mach. Intel., 11 (1989) 674-693

[81] S. Mallat and W. L. Hwang, *Singularity Detection and Processing with Wavelets*, IEEE Trans. Inf. Theo., 38 (1992) 617-643

[82] S. Mallat and S. Zhong, *Characterization of Signals from Multiscale Edges*, IEEE Trans. Patt. Anal. Mach. Intel., 14 (1992) 710-732

[83] Y. Meyer and S. Roques, *Progress in Wavelet Analysis and Applications*, Proceedings of the International Conference "Wavelets and Applications," Toulouse, France - June 1992, Editions Frontieres, 1993

[84] S. Nakamura et al., *A New Limit on the Flux of Strange Matter*, Phys. Let., B263 (1991) 529-533

[85] A. Noll et al., *The SIEGEN Automatic Measuring System for Nuclear Track Detectors - New Developments*, Nucl. Tracks Radiat. Meas., 15 (1988) 265-268

[86] S. Orito et al., *Search for Supermassive Relics with a 2000-m^2 Array of Plastic Track Detectors*, Phys. Rev. Let., 66 (1991) 1951-1954

[87] E. N. Parker, *The Origin of Magnetic Fields*, Astrophys. J., 160 (1970) 383-404

[88] E. N. Parker, *The Generation of Magnetic Fields in Astrophysical Bodies. II. The Galactic Field*, Astrophys. J., 163 (1971) 255-278

[89] E. N. Parker, *The Generation of Magnetic Fields in Astrophysical Bodies. VI. Periodic Modes of the Galactic Field*, Astrophys. J., 166 (1971) 295-300

[90] V. Patera, *Excitation and Ionization in Low-Z Atoms by Slow Magnetic Monopoles*, Phys. Lett., A137 (1989) 259-266

[91] J. P. Petrakis et al., *A Spectrophotometer for Measuring Liquid Attenuation Lengths at Wavelengths between 400nm and 600nm*, Nucl. Inst. Meth., A268 (1988) 256-261

[92] A. Polyakov, *Particle Spectrum in Quantum Field Theory*, JETP Lett., 20 (1974) 194-195 [Pis'ma Zh. Eksp. Teor. Fiz. Pis. Red. 20 (1974) 430-433]

[93] J. P. Preskill, *Cosmological Production of Superheavy Magnetic Monopoles*, Phys. Rev. Lett., 43 (1979) 1365-1368

[94] J. Preskill, *Magnetic Monopoles*, Ann. Rev. Nucl. Part. Sci., 34 (1984) 461-530

[95] P. B. Price, *Limits on Flux of Supermassive Monopoles and Charged Relic Particles Using Plastic Track Detectors*, Phys. Lett., B140 (1984) 112-115

[96] P. B. Price and M. H. Salamon, *Search for Supermassive Magnetic Monopoles Using Mica Crystals*, Phys. Rev. Lett., 56 (1986) 1226-1229

[97] Y. Rephaeli and M. S. Turner, *The Magnetic Monopole Flux and the Survival of Intracluster Magnetic Fields*, Phys. Lett., B121 (1983) 115-118

[98] V. A. Rubakov, *Adler-Bell-Jackiw Anomaly and Fermion-Number Breaking in the Presence of a Magnetic Monopole*, Nucl. Phys., B203 (1982) 311-348

[99] L. H. Ryder, *Quantum Field Theory*, Cambridge University Press, Cambridge, 1985

[100] P. G. H. Sandars, *Magnetic Charge*, Contemp. Phys., 7 (1966) 419-429

[101] K. Scholberg, *Setting Photomultiplier Tube Gains*, MACRO internal note 1019/93 (1993) (unpublished)

[102] K Scholberg, Caltech; private communication (1994)

[103] R. Singer and D. Trautmann, *Excitation of Atoms by Slow Magnetic Monopoles: A Fully Numerical Hartree-Fock Approach*, Nucl. Phys., A554 (1993) 421-438

[104] D. P. Snowden-Ifft and P.B. Price, *The Low Velocity Response of the Solid State Nuclear Track Detector CR39*, Phys. Lett., B288 (1992) 250-253

[105] G. 't Hooft, *Magnetic Monopoles in Unified Gauge Theories*, Nucl. Phys., B79 (1974) 276-284

[106] J. L. Thron et al. (The SOUDAN 2 Collaboration), *Search for Magnetic Monopoles with the SOUDAN 2 Detector*, Phys. Rev., D46 (1992) 4846-4851

[107] M. S. Turner, E. N. Parker and T. J. Bogdan, *Magnetic Monopoles and the Survival of Galactic Magnetic Fields*, Phys. Rev., D26 (1982) 1296-1305

[108] R. Wald, *General Relativity*, University of Chicago Press, Chicago, 1984

[109] J.F. Ziegler, J. P. Biersack and U. Littmark, *The Stopping and Range of Ions in Solids* Pergamon Press, New York, 1985